

國立臺灣大學工學院土木工程學系



碩士論文

Department of Civil Engineering

College of Engineering

National Taiwan University

Master Thesis

深度神經網路應用於短纖維複合材及仿生階層複合結構的

應力應變曲線預測

Stress-strain curve prediction of short fiber-reinforced composites  
and bio-inspired layered structural composites using deep neural  
networks

蔡孟霖

Meng-Lin Tsai

指導教授：張書瑋 博士

Advisor: Shu-Wei Chang, Ph.D.

中華民國 111 年 7 月

July, 2022

國立臺灣大學碩士學位論文  
口試委員會審定書

**National Taiwan University Master Thesis  
Oral Examination Committee Approval**

深度神經網路應用於短纖維複合材及仿生階層複合結構的應力應變曲線  
預測

Stress-strain curve prediction of short fiber-reinforced composites and bio-  
inspired layered structural composites using deep neural networks

本論文係蔡孟霖(R09521221)在國立臺灣大學土木工程學系結構工程組  
完成之碩士學位論文，於民國 111 年 7 月 25 日承下列考試委員審查通  
過及口試及格，特此證明。

Tsai, Meng-Lin (R09521221) completed this master thesis at the Department  
of Civil Engineering Structural Engineering on July 25, 2022 and passed the  
oral examination reviewed by the following examination committee  
members.

口試委員 Oral examination committee members：

張書瑋

(指導教授 Advisor)

張書瑋

陳俊杉

陳俊杉

黃仲偉

黃仲偉

陳柏宇

陳 柏 宇

周佳靚

周佳靚

系主任

謝尚賢

謝尚賢



## 誌謝



研究所短短的兩年轉眼間就過去了，尤其是因為疫情而改成線上授課，幾乎有一半的時間都在家裡上課。儘管如此，還是覺得這段日子是個獨特的歷程，是個不斷學習、不斷認識自我的過程。

首先，要感謝我的指導教授張書瑋老師，在這段日子裡引導我學習，讓我不會迷失方向並指引我向對的方向前進。除了學術上的知識及待人處事上，從老師身上學到更多的是如何去思考、分析問題，進而精準的解決問題。也謝謝老師總是很有耐心地跟我討論，不厭其煩地提點我、幫助我收斂所有發散的想法。也給予我很多機會在各樣的場合學習、報告，讓我對於表達自己的想法也有很大的進步。另外，也要謝謝陳俊杉老師、黃仲偉老師、陳柏宇老師與周佳靚老師作為我的口試委員提供很多寶貴的建議及後續可能思考的方向，讓我能夠將論文更加完善。謝謝仲偉老師在建模跟跑模擬方面提供很多指導與協助。而在參與 BioMGI 計畫的這兩年，俊杉老師、柏宇老師跟佳靚老師的團隊總是呈現豐富又厲害的研究，讓我認識到各種仿生相關的材料及研究方法。

謝謝 813 的大家，雖然我不是很常會去研究室，但待在那裡的時間都是很快樂的。謝謝亞芸跟憲君，不論是在修課或研究上都給我很多幫助，是我一起上課、討論研究、或在上課時間討論研究的好夥伴。謝謝諺霖常常跟我一起聊對各種事情的看法，也謝謝維翰學長、羽白學長、江元學長在研究上常常提供我很多想法。也謝謝其他 M5 lab 的大家，能夠待在這樣氣氛很好的 group 真的是我很大的榮幸。

最後，最謝謝我的父母給予我無限的關愛與照顧，讓我能夠無憂無慮的長大，提供我最好的學習資源與生活環境，同時也都很支持我的所有決定，讓我走想走的



路，做我最堅實的後盾。謝謝哥哥作為一個好榜樣讓我來學習，常常跟我分享一些過來人的經驗，也一直作為我最好的朋友。謝謝心渝人在國外也一直都很關心我、支持我，也給了我很多的鼓勵。感謝上帝保守看顧。謹以本論文獻給在研究所這兩年相遇或曾幫助過我的人們來表達我最真摯的感謝。

## 中文摘要



本研究針對短纖維複合材及仿生階層複合結構建立了一套以深度神經網絡預測應力應變曲線的流程。從古至今，材料的發展一直都在帶領著人類生活不斷地進步。近年來，因為電腦計算模擬技術、3D 列印及機器學習等先進技術的蓬勃發展，材料的設計得以更加深入地探討，能拓展的層面也越來越廣。因此，透過機器學習輔助，在廣大的設計空間中藉由預測應力應變曲線來更加了解材料性質，找尋符合需求的材料，是本研究主要的宗旨。

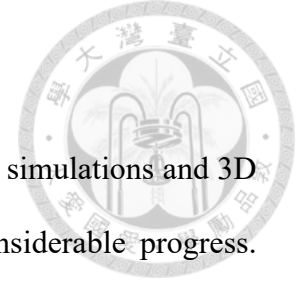
短纖維複合材料的材料性質受許多因素影響，如纖維形狀、纖維含量、纖維的方向性及基體材料與纖維之間的介面的品質等。三維的有限元素分析能精準的預測短纖維複合材料的材料性質；然而，計算需耗費相當大的計算資源及成本。因此，本研究利用主成分分析 (PCA) 降維後訓練了深度神經網絡 (DNN) 預測模型，建立材料組成物的性質以及由有限元素分析 (FEA) 得來的應力應變曲線的關係，以預測短纖維複合材料的應力應變曲線，再由應力應變曲線求得其各應變下的應力與勁度。此預測模型材料性質的決定係數 ( $R^2$ ) 皆高達 0.9 以上，而預測之應力應變曲線與真實值之應力應變曲線比較下的相對最大誤差大部分都小於 10%。此外，本研究亦提出應用理論引導之機器學習 (TGML) 以及兩階段機器學習 (two-phase learning) 之方法來提升預測模型之準確度。而上述方法可延伸應用於其他具非線性材料性質之複合材料分析。

另外，自然環境中生物材料具有相當好的機械性質與多功能性，因此值得我們作為設計材料時的參考。本研究的仿生階層複合結構是啟發自骨頭的拓撲與竹子的階層密度分佈。本研究運用主成分分析降維後訓練了另一個深度神經網絡預測模型，建立複合材各階層之體積分率與來自二維三角晶格彈簧模型 (LSM) 模擬得到的應力應變曲線的關係，以預測具破壞行為之仿生階層複合結構的應力應變曲線，再由其應力應變曲線求得最大強度及韌性。此部分預測模型韌性的決定係數高達 0.85，而強度的決定係數亦達 0.8。因此可驗證此預測模型可以準確且有效地預測材料的應力應變曲線，在廣大的設計空間中能夠更快速地了解材料性質，更進一步去促進材料設計的發展與最佳化。

關鍵字：機器學習、深度神經網絡、短纖維複合材料、理論引導之機器學習、兩階段機器學習、仿生階層複合結構



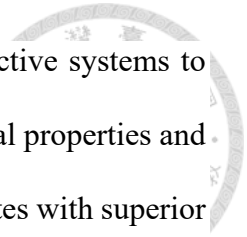
# Abstract



In recent years, attributed to the advancement in computational simulations and 3D printing experiments, the development of materials has made considerable progress. Despite these material analysis methods providing highly accurate predictions of material properties, they are not feasible to explore the colossal design space of structural materials due to the high cost and time consumption. Therefore, in this research, machine learning techniques are utilized to predict stress-strain curves of different composite materials and further understand the mechanical behaviors of composites.

Firstly, this study predicts the mechanical response of short fiber-reinforced composites (SFRCs). The properties of SFRCs greatly depend on several factors, such as fiber shape, fiber content, fiber orientation, and the interphase quality between fiber and matrix materials. Three-dimensional finite element analyses (FEA) for the SFRCs predict composite properties accurately; however, the tremendous consumption of computational cost and time is a critical disadvantage. With the aid of machine learning techniques, the predictions of the composite properties can be produced effectively and accurately at the same time when having a sufficient amount of data. In this research, we propose a machine learning approach via training a deep learning network with the FEA dataset to predict the nonlinear mechanical response of short fiber-reinforced composites. Moreover, theory-guided machine learning (TGML) and two-phase learning approaches are adopted to enhance predictive performances. Our results show that TGML and two-phase learning methods can capture more information on the data and thus improve predictive performances. The proposed method can be extended to other composite analyses with nonlinear mechanical behavior.

Secondly, the mechanical responses of bio-inspired layered structural composites are



predicted in this work. Biological materials evolve extraordinary protective systems to survive the competitive environment, thus having outstanding mechanical properties and multifunctionality. For instance, bone and bamboo are both bio-composites with superior mechanical properties. In this research, the composite structures are inspired by the topology of bone and the density distribution of bamboo. To explore the vast design space of structural materials, we developed a machine learning-based surrogate model using a combination of principal component analysis (PCA) and deep neural networks (DNN) and predicted the entire stress-strain behavior of the bio-inspired layered composite structures. The results show that the surrogate model is accurate and efficient for investigating the design space. The proposed approach in this work can be extended to other composite structures to accelerate material design and optimization.

**Keywords:** Machine Learning, Deep Neural Network, Short Fiber-reinforced Composite, Theory-guided Machine Learning, Two-phase Learning, Bio-inspired Layered Structural Composite

# List of Contents



誌謝 .....	i
中文摘要 .....	iii
Abstract.....	v
List of Contents .....	vii
List of Figures.....	ix
List of Tables .....	xv
<b>Chapter 1 Introduction .....</b>	<b>1</b>
1.1 Background and Motivation .....	1
1.2 Literature Review .....	4
1.3 Objectives of the Thesis.....	12
1.4 Organization of the Thesis .....	13
<b>Chapter 2 Materials and Methods.....</b>	<b>15</b>
2.1 Data Generation .....	15
2.1.1 FCC-Structured RVE SFRC Dataset.....	15
2.1.2 Bio-Inspired Layered Structural Composite Dataset .....	18
2.2 Principal Component Analysis .....	21
2.3 Machine Learning Approaches .....	22
2.3.1 Fundamental Concepts of Machine Learning .....	22
2.3.2 Deep Learning .....	23
<b>Chapter 3 Stress-strain Curve Predictions of SFRCs.....</b>	<b>29</b>
3.1 Dataset Preparation.....	29
3.2 DNN Model Setup .....	32

3.3	Results and Discussion .....	36
3.4	Summary.....	42
<b>Chapter 4</b>	<b>TGML and Two-phase Learning for Enhancing Stress-strain Curve</b>	
	<b>Predictions of SFRCs .....</b>	<b>43</b>
4.1	Dataset Preparation.....	44
4.1.1	Dataset for Each Task.....	44
4.1.2	Data Preparation for Model X.....	45
4.1.3	Data Preparation for Model Y .....	46
4.1.4	Data Preparation for Model Z .....	47
4.2	DNN Model Setup .....	49
4.3	Results and Discussion .....	49
4.4	Summary.....	79
<b>Chapter 5</b>	<b>Stress-strain Curve Predictions of Bio-inspired Layered Structural</b>	
	<b>Composites.....</b>	<b>81</b>
5.1	Dataset Preparation.....	82
5.2	DNN Model Setup .....	84
5.3	Results and Discussion .....	87
5.4	Properties Prediction of Whole Design Space.....	90
5.5	Summary.....	91
<b>Chapter 6</b>	<b>Conclusions and Future Work.....</b>	<b>93</b>
6.1	Conclusions.....	93
6.2	Future Work .....	94
References	.....	95

# List of Figures



Fig 1.1: Toughness and stiffness for different materials [1].	1
Fig 1.2: Projections for natural and synthetic materials [2].	2
Fig 1.3: Multiscale simulation strategy for virtual testing of SFRCs [33].	5
Fig 1.4: The eight most common biological structural design elements [57].	7
Fig 1.5: Bone-inspired composite. (a) Biomimetic approach. (b) Schematic of the sample geometry, applied loading condition, and corresponding stress-strain curve for the base materials. (c) Types of composites [62].	8
Fig 1.6: Natural bamboo with both gradient and cellular structures. (a) Cross-section of natural bamboo. (b) The volume fraction of each layer [64].	8
Fig 1.7: The flow chart of the ML approach using the linear model for an eight-by-eight system [66].	10
Fig 1.8: Workflow of the modeling process to predict stress-strain curve by CNN model [67].	11
Fig 1.9: The overall workflow for applying transfer learning to predict stress-strain curves of fiber composites [71].	11
Fig 2.1: FCC-structured RVE SFRCs for FEM. (a) Aspect ratio = 1. (b) Aspect ratio = 4. (c) Aspect ratio = 7. (d) Aspect ratio = 10.	16
Fig 2.2: Illustration of the effect of interphase properties $K$ and $t_{\max}$ .	17
Fig 2.3: Illustration of the bio-inspired layered structural composite.	18
Fig 2.4: (a) Illustration of the composition of the composite. (b) Illustration of uniaxial tensile test simulation and LSM model.	19
Fig 2.5: Comparison between traditional programming and machine learning.	22



Fig 2.6: Illustration of a DNN model. ....	25
Fig 2.7: Illustration of the training loop. [80].....	25
Fig 3.1: Illustration of the workflow to predict stress-strain curves of SFRCs. ....	29
Fig 3.2: Input (material properties) and output (stress-strain curve data transformed to 5- dimension data via PCA) formats. ....	30
Fig 3.3: Distribution of each composite composition. (a) $\sigma_y/E_0$ (b) $k/E_0$ (c) $E_1/E_0$ (d) AR (e) K (f) $t_{max}$ . ....	31
Fig 3.4: Cumulative explained variance ratio with respect to the number of dimensions. .....	31
Fig 3.5: DNN architecture. ....	32
Fig 3.6: 8 comparisons between the predicted stress-strain curve and the actual stress- strain curve (FEM). ....	37
Fig 3.7: Loss history of the predictive model. ....	38
Fig 3.8: $R^2$ visualization plot of stiffness. ....	38
Fig 3.9: $R^2$ visualization plot of stress when strain = 0.01. ....	39
Fig 3.10: $R^2$ visualization plot of stress when strain = 0.02. ....	39
Fig 3.11: $R^2$ visualization plot of stress when strain = 0.03. ....	40
Fig 3.12: $R^2$ visualization plot of stress when strain = 0.04. ....	40
Fig 3.13: $R^2$ visualization plot of stress when strain = 0.05. ....	41
Fig 3.14: Comparison between predictive performances of ML with FEM for SFRCs. 82 testing data were used for comparison. ....	41
Fig 4.1: The overall workflow for predicting stress-strain curves of SFRCs. ....	43
Fig 4.2: Illustration of the dataset of each model. ....	45
Fig 4.3: Comparison between Halpin-Tsai Derived $E_c/E_0$ and actual values from FEM. .....	47

Fig 4.4: Illustration of two-phase learning. ....	48
Fig 4.5: $R^2$ visualization of the 5th-degree polynomial model. ....	48
Fig 4.6: Loss history of task A. (a) Model X1. (b) Model Y1. (c) Model Z1. ....	52
Fig 4.7: 8 comparisons between predicted stress-strain curves by model X1, Y1, and Z1 and the actual stress-strain curve (FEM). ....	53
Fig 4.8: $R^2$ visualization plot of model X1. (a) Stiffness. (b) Stress when strain = 0.01. (c) Stress when strain = 0.03. (d) Stress when strain = 0.05. ....	54
Fig 4.9: $R^2$ visualization plot of model Y1. (a) Stiffness. (b) Stress when strain = 0.01. (c) Stress when strain = 0.03. (d) Stress when strain = 0.05. ....	55
Fig 4.10: $R^2$ visualization plot of model Z1. (a) Stiffness. (b) Stress when strain = 0.01. (c) Stress when strain = 0.03. (d) Stress when strain = 0.05. ....	56
Fig 4.11: Comparison between performances of model X1, Y1, and Z1 in task A. ....	57
Fig 4.12: Boxplot of maximum error of model X1, Y1, and Z1 in task A. ....	57
Fig 4.13: Loss history of task B. (a) Model X2. (b) Model Y2. (c) Model Z2. ....	59
Fig 4.14: 8 comparisons between predicted stress-strain curves by model X2, Y2, and Z2 and the actual stress-strain curve (FEM). ....	60
Fig 4.15: $R^2$ visualization plot of model X2. (a) Stiffness. (b) Stress when strain = 0.01. (c) Stress when strain = 0.03. (d) Stress when strain = 0.05. ....	61
Fig 4.16: $R^2$ visualization plot of model Y2. (a) Stiffness. (b) Stress when strain = 0.01. (c) Stress when strain = 0.03. (d) Stress when strain = 0.05. ....	62
Fig 4.17: $R^2$ visualization plot of model Z2. (a) Stiffness. (b) Stress when strain = 0.01. (c) Stress when strain = 0.03. (d) Stress when strain = 0.05. ....	63
Fig 4.18: Comparison between performances of model X2, Y2, and Z2 in task B. ....	64
Fig 4.19: Boxplot of maximum error of model X2, Y2, and Z2 in task B. ....	64
Fig 4.20: Loss history of task C. (a) Model X3. (b) Model Y3. (c) Model Z3. ....	66

Fig 4.21: 8 comparisons between predicted stress-strain curves by model X3, Y3, and Z3 and the actual stress-strain curve (FEM). .....	67
Fig 4.22: $R^2$ visualization plot of model X3. (a) Stiffness. (b) Stress when strain = 0.01. (c) Stress when strain = 0.03. (d) Stress when strain = 0.05. ....	68
Fig 4.23: $R^2$ visualization plot of model Y3. (a) Stiffness. (b) Stress when strain = 0.01. (c) Stress when strain = 0.03. (d) Stress when strain = 0.05. ....	69
Fig 4.24: $R^2$ visualization plot of model Z3. (a) Stiffness. (b) Stress when strain = 0.01. (c) Stress when strain = 0.03. (d) Stress when strain = 0.05. ....	70
Fig 4.25: Comparison between performances of model X3, Y3, and Z3 in task C.....	71
Fig 4.26: Boxplot of maximum error of model X3, Y3, and Z3 in task C. ....	71
Fig 4.27: Loss history of task D. (a) Model X4. (b) Model Y4. (c) Model Z4. ....	73
Fig 4.28: 8 comparisons between predicted stress-strain curves by model X4, Y4, and Z4 and the actual stress-strain curve (FEM). ....	74
Fig 4.29: $R^2$ visualization plot of model X4. (a) Stiffness. (b) Stress when strain = 0.01. (c) Stress when strain = 0.03. (d) Stress when strain = 0.05. ....	75
Fig 4.30: $R^2$ visualization plot of model Y4. (a) Stiffness. (b) Stress when strain = 0.01. (c) Stress when strain = 0.03. (d) Stress when strain = 0.05. ....	76
Fig 4.31: $R^2$ visualization plot of model Z4. (a) Stiffness. (b) Stress when strain = 0.01. (c) Stress when strain = 0.03. (d) Stress when strain = 0.05. ....	77
Fig 4.32: Comparison between performances of model X4, Y4, and Z4 in task D.....	78
Fig 4.33: Boxplot of maximum error of model X4, Y4, and Z4 in task D. ....	78
Fig 5.1: Workflow of the modeling process. ....	81
Fig 5.2: Distribution of strength and toughness of the bio-inspired structures dataset. ..	83
Fig 5.3: Cumulative explained variance ratio with respect to the number of dimensions. ....	83

Fig 5.4: Loss history of the predictive model. ....	87
Fig 5.5: 8 comparisons between the predicted stress-strain curve and the actual stress- strain curve (LAMMPS simulation). ....	88
Fig 5.6: $R^2$ visualization plot of strength. ....	89
Fig 5.7: $R^2$ visualization plot of toughness. ....	89
Fig 5.8: Predicted material properties distribution of the whole design space. ....	90



# List of Tables



Table 2.1: Input parameters with given ranges for elasto-plastic composite.....	17
Table 2.2: Parameters of the Harmonic Springs for Different Phases. ....	20
Table 3.1: Average WMSE results with ReLU activation function. The minimum value is highlighted in red. ....	33
Table 3.2: Average WMSE results with LeakyReLU activation function. The minimum value is highlighted in red. ....	34
Table 3.3: Average WMSE results with GeLU activation function. The minimum value is highlighted in red. ....	34
Table 3.4: Average WMSE results with ELU activation function. The minimum value is highlighted in red. ....	35
Table 3.5: Evaluation metrics of predictive models. ....	36
Table 4.1: Evaluation metrics of model X1. ....	50
Table 4.2: Evaluation metrics of model Y1. ....	50
Table 4.3: Evaluation metrics of model Z1. ....	51
Table 4.4: Evaluation metrics of model X2. ....	58
Table 4.5: Evaluation metrics of model Y2. ....	58
Table 4.6: Evaluation metrics of model Z2. ....	58
Table 4.7: Evaluation metrics of model X3. ....	65
Table 4.8: Evaluation metrics of model Y3. ....	65
Table 4.9: Evaluation metrics of model Z3. ....	65
Table 4.10: Evaluation metrics of model X4. ....	72
Table 4.11: Evaluation metrics of model Y4. ....	72

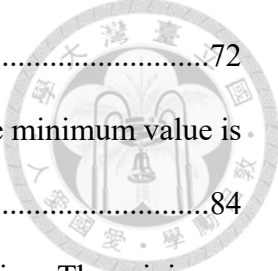


Table 4.12: Evaluation metrics of model Z4. ....	72
Table 5.1: Average WMSE results with ReLU activation function. The minimum value is highlighted in red. ....	84
Table 5.2: Average WMSE results with LeakyReLU activation function. The minimum value is highlighted in red. ....	85
Table 5.3: Average WMSE results with GeLU activation function. The minimum value is highlighted in red. ....	85
Table 5.4: Average WMSE results with ELU activation function. The minimum value is highlighted in red. ....	86
Table 5.5: Evaluation metrics of the predictive model. ....	87

# Chapter 1 Introduction



## 1.1 Background and Motivation

Composites have permeated our daily lives and have played an important role in the evolution of human civilization. Humans have been using composite materials for thousands of years in different ways and in various applications. Date back to 1500 B.C., Egyptians and Mesopotamian builders and artisans used straws to reinforce mud bricks, pottery, and boats. In about 1200 A.D., composite bows were invented by Mongols with a combination of bones, horns, bamboo, and wood bonded with natural pine resin. The powerful and accurate composite bows led Genghis Khan to dominate almost half of the world. During World War II, many composite materials were developed and moved from research to actual production with the advantages of being light-weighted and strong. Since then, the usage of composite materials has begun to expand rapidly.

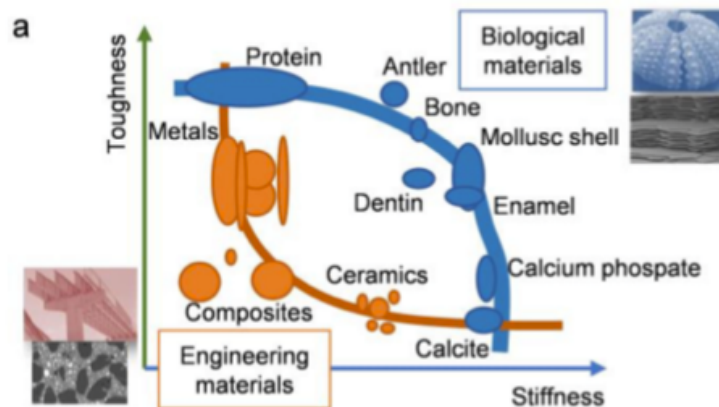


Fig 1.1: Toughness and stiffness for different materials [1].

Most engineering structural materials require stiffness and toughness; however, as shown in Fig 1.1, the properties of stiffness and toughness are mutually exclusive. By contrast, composite materials, which are made of two or more distinct materials with



diverse mechanical, physical, and chemical properties, have different performance characteristics. Due to the combination of typically soft and stiff materials, the stiff-soft mechanism, hierarchical geometry, and multiscale hybrids give the composite better mechanical properties. Besides synthetic composites, composites also exist in nature. For instance, bone, composed of collagen and hydroxyapatite in a hierarchical geometry, has not only outstanding strength-to-weight and stiffness-to-weight ratio but also a remarkable fracture toughness. As shown in Fig 1.2, synthetic and natural composite materials have toughness values far exceeding their basic building blocks. With such significant mechanical behaviors, composite materials have drawn more and more attention from researchers.

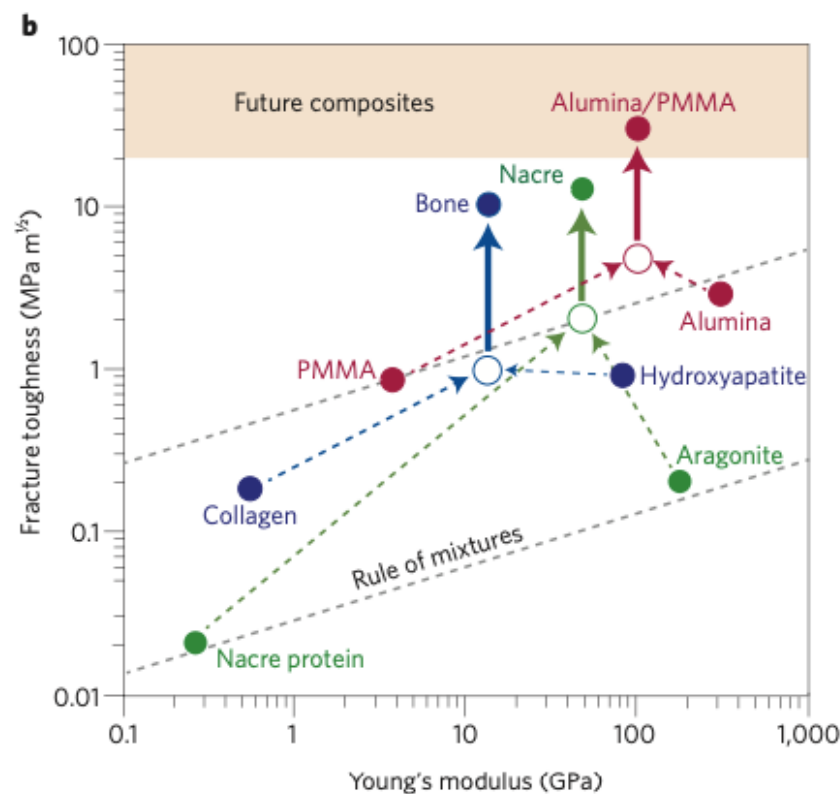
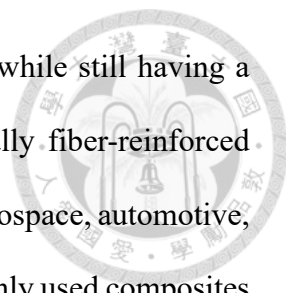


Fig 1.2: Projections for natural and synthetic materials [2].



To meet the need for higher and higher strength and stiffness while still having a light weight simultaneously, applying composite materials, especially fiber-reinforced composites, is a good solution in a wide range of industries such as aerospace, automotive, and construction. Fiber-reinforced polymer is one of the most commonly used composites since it can offer many benefits, including lightweight, lower material costs, corrosion resistance, durability, and design flexibility. Fiber-reinforced polymers have different properties and applications depending on the matrixes and reinforcements, their ratio of the two materials, the bonding between fiber and polymer matrix, etc. Thus, various methods were proposed to analyze the properties of fiber-reinforced polymer composite.

Knowing the effective responses of fiber-reinforced composites is the key to optimizing materials to satisfy the demand of various industries. Hence, many methods are proposed to understand more about the mechanical behaviors of materials. Many researchers have investigated several homogenization methods based on analytical formulations. However, even though homogenization methods can predict material properties faster than experiments, these methods have restrictions because of mathematical assumptions. Because of the improvement of computational capability, the finite element method (FEM) has been widely applied to analyze composite material properties [3]. Numerical modeling can predict entire stress-strain curves so we can get inelastic properties such as strength and toughness. Nevertheless, the nonlinear behavior of materials, consideration of the cohesive interphase, and complexity of structures result in a significant increase in the computational costs of FEM, which limits its applicability. Recently, machine learning techniques have been applied to composite analysis based on data generated from either homogenization or finite element methods. Predictions of the outputs can be immediately produced after we feed inputs into a trained machine learning model. However, a sufficient amount of data is required to ensure that the prediction is

reliable.

It is widely accepted that the performance of a deep neural network (DNN) model can be enhanced by getting a larger dataset. Nonetheless, obtaining a large dataset is often arduous because of high time and cost consumption. Therefore, there is a need to apply techniques such as theory-guided machine learning (TGML) or two-phase learning to create high-performance learners trained with limited data.

## 1.2 Literature Review

With notable advantages like high toughness, high strength, light weight, and ease of fabrication, composite materials offer a possible solution for various usages. Composites play an essential role in civil engineering [4], automotive fabrication [5], aerospace industry [6], and also military technology [7]. To fulfill the need for a wide range of applications, researchers regard understanding the mechanical properties of composite materials as a crucial key.

Defined as materials made by mixing two or more chemically and physically distinct components, composites are divided into three types based on the material of the matrix phase. These include: metal matrix composites (MMCs) [8, 9], ceramic matrix composites (CMCs) [10-12], and polymer matrix composites (PMCs) [13, 14]. These matrixes bind the fibers together while the fibers are the load-bearing component of the composites. Hence, the materials of fibers are also important for the composites, which attracted researchers to investigate composites composed of different types of fibers. In particular, carbon fibers and glass fibers are the most commonly used in composites [15]. Besides, with the increasing environmental awareness, the high cost of carbon fibers, and the threat of a shortage of raw materials, the demand for natural fibers [16, 17] and

recycled fibers [18-20] is rising.

For short fiber-reinforced composites (SFRCs), the external loads are not directly applied to fibers. The load is applied to matrix materials and then transferred to the fibers by fiber ends and the surfaces of fibers. Consequently, the fiber aspect ratio greatly influences the properties of SFRCs [21, 22]. Moreover, the properties of short fiber-reinforced composites also significantly depend on several factors such as fiber shape [23], fiber content [24, 25], fiber coating [26, 27], fiber arrangement [28], and fiber orientation [29]. In addition, the effect of the interphase between fibers and matrix should also be taken into account since it affects the load transferring to fibers and thus has a large impact on the material properties [30-32].

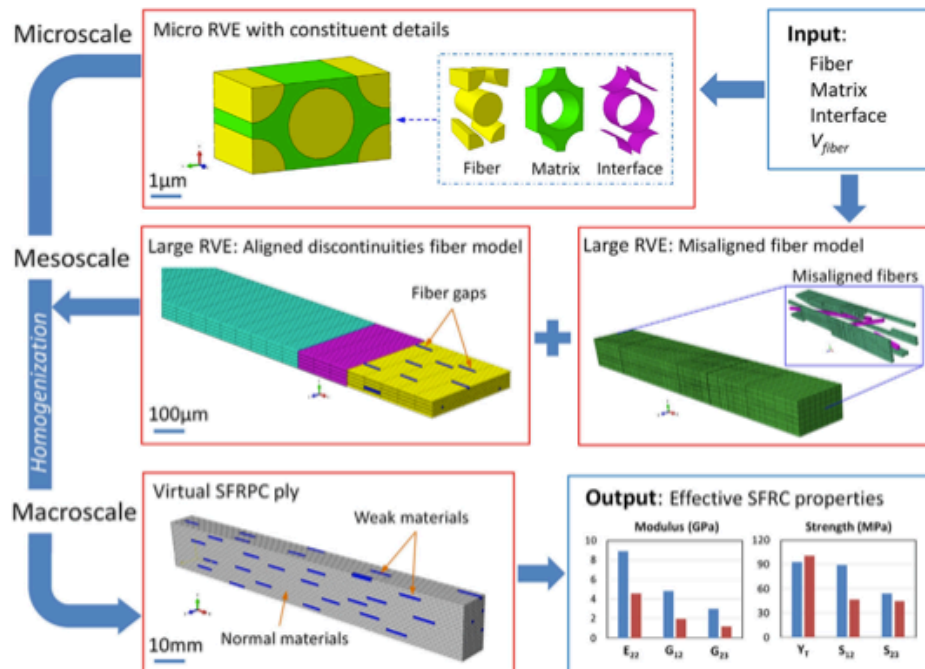
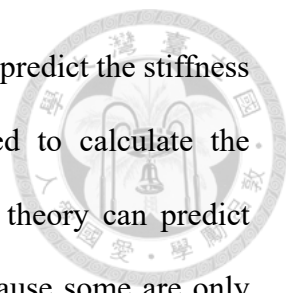


Fig 1.3: Multiscale simulation strategy for virtual testing of SFRCs [33].

Since so many factors affect the mechanical behavior of SFRCs, researchers have made an effort to analyze the properties of SFRCs. Takayanagi et al. [34, 35], Halpin [36-



38], Christensen [39], and Epaarachichi et al. [40] derived models to predict the stiffness of SFRCs. Several homogenization methods have been suggested to calculate the effective material behavior [41-44]. Although the homogenization theory can predict composite properties fast, homogenization methods are limited because some are only valid when the fiber volume fraction is low [45-47] or the fibers are in particular shapes [48]. Therefore, researchers carried out experiments [49-51] and numerical simulations such as FEM [3, 33, 52-56] that offer highly accurate predictions of composite properties. For instance, as shown in Fig 1.3, Wang et al. [33] presented a multiscale approach to generate a microscale representative numerical model of aligned fiber composites, investigate the mesoscale mechanical performance of possible material defects, and predict macroscale effective properties and failure behaviors of SFRCs.

In recent decades, understanding the properties of bio-inspired composites has been a popular subdiscipline of material science. After millions of years of evolution, natural materials are equipped with unique protective systems to survive the competitive environment, which leads to the outstanding mechanical properties and multifunctionality of natural materials. Naleway et al. [57] proposed the eight most common structural design elements in biological materials, including fibrous, helical, gradient, layered, tubular, cellular, suture, and overlapping, as shown in Fig 1.4. Based on these design elements, researchers have endeavored to understand the complicated composite structures composed of the building blocks and their effects on mechanical behavior [58-61]. For example, as shown in Fig 1.5, Libonati et al. [62] manufactured bone-inspired composite samples and investigated their fracture behavior in mechanical tests. The bone-inspired design is proved to be crucial for toughness improvement and balance with material strength. Additionally, a computational framework is proposed by Libonati et al. [63] to predict the failure and behavior of bone-inspired composites. As another

enlightening natural material, bamboo is taken as a gradient structure with different volume fractions in each layer, as shown in Fig 1.6. Long et al. [64] conducted tensile tests and finite element analyses to show the effect of gradient topology on the mechanical behavior of the bamboo structures. The biological dataset in this thesis is inspired by bone and bamboo, which can be classified as cellular and gradient structures.

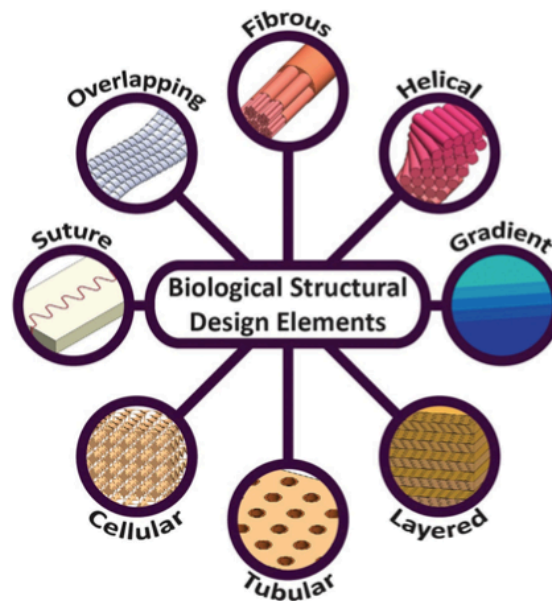


Fig 1.4: The eight most common biological structural design elements [57].

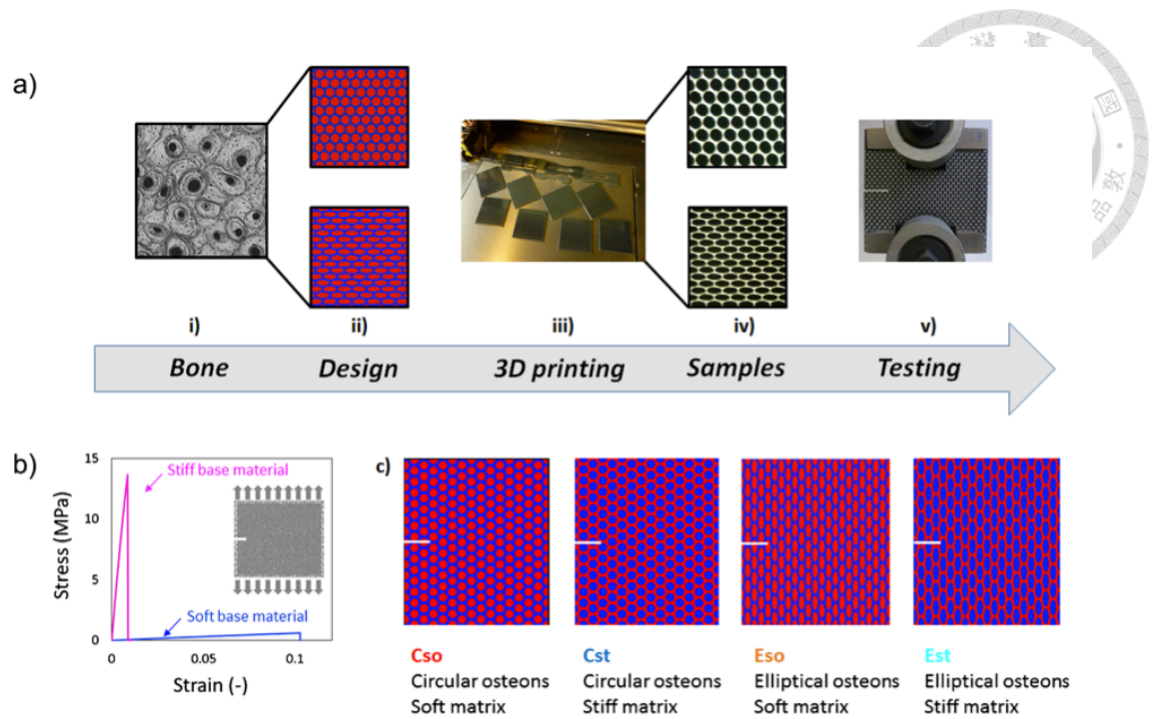


Fig 1.5: Bone-inspired composite. (a) Biomimetic approach. (b) Schematic of the sample geometry, applied loading condition, and corresponding stress-strain curve for the base materials. (c) Types of composites [62].

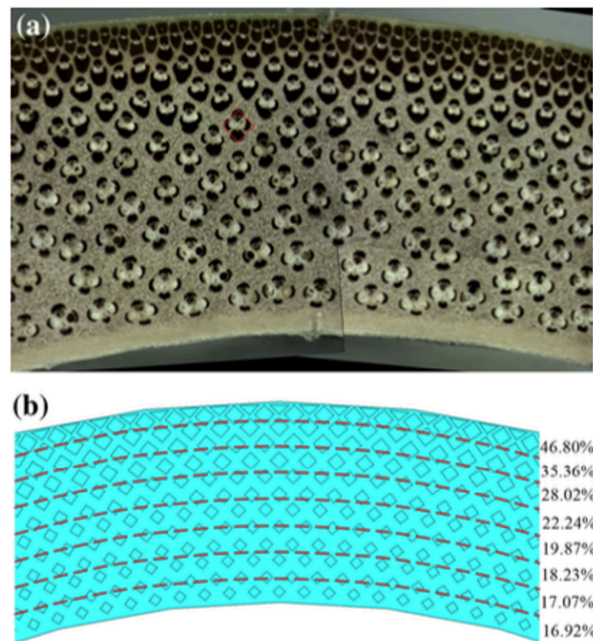
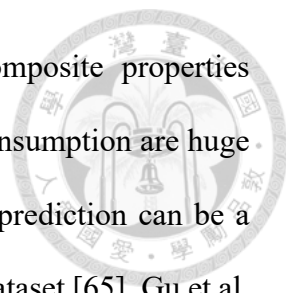


Fig 1.6: Natural bamboo with both gradient and cellular structures. (a) Cross-section of natural bamboo. (b) The volume fraction of each layer [64].



Although conducting experiments and FEM can predict composite properties accurately, the efficiency, high computational cost, and large time consumption are huge drawbacks. Hence, implementing machine learning-aided property prediction can be a significant breakthrough by training an ML model with a sufficient dataset [65]. Gu et al. [66] trained ML models with data labeled by the FEM model and predicted the strength and toughness of 2-D composites in a checkerboard system. Fig 1.7 depicts the flow chart of their ML approach for an 8 by 8 composite system. Their results demonstrate their ML models' capability to predict mechanical properties accurately and thus offer the opportunity to study more extensive systems.

Stress-strain curves contain information on material mechanical properties, such as strength, stiffness, and toughness. Yang et al. [67] predicted the entire stress-strain curves of binary composites by implementing principal component analysis and ML. Fig 1.8 presents the workflow of their modeling process for the 121-square-block composite plate system. Their study shows the potential of using machine learning methods to predict stress-strain curves.

There are several ways to improve the predictive performances of ML when the amount of data is limited. For instance, transfer learning, two-phase learning, and TGML are suitable methods to apply. Transfer learning is applied to improve a learner from one domain via transferring information from a related domain [68, 69]. Thus, transfer learning is often used when large data volumes are unavailable [70]. Jung et al. [71] generated a sufficiently large dataset with a low computational cost while less accuracy by homogenization theory to train the DNN model. Subsequently, transfer learning was applied to fine-tune the pre-trained DNN model with a relatively small but accurate FEA dataset. The framework of their transfer learning approach is depicted in Fig 1.9. Their results show that ML and transfer learning techniques can improve the accuracy and



efficiency of composite analysis while having a small dataset. In addition, two-phase learning is another ML technique to enhance the predictive model's performance. As its name implies, two-phase learning uses two algorithms together. The first algorithm is used for collecting essential characteristics from the dataset, and the second algorithm is used to predict the values. The approach shows great potential to produce correct and effective predictions [72]. Last but not least, theory-guided machine learning (TGML) is the other ML application in engineering problems. TGML relies on not only virtual or physical data but also the physical laws related to the problem (i.e., theory or domain knowledge). During the training process of ML models, a theory can be utilized to define physics-based features or any element in the model architecture. Zobeiry et al. [73] adopted TGML to predict the damage properties of composites. Their proposed strategy shows the effectiveness of TGML in reducing experimental efforts for damage characteristics in composites.

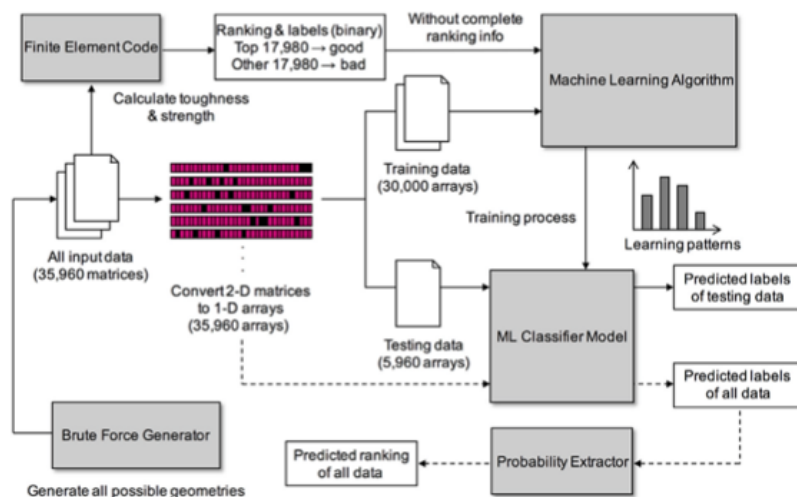


Fig 1.7: The flow chart of the ML approach using the linear model for an eight-by-eight system [66].

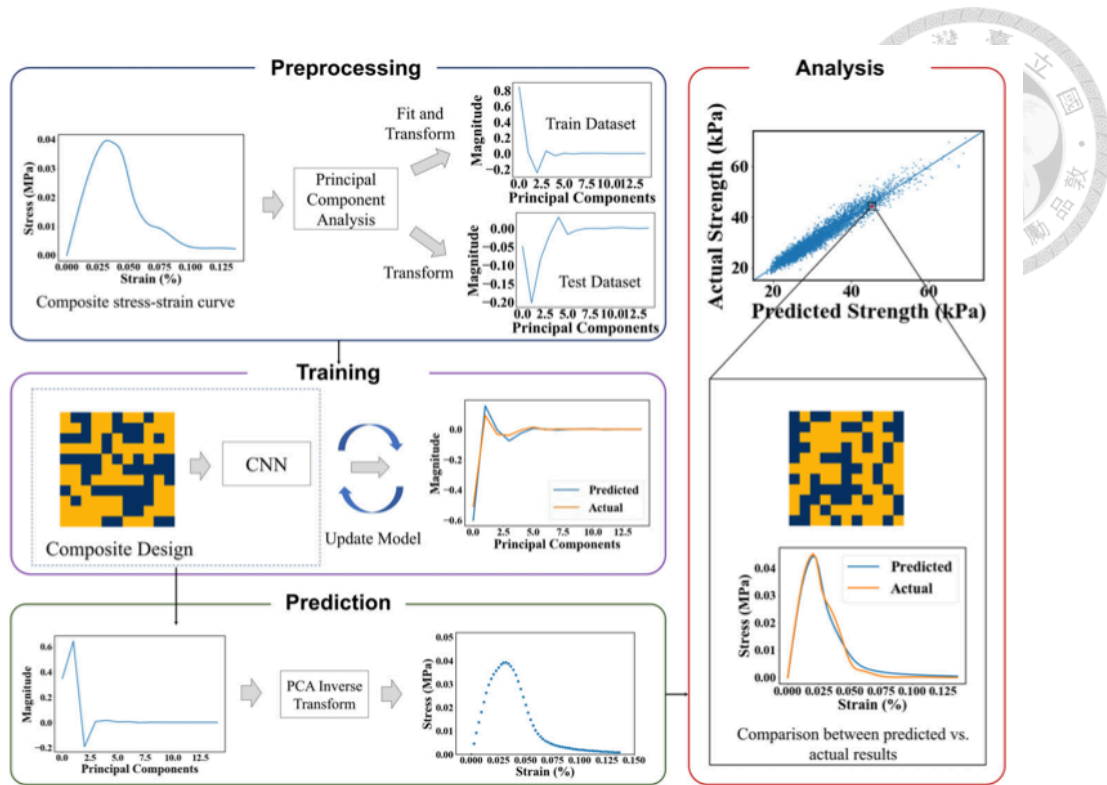


Fig 1.8: Workflow of the modeling process to predict stress-strain curve by CNN model

[67].

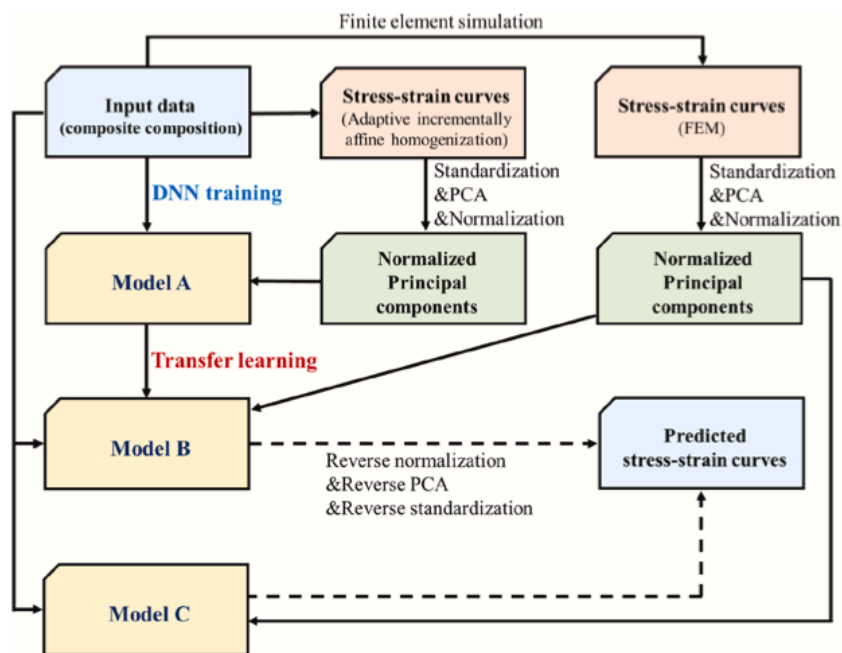


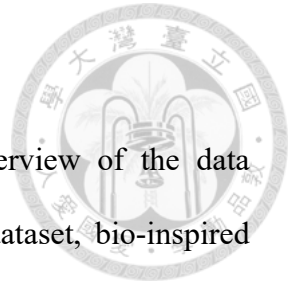
Fig 1.9: The overall workflow for applying transfer learning to predict stress-strain curves of fiber composites [71].

### 1.3 Objectives of the Thesis

It is noteworthy that machine learning is generally regarded as a powerful tool to utilize in real-life applications, including predicting the mechanical properties of materials. Hence, this study is aimed to implement machine learning techniques to provide predictions of stress-strain curves of composites. We divide this thesis into three parts to achieve our goal. Firstly, the predictive model based on deep neural networks will be trained with inputs of parameters of the material composition to offer stress-strain curve predictions of face-centered-cubic (FCC) structured representative volume element (RVE) SFRCs. Secondly, TGML and two-phase learning approaches are applied, and their effects on the results are compared. Thirdly, the stress-strain curves of bio-inspired layered structural composites will be predicted via another DNN model. We believe the work done in this thesis can provide an efficient method to get reliable predictions of stress-strain curves and thus help to understand more about materials.

## 1.4 Organization of the Thesis

The thesis is organized as follows: Chapter 2 gives an overview of the data generation and methods used in this thesis, in which the SFRC dataset, bio-inspired layered structural composite dataset, principal component analysis, and machine learning methods are discussed. Next, the setups and results of the predictive model for stress-strain curve predictions of face-centered-cubic-structured RVE SFRCs are presented in Chapter 3. Further, the procedures, results, and comparisons for applying TGML and two-phase learning to predict stress-strain curves of the SFRCs are described in Chapter 4. Additionally, the results of stress-strain curve predictions of bio-inspired composites are included in Chapter 5. Eventually, the conclusions of this thesis are mentioned in Chapter 6, along with some future works.





## Chapter 2 Materials and Methods

In this chapter, the FCC-structured SFRC dataset and the dataset of bio-inspired layered structural composites inspired by bone and bamboo are described. Further, principal component analysis and the theoretical background of machine learning methods are followed.

### 2.1 Data Generation

#### 2.1.1 FCC-Structured RVE SFRC Dataset

As described in Chapter 1, for SFRCs, the load applied to matrix materials is transferred to the fibers by fiber ends and the surfaces of fibers. Interphase, a zone of finite dimensions between the matrix and the fibers, exists in composite materials. This interphase has non-uniform mechanical properties depending on the manufacturing machine, materials, and process. Although the interphase thickness may seem small and insignificant, the interphase quality is directly linked to the properties of the composite material and its mechanical performance. Hence, the effect of interphase will be considered in the FEM simulations.

The FEM accurately evaluates the stress distribution and yield inside a composite when the composite is applied to mechanical load. If the numerical method is carefully executed, we take the results from the FEM as ground truth. In this study, the commercial software ABAQUS [74] is employed. As shown in Fig 2.1, we generated RVE models and arranged the fiber into an FCC configuration. To represent the behavior of bulk composites, we considered periodic boundary conditions for the RVE [75, 76]. Half of the RVE was used to conduct the analysis, and symmetric boundary conditions were applied to the back side of the RVE model. About 4,000 to 9,000 elements are required

for models with a different aspect ratio of the reinforcements to ensure convergence.

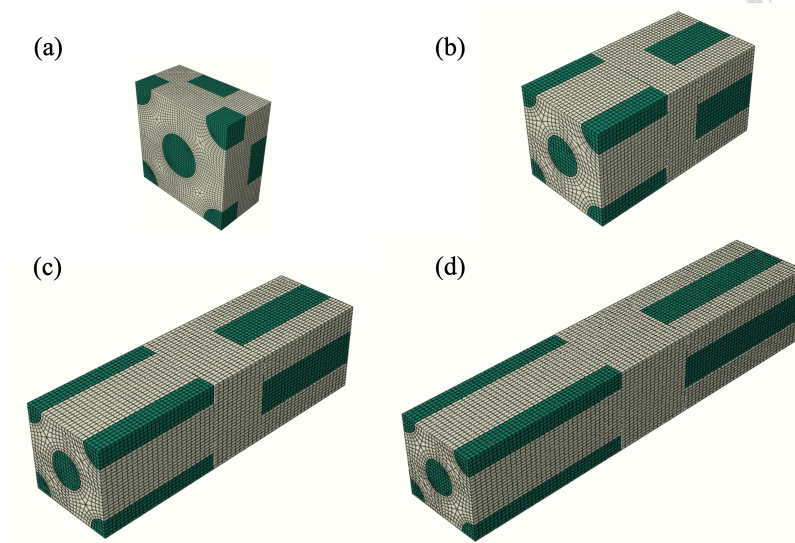


Fig 2.1: FCC-structured RVE SFRCs for FEM. (a) Aspect ratio = 1. (b) Aspect ratio = 4. (c) Aspect ratio = 7. (d) Aspect ratio = 10.

In normal conditions, fibers have much higher Young's moduli than the matrix materials in most composites. In this study, we assumed the composite was composed of an elasto-plastic matrix and linear elastic short fibers. The composite composition can be characterized by seven parameters related to the elastic properties (Young's modulus  $E_0$ ) and plastic properties (yield stress  $\sigma_y$ , hardening modulus  $k$ ) of the matrix, the elastic properties (Young's modulus  $E_1$ ) and aspect ratio (AR) of the reinforcements, as also the cohesive properties (normal and tangential stiffness components  $K$  and the peak values of the contact stress  $t_{max}$ ) of the interphase. The interphase properties are defined by the function of surface-based cohesive behavior in ABAQUS. The Poisson's ratio of the matrix, the Poisson's ratio of the reinforcements, and the volume fraction of the reinforcements are fixed to 0.35, 0.3, and 20%, respectively. After normalizing  $E_1$ ,  $\sigma_y$ , and  $k$  with  $E_0$ , we can transform the input parameters into a set of six parameters. The

normalized six parameters are taken as the input, and the stress-strain curve of the composite under uniaxial loading is taken as the output. The ranges of each input parameter considered in this study are presented in Table 2.1. These parameters greatly influence the stress-strain curves of SFRCs. Examples of the effect of cohesive-related parameters, i.e., the ratio of the stress of composites with the effect of interphase to that of tie (perfectly bonded) composites, are depicted in Fig 2.2. The relationship between these parameters and the stress-strain behavior is a problem of great complexity. Hence, implementing deep learning techniques is an excellent choice to predict the nonlinear behavior of stress-strain curves of SFRCs.

Table 2.1: Input parameters with given ranges for elasto-plastic composite.

$\sigma_y/E_0$	$k/E_0$	$E_1/E_0$	AR	$K$ (N/mm <sup>3</sup> )	$t_{max}$ (MPa)
0.005~0.025	0.01~0.1	1~200	1, 4, 7, 10	$10^5 \sim 10^7$	50~250

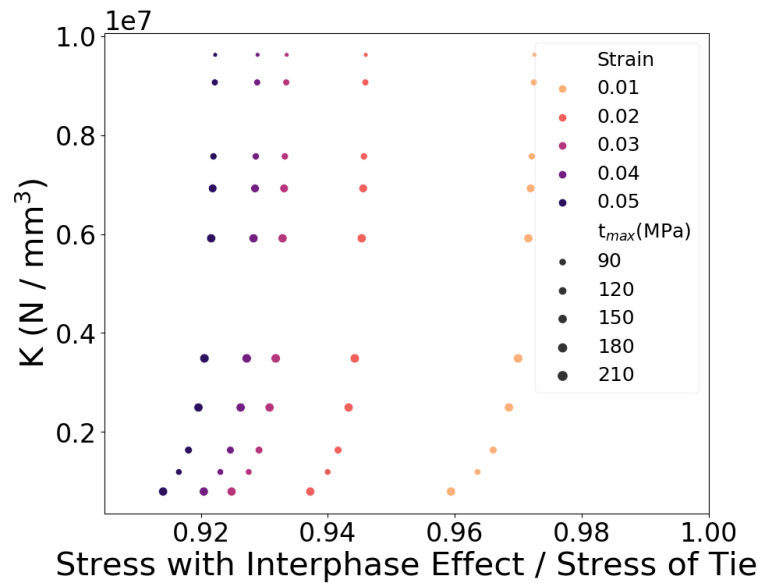


Fig 2.2: Illustration of the effect of interphase properties  $K$  and  $t_{max}$ .



### 2.1.2 Bio-Inspired Layered Structural Composite Dataset

The bio-inspired layered structural composite dataset was designed based on the bone-inspired topology combined with the concept of having various soft inclusion densities in each layer like bamboo. For all models in the dataset, the volume density of inclusion for the whole structure is fixed at 25.26%. In this study, we chose the elliptical pattern, which was proved to have the best mechanical performance in the study of Libotani et al. [63], and the volume fractions of each layer are 18.02%, 22.24%, 28.02%, 35.36%, and 46.80%, which are referred to that of Long et al.'s work [64]. However, unlike bamboo structures with gradationally distributed density in each layer, the volume fractions are shuffled in this work, as shown in Fig 2.3.

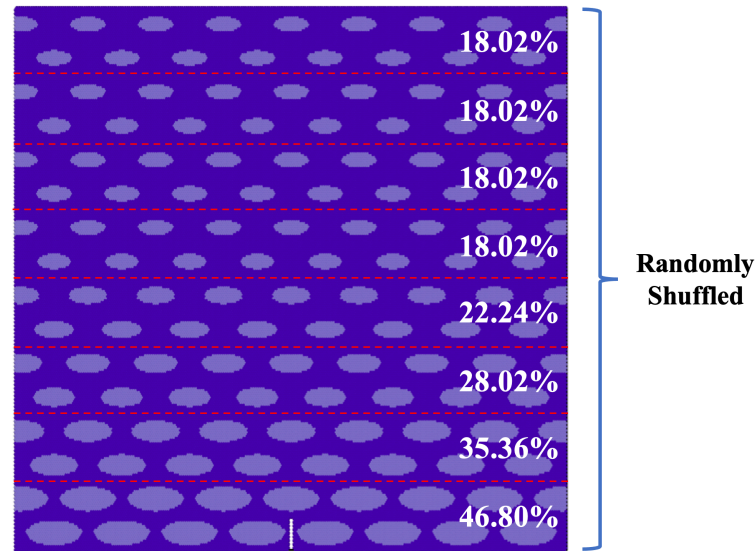


Fig 2.3: Illustration of the bio-inspired layered structural composite.

As depicted in Fig. 2.4(a), the topology comprises the inclusion and matrix with a dimension of 25600 x 25600 x 1 cubic unit length. Firstly, the matrix is divided into 8x8 squares. Each square will have two elliptical inclusions with an aspect ratio (AR) of 2.25.

Hence, there will be 128 elliptical inclusions in total for each model. Secondly, the whole model is divided into 8 layers, and the area of the elliptic inclusion is calculated according to the density  $\rho$  in each layer. The length of the elliptical inclusion  $a$  is obtained as follows:

$$AR = \frac{b}{a} = 2.25 \quad (2-1)$$

$$\rho = \frac{2 \times 2.25a \times a \times \pi}{L^2} \quad (2-2)$$

$$a = \sqrt{\frac{\rho L^2}{4.5\pi}} \quad (2-3)$$

After knowing all parameters we need to construct the composite structures, the discrete particle models are created by in-house Python codes.

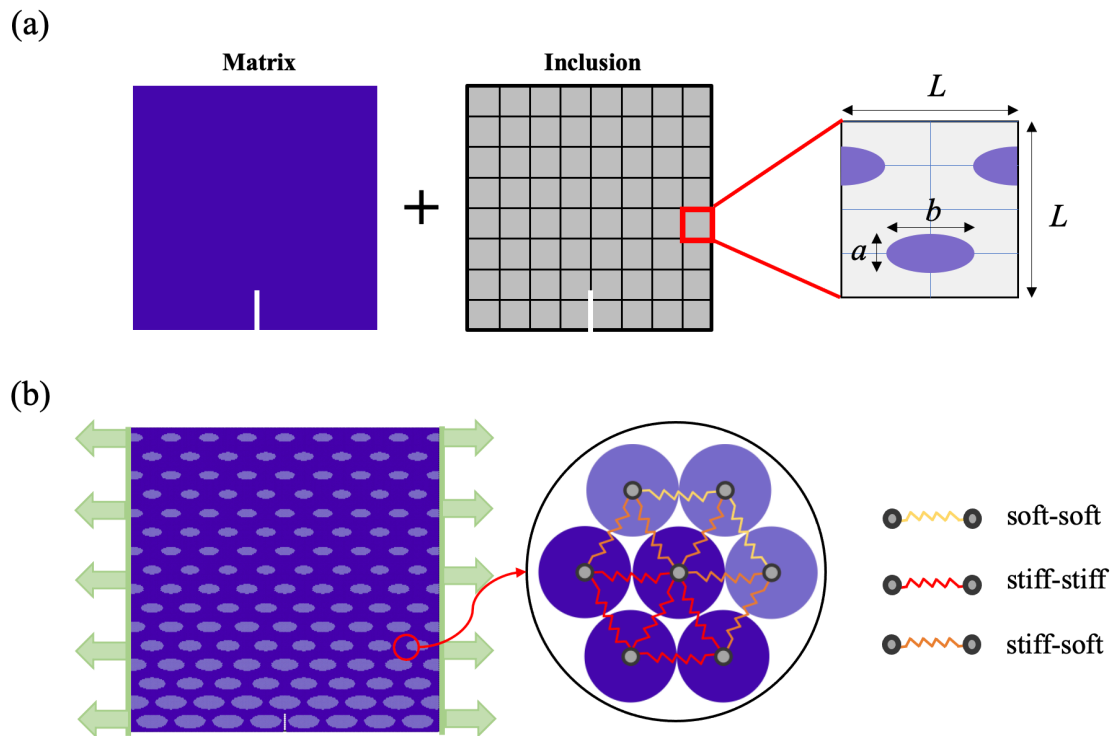


Fig 2.4: (a) Illustration of the composition of the composite. (b) Illustration of uniaxial tensile test simulation and LSM model.

We adopted the 2D lattice spring model (LSM) with hexagonal packing particles and a triangular spring network to predict the bio-inspired composite materials' behavior. Each particle interacts with its nearest neighbors through harmonic springs (see Fig. 2.4(b)). Stiff, soft, and interphase harmonic springs are the bonds connecting the stiff-stiff particles, the soft-soft particles, and the stiff-soft particles, respectively. The parameters of the harmonic springs referred to parameters in our previous work [61] are shown in Table 2.2. The potential energy in a harmonic spring is denoted as a function of the spring length  $l$ , the assigned stiffness of  $k$ , the equilibrium spring length  $l_0$ , and the elongated spring length at breakage  $l_b$ :

$$U(l) = \begin{cases} \frac{1}{2}k(l - l_0)^2, & l < l_b \\ 0, & l > l_b \end{cases} \quad (2-4)$$

where  $l_0$  is 100 unit length. Once the spring is extended longer than  $l_b$ , the spring breakage dissipates energy stored in the spring, and we eliminate the broken spring from the model.

Table 2.2: Parameters of the Harmonic Springs for Different Phases.

	stiff-stiff	soft-soft	stiff-soft
spring constant ( $k$ )	$100k$	$k$	$6.25k$
spring cutoff length ( $l_b$ )	$1.01l_0$	$1.10l_0$	$1.04l_0$
potential energy ( $U$ )	$5 \times 10^{-3} kl_0^2$	$5 \times 10^{-3} kl_0^2$	$5 \times 10^{-3} kl_0^2$

We employed the LAMMPS code [77] to conduct uniaxial tensile test simulations of the composite models. A 250 x 1500 notch is added to each model to simulate the mode I fracture. By displacing the left and right boundaries with  $2.56 \times 10^{-3}$  unit length per step and conducting energy minimization for every strain of 0.001, the loading-minimization cycles can ensure that the model's load transfer is correct. The stress-strain curve data is collected during the displacement-controlled simulations.

## 2.2 Principal Component Analysis

Principal component analysis (PCA), a dimensionality reduction method, identifies an orthonormal basis and projects the data into a lower dimension [78]. The PCA algorithm involves the following steps:

1. Standardize the n-dimensional dataset.
2. Construct the covariance matrix.
3. Calculate the eigenvectors and eigenvalues from the covariance matrix.
4. Sort the eigenvalues by decreasing order to rank the corresponding eigenvectors.
5. Choose  $m$  eigenvalues that correspond to the  $m$  largest eigenvalues, where the new feature subspace's dimensionality is  $m$  ( $m \leq n$ )
6. Construct a projection matrix  $J$  from the first  $m$  eigenvectors.
7. Transform the n-dimensional input by the projection matrix  $J$  dataset  $D$  to obtain the new  $m$ -dimensional feature subspace.

Implementing PCA expresses a large set of variables with a smaller one but retains most of the information in the large set. A smaller set of variables is easier to explore and visualize, making data analyses much more efficient and straightforward. Hence, for a large dataset like stress-strain curves, PCA is an appropriate method to reduce the

variables of a dataset while preserving as much explanation of the data as possible.



## 2.3 Machine Learning Approaches

### 2.3.1 Fundamental Concepts of Machine Learning

Machine learning is usually defined as a method that learns from data and experience to find patterns in the dataset and the operating rules and finally achieve artificial intelligence. As shown in Fig 2.5, traditional programming is a process that humans input rules or programs and data to be processed and then get the answers. On the other hand, in machine learning, the algorithm automatically formulates the rules from the data. These rules can further be applied to newly observed data to produce new predictions.

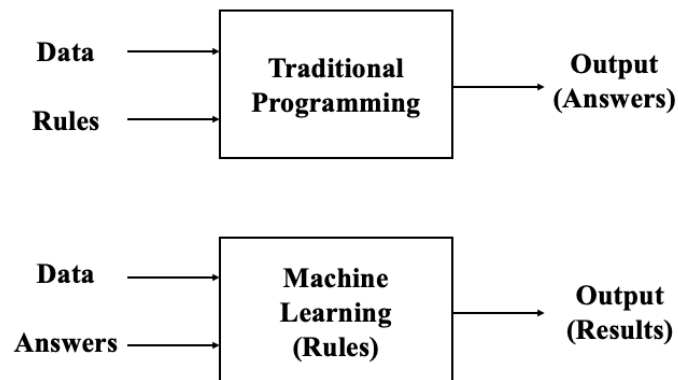
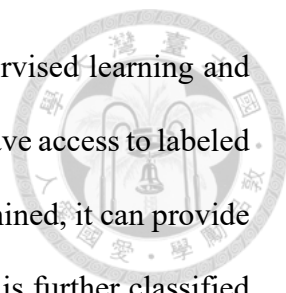


Fig 2.5: Comparison between traditional programming and machine learning.

The three main elements of machine learning are representation, evaluation, and optimization [79]. Representation means that the choice of the hypothesis space determines whether it can be learned. Therefore, the way to represent the input or the selection of the features to use is what matters. Furthermore, an evaluation function differentiates good models from bad ones. Last but not least, optimization is the algorithm to search for the optimal model.



When it comes to the different types of machine learning, supervised learning and unsupervised learning play crucial roles. In supervised learning, we have access to labeled input-output pairs that help train the model. Once the model is determined, it can provide predictions from new and unknown data labels. Supervised learning is further classified into two subgroups: regression and classification tasks. Regression tasks predict a continuous quantity, while classification tasks assign observations into discrete categories. On the other hand, unsupervised learning is an entirely different type of task. There are many situations where the “right answers” are unobservable, infeasible to obtain, or the “right answers” do not even exist. Hence, unsupervised learning helps identify the pattern or structure in data. Those models are often trained for clustering and dimensionality reduction without provided labels.

### **2.3.2 Deep Learning**

Deep learning is a specific subdivision of machine learning in AI that learns the pattern from data by successive layers of incremental meaningful representations. The word “deep” in deep learning means that multiple layers are used in the network. Classical machine learning techniques, or so-called shallow learning, only transform the input data into one or two successive representation spaces by transformations such as decision trees. However, such techniques cannot attain the sophisticated representations required by intricate problems. On the other hand, deep learning automatically learns all the features by the layer-by-layer method in which increasingly complex representations are developed and by learning all layers of representation jointly. It substitutes complex multistage pipelines with a simple, straightforward, and end-to-end deep learning model, thus significantly simplifying the machine learning workflows.

### 2.3.2.1 Deep Neural Network (DNN)

A deep neural network is composed of multi-layered artificial neural networks (ANNs) inspired by information delivering and scattered communication nodes in biological systems, as illustrated in Fig 2.6. These artificial neurons obtain weighted inputs from other nodes and generate output through a differentiable activation function. The following expressions describe the mathematical notation of the inner processing by the neuron:

$$\begin{cases} u = \sum_{i=1}^n w_i x_i - b \\ z = g(u) \end{cases} \quad (2-5)$$

where  $x_i$  is  $i^{th}$  input,  $w_i$  is the weight of the  $i^{th}$  input,  $b$  is the bias,  $g(\cdot)$  is the activation function,  $u$  is the activation potential, and  $z$  is the output of the neuron. We can see a DNN model as a series of chained functions:

$$y = f(x) = f^{(N)}(f^{(N-1)}(\dots f^{(2)}(f^{(1)}(x)))) \quad (2-6)$$

where  $N$  is the number of layers of the deep learning model, and  $y$  stands for the final output. As shown in Fig 2.7, Chollet clearly illustrated the training loop [80]. The goal of using a deep neural network is to map inputs to targets via a deep sequence of data transformations (layers). By observing many examples of inputs and targets, these layers store the weights of the inputs. In each training loop, the loss function measures how far the outputs are from the actual targets and computes a distance score (i.e., loss score), capturing how well the network has done on this specific example. Next, the optimizer updates the weights according to the loss score, which implements the backpropagation algorithm to find a network with a minimal loss.

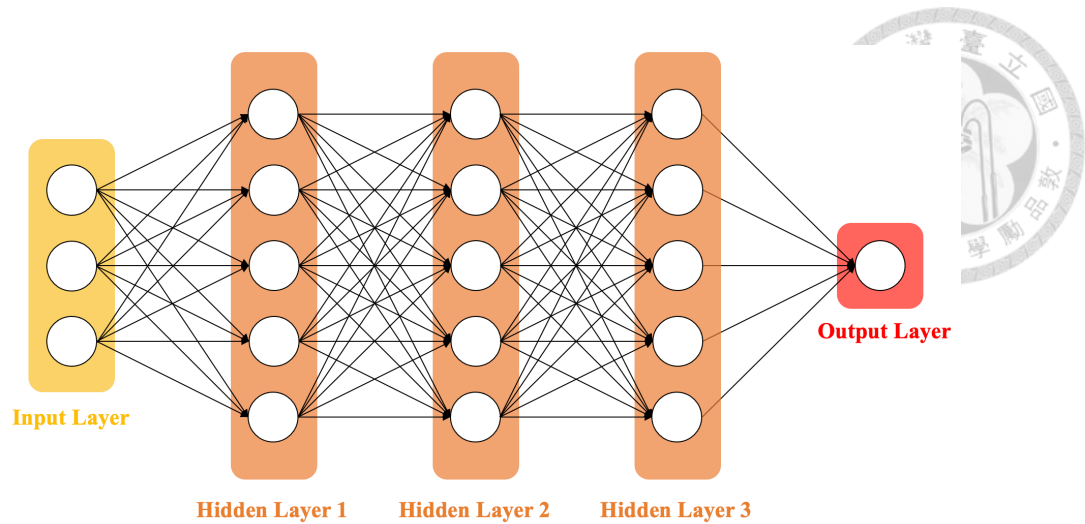


Fig 2.6: Illustration of a DNN model.

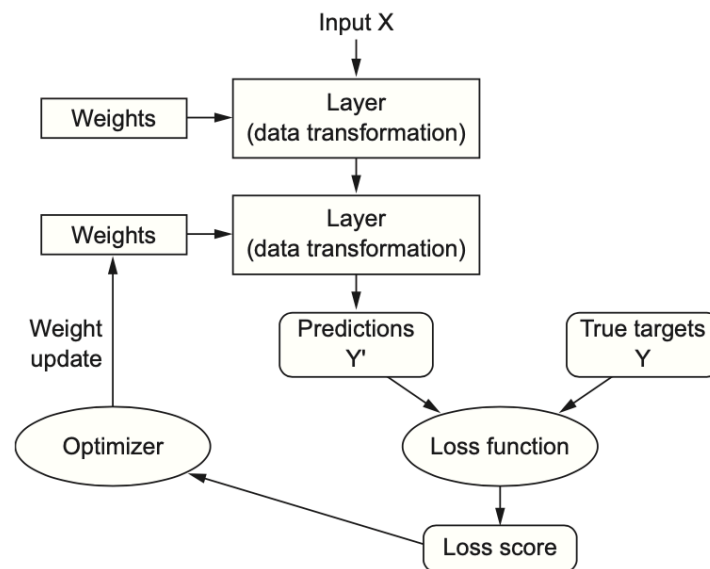


Fig 2.7: Illustration of the training loop. [80]

### 2.3.2.2 Activation Layer

Activation layers are layers with activation functions that define how the output is transformed by the weighted sum of the input from a node or nodes in a neural network. Many activation functions are nonlinear to learn the complex relationships in the data.



Hence, deep learning models can deal with more sophisticated tasks. For instance, rectified linear unit (ReLU), one of the most commonly used activation functions in deep learning, is a piecewise linear function that will output the input directly if it is positive; otherwise, it will output zero. This function solves the vanishing gradient problem; however, it occurs the dying ReLU problem [81]. Thus, activation functions like leaky rectified linear unit (Leaky ReLU), exponential linear unit (ELU) [82], and Gaussian error linear unit (GELU) [83] are introduced to avoid the dying ReLU problem. The equations of ReLU, Leaky ReLU, ELU, and GELU are shown in Equations 2.7 to 2.10, where  $x$  is the input tensor to a neuron. These activation functions are used in the grid-search hyperparameter tuning to optimize the DNN architecture in this research.

- ReLU function:

$$f(x) = \max(0, x) \quad (2-7)$$

- Leaky ReLU function:

$$f(x) = \begin{cases} x & \text{if } x > 0 \\ \alpha x & \text{if } x \leq 0 \end{cases} \quad (2-8)$$

- GeLU function:

$$f(x) = 0.5x \left(1 + \tanh\left(\sqrt{\frac{2}{\pi}}(x + 0.044715x^3)\right)\right) \quad (2-9)$$

- ELU function:

$$f(x) = \begin{cases} x & \text{if } x > 0 \\ \alpha(e^x - 1) & \text{if } x < 0 \end{cases} \quad (2-10)$$

### 2.3.2.3 Performance Metrics

Different performance metrics are used to evaluate the results of the machine learning models depending on the learning tasks. For regression models, mean squared error (MSE), mean absolute error (MAE), and r-squared score ( $R^2$ ) are the commonly used evaluation methods to measure the accuracy of the predictive results. MSE shows the mean of the distance from each point to the predicted regression model. The squaring is crucial to reduce the complexity of negative signs. When the model is closer to actual data, the MSE is smaller and thus is more accurate.

$$MSE = \frac{1}{n} \sum_{i=1}^n (y_i - \hat{y}_i)^2 \quad (2-11)$$

MAE is an arithmetic average of the absolute errors, which is described by the following expressions:

$$MAE = \frac{1}{n} \sum_{i=1}^n |y_i - \hat{y}_i| \quad (2-12)$$

Denoted as  $R^2$ , the coefficient of determination is a statistical measure representing the variance proportion for a dependent variable explained by the variables in the regression model. In other words,  $R^2$  indicates how well the data fit the regression model. The more accurate the predictive model is, the closer the value of  $R^2$  score is to 1.

$$R^2 = 1 - \frac{\text{Explained Variance}}{\text{Total Variance}} = 1 - \frac{\sum_{i=1}^n (y_i - \hat{y}_i)^2}{\sum_{i=1}^n (y_i - \bar{y}_i)^2} \quad (2-13)$$



## Chapter 3 Stress-strain Curve Predictions of SFRCs

In this chapter, the detailed training setup and the results of the predictive model are presented. For predicting the stress-strain curves, the regression model is based on DNN.

Fig 3.1 shows the process of predicting the stress-strain behavior of the SFRCs. The ML model training and analyses of the results are done by Python codes.

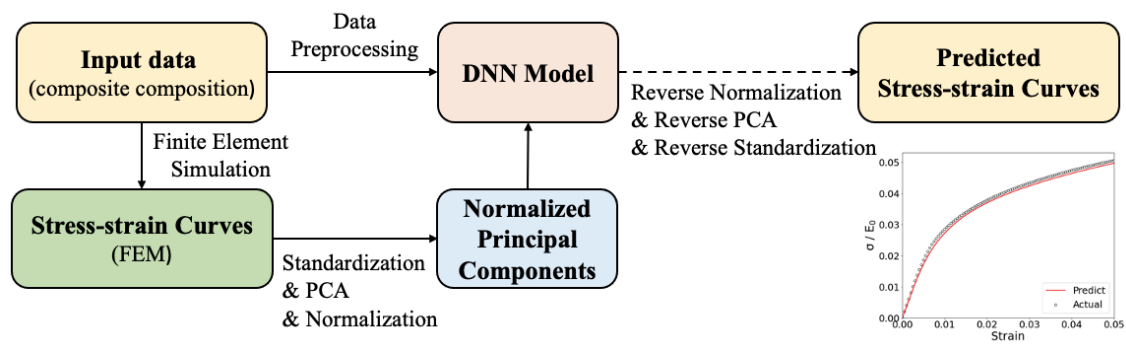


Fig 3.1: Illustration of the workflow to predict stress-strain curves of SFRCs.

### 3.1 Dataset Preparation

We collect our data by finite element simulation as described in section 2.1.1. Because of the limit of computational resources, 814 samples were randomly assigned with the six material parameters to perform FEM simulation. The input and output formats are depicted in Fig 3.2. In this work, the FEM results are taken as ground truth. The FEM dataset of 814 samples was divided into training, validation, and testing sets at a ratio of 8:1:1. Both training and validation sets were used in the training stage. In contrast, the testing set was not involved in training but only used to evaluate the model performance. We normalized each input parameter to values between 0 and 1 before training. The distribution of each parameter in the dataset is shown in Fig 3.3. The output data, the stress evaluated at 101 strain points from the stress-strain curves, are represented

as arrays of stress values (referred to as stress vectors). Using strain vectors adds no useful information to the model since strain vectors are constant for all inputs. Firstly, the stress vectors are standardized to center at mean of 0 with standard deviation of 1 by column. Using standardization retains valuable information about outliers and lowers the sensitivity of machine learning algorithms to them. Next, the dimensionality of the stress vectors is reduced via PCA. PCA is only fit on training data to get the orthogonal basis, which is defined by principal component vectors. Based on this basis, training and validation data are transformed. The stress vectors are transformed into 5-dimension vectors composed of the first 5 principal components, as demonstrated in Fig 3.2. Defined as the sum of eigenvalues normalized by the sum of all eigenvalues ( $\sum_{i=1}^5 \lambda_{jj} / \sum_{i=1}^{101} \lambda_{jj}$ ), the cumulative explained variance is 99.99%. The cumulative explained variance ratio with respect to the number of dimensions is depicted in Fig 3.4. Subsequently, we normalize the reduced dimension data (the 5 most important principal components) to values between 0 and 1. By the procedures mentioned above, the DNN model can learn more efficiently in a lower dimension space to obtain better predictive performance with less training data.

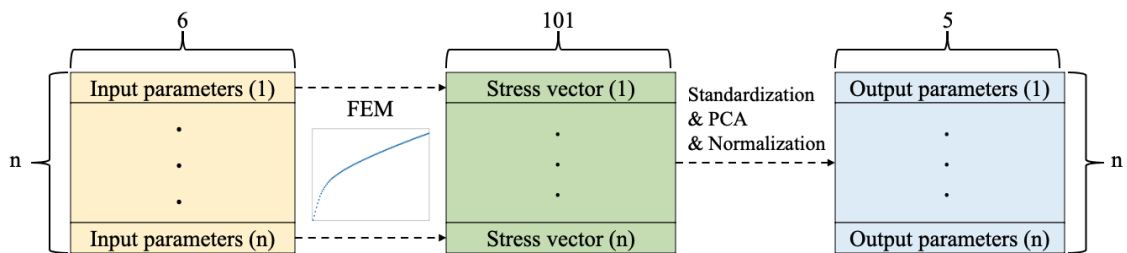


Fig 3.2: Input (material properties) and output (stress-strain curve data transformed to 5-dimension data via PCA) formats.

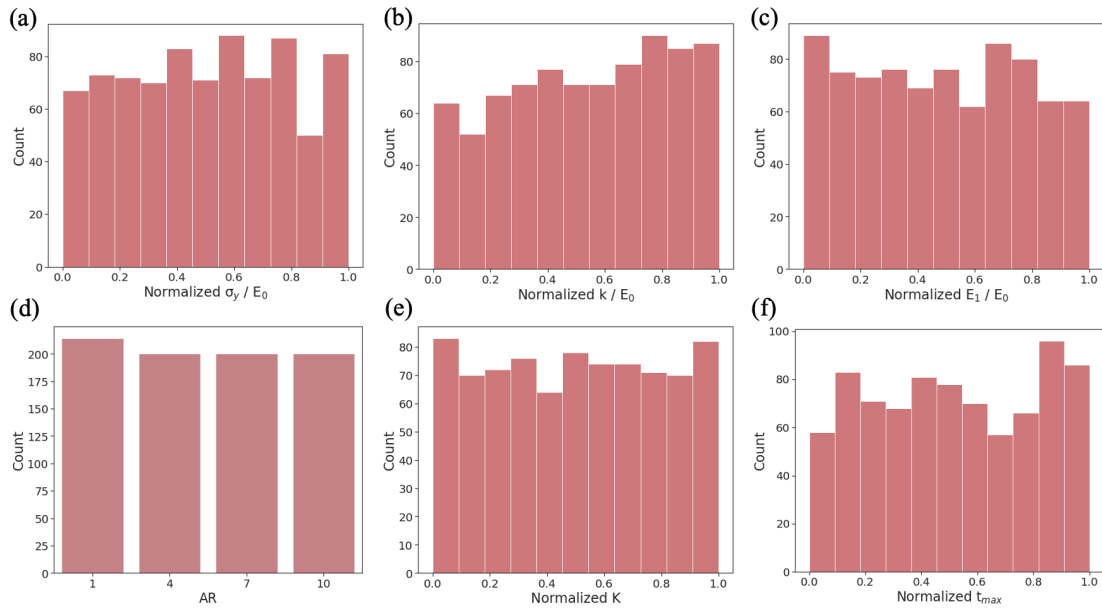


Fig 3.3: Distribution of each composite composition. (a)  $\sigma_y/E_0$  (b)  $k/E_0$  (c)  $E_1/E_0$  (d) AR  
(e)  $K$  (f)  $t_{max}$ .

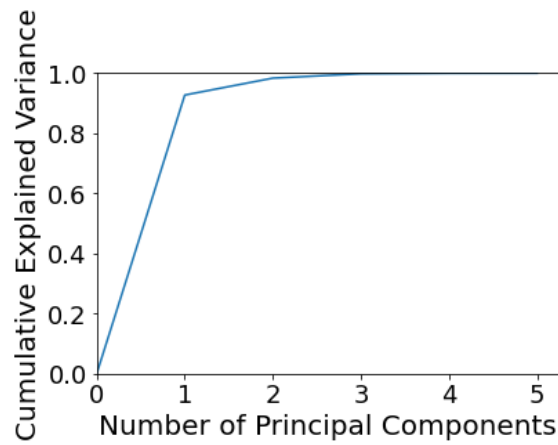


Fig 3.4: Cumulative explained variance ratio with respect to the number of dimensions.

### 3.2 DNN Model Setup

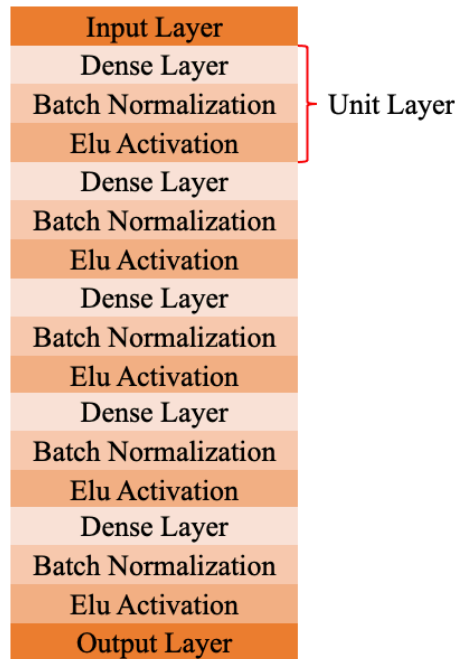


Fig 3.5: DNN architecture.

We chose a DNN architecture to employ a flexible model to learn the complicated stress-strain behavior of the composites. As shown in Fig 3.5, the DNN architecture is composed of a series of unit layers which includes a dense layer, batch normalization, and activation function in each unit layer. Batch normalization is a method known for its capability to make training faster and more stable [84].

Each eigenvalue obtained via PCA represents the explained variance in each principal component. However, conventional loss functions for regression problems, such as the mean squared error loss function, cannot communicate with our DNN model that some principal components are more important than others. Hence, we show our DNN model the various importance of principal components by constructing a customized loss function to weight errors in each principal component by the correspondent eigenvalue.

The weighted mean squared error (WMSE) is defined as follows:



$$WMSE = \frac{1}{n} \sum_{i=1}^n \sum_{j=1}^5 \lambda_{jj} (Y_{j,i}^{true} - Y_{j,i}^{pred})^2 \quad (3-1)$$

To optimize the DNN architecture, we implement the grid-search technique to find the best combination of hyper-parameters. The architecture with the lowest average weighted mean squared error after five epochs was chosen in the following search space:

- Number of neurons in each dense layer = [40, 50, 60, 70, 80, 90, 100]
- Number of hidden unit layers = [3, 4, 5, 6]
- Activation function = [ReLU, LeakyReLU, GeLU, ELU]

The results of the grid-search after five epochs were obtained over 5-fold cross-validation, as demonstrated in Table 3.1 to Table 3.4.

Table 3.1: Average WMSE results with ReLU activation function. The minimum value is highlighted in red.

ReLU Activation Function		Number of hidden unit layers			
		3	4	5	6
Number of neurons	40	0.007150	0.007309	0.008678	0.009210
	50	0.007094	0.007605	0.008248	0.008456
	60	0.006846	0.007216	0.007783	0.008584
	70	0.006771	0.006998	0.007884	0.008465
	80	0.007234	0.007040	0.007666	0.008867
	90	0.006871	0.006364	0.007207	0.007879
	100	0.006563	0.006854	0.007082	0.008302



Table 3.2: Average WMSE results with LeakyReLU activation function. The minimum value is highlighted in red.

LeakyReLU Activation Function		Number of hidden unit layers			
		3	4	5	6
Number of neurons	40	0.005208	0.004714	0.004375	0.004654
	50	0.004583	0.004480	0.004334	0.004857
	60	0.004979	0.004450	0.004169	0.004516
	70	0.004697	0.004120	0.004313	0.004356
	80	0.004426	0.004315	0.004598	0.004436
	90	0.005339	0.004964	0.004175	0.004570
	100	0.005376	0.004909	0.004970	0.005181

Table 3.3: Average WMSE results with GeLU activation function. The minimum value is highlighted in red.

GeLU Activation Function		Number of hidden unit layers			
		3	4	5	6
Number of neurons	40	0.006153	0.006033	0.006245	0.007781
	50	0.004900	0.005945	0.006135	0.006890
	60	0.005089	0.005317	0.005903	0.005834
	70	0.004919	0.005276	0.005470	0.006387
	80	0.004880	0.005136	0.005721	0.005572
	90	0.004722	0.005033	0.005498	0.005806
	100	0.004856	0.005563	0.005657	0.005319

Table 3.4: Average WMSE results with ELU activation function. The minimum value is highlighted in red.

ELU Activation Function		Number of hidden unit layers			
		3	4	5	6
Number of neurons	40	0.003831	0.003582	0.003496	0.003666
	50	0.003541	0.003433	0.003404	0.003599
	60	0.003663	0.003346	0.003343	0.003219
	70	0.003441	0.003251	0.003753	0.003516
	80	0.003536	0.003185	0.003114	0.003213
	90	0.003469	0.003285	0.003739	0.003533
	100	0.004119	0.004098	0.003422	0.003453

The chosen architecture has 80 neurons in each dense layer, five hidden unit layers, and ELU as an activation function. This DNN architecture has 27,685 trainable parameters. The Adam optimizer, a popular algorithm in the field of deep learning, was employed to train the DNN model [85]. Also, we set the batch size to 8 in this model. Moreover, early stopping was adopted once the validation loss did not improve within 20 steps to avoid over-fitting.

After the training, the 101-dimensional stress-strain curves were obtained from the output, i.e., the 5-dimensional normalized principal components, via reverse normalization, reverse PCA, and reverse standardization.

### 3.3 Results and Discussion

Table 3.5: Evaluation metrics of predictive models.

Properties	R <sup>2</sup> score			MSE			MAE		
	Train	Valid.	Test	Train	Valid.	Test	Train	Valid.	Test
Stiffness	0.9343	0.9368	0.9331	0.0702	0.0616	0.0717	0.1911	0.1657	0.1944
Stress when strain = 0.01	0.9478	0.9498	0.9337	2.68E-06	2.35E-06	3.20E-06	1.14E-03	1.00E-03	1.05E-03
Stress when strain = 0.02	0.9579	0.9620	0.9497	4.46E-06	3.80E-06	5.33E-06	1.59E-03	1.36E-03	1.51E-03
Stress when strain = 0.03	0.9600	0.9642	0.9551	5.68E-06	4.91E-06	6.39E-06	1.83E-03	1.61E-03	1.73E-03
Stress when strain = 0.04	0.9612	0.9662	0.9540	6.56E-06	5.64E-06	7.79E-06	1.97E-03	1.80E-03	1.90E-03
Stress when strain = 0.05	0.9620	0.9672	0.9504	7.31E-06	6.35E-06	9.54E-06	2.08E-03	1.98E-03	2.10E-03

We selected the model that had a minimum loss on validation data as the final predictive model. The loss history during training, examples of predictive stress-strain curves, and regression scatter plots of the predictive model are plotted in Fig 3.6 to Fig 3.13. Table 3.5 demonstrates the evaluation metrics of R<sup>2</sup> score, MSE, and MAE corresponding to training, validation, and testing data. The maximum relative error of each stress-strain curve is defined as follows:

$$\text{Maximum Error} = \max\left(\frac{\sigma_1^{\text{Pred}} - \sigma_1^{\text{FEM}}}{\sigma_1^{\text{FEM}}}, \dots, \frac{\sigma_{100}^{\text{Pred}} - \sigma_{100}^{\text{FEM}}}{\sigma_{100}^{\text{FEM}}}\right) \quad (3-2)$$

The histogram of 82 testing data's maximum error is presented in Fig 3.14. From the results, we can see impressive performances of all R<sup>2</sup> scores higher than 0.9 and maximum error lower than 10% for most of the predicted stress-strain curves compared to ground truth (FEM). These results show that DNN models have great potential to be used as surrogate models to provide accurate predictions of stress-strain curves from material parameters efficiently.

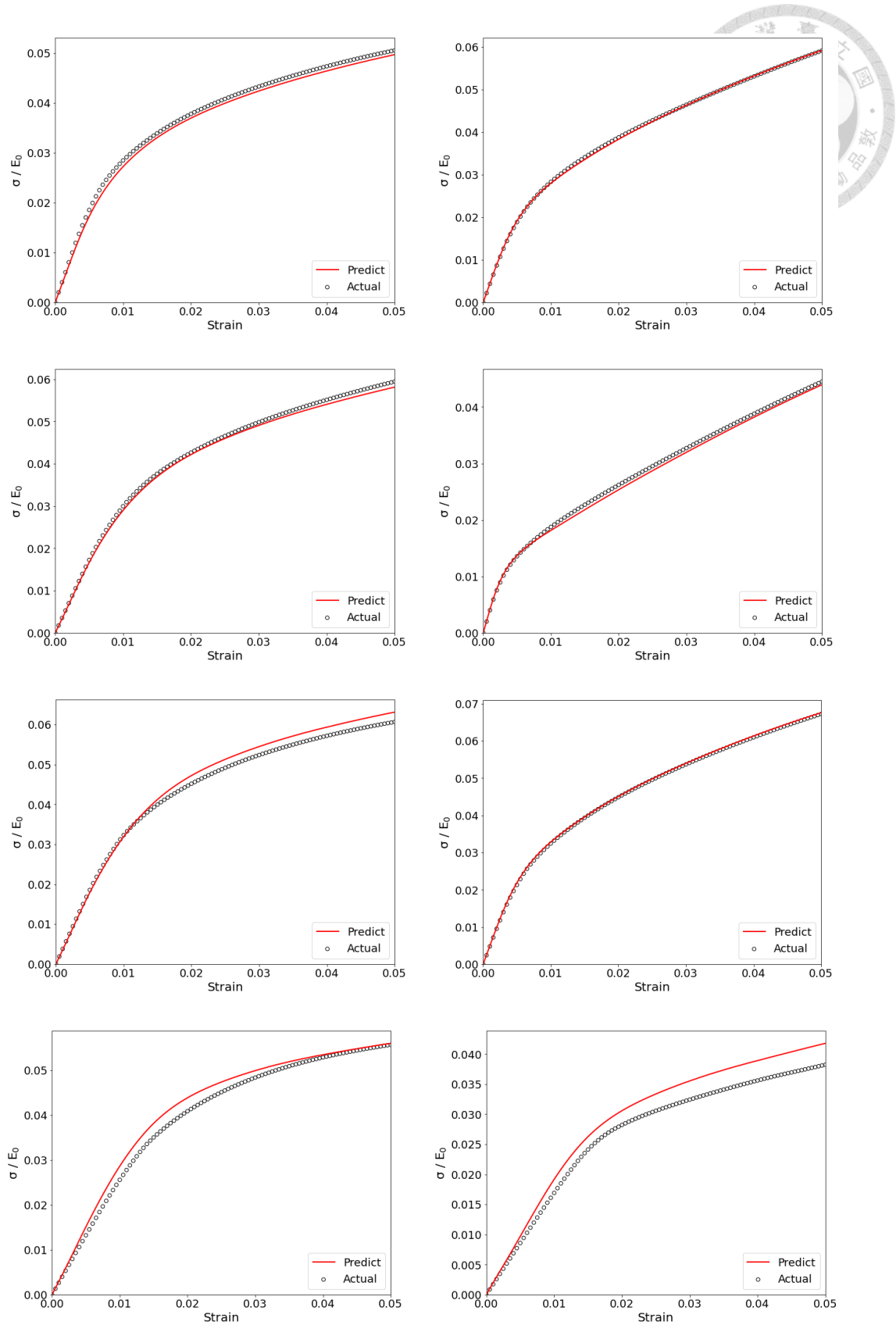


Fig 3.6: 8 comparisons between the predicted stress-strain curve and the actual stress-strain curve (FEM).

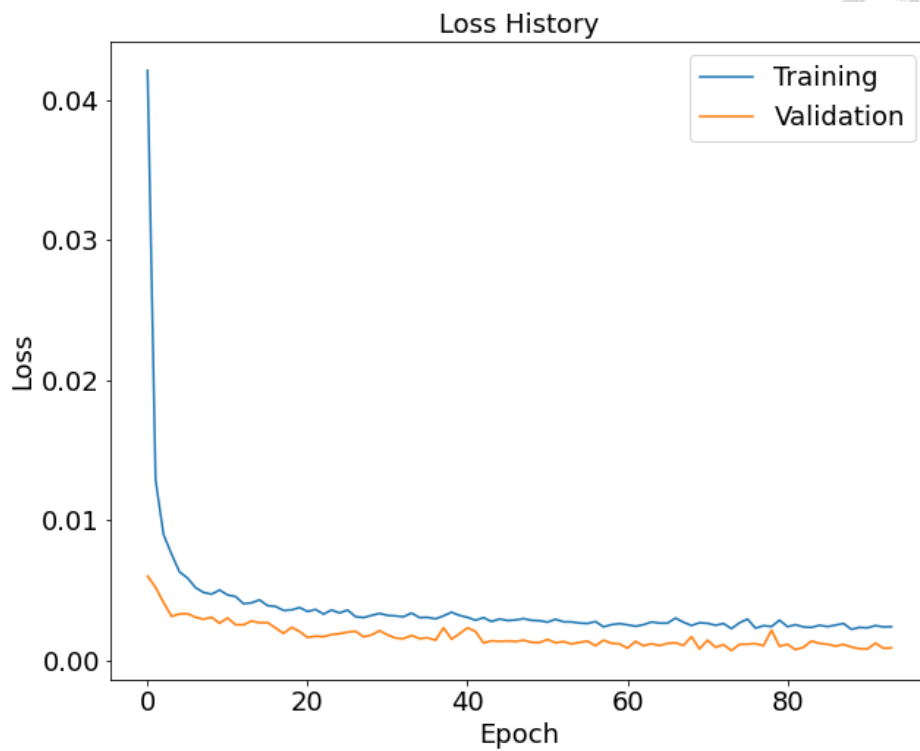


Fig 3.7: Loss history of the predictive model.

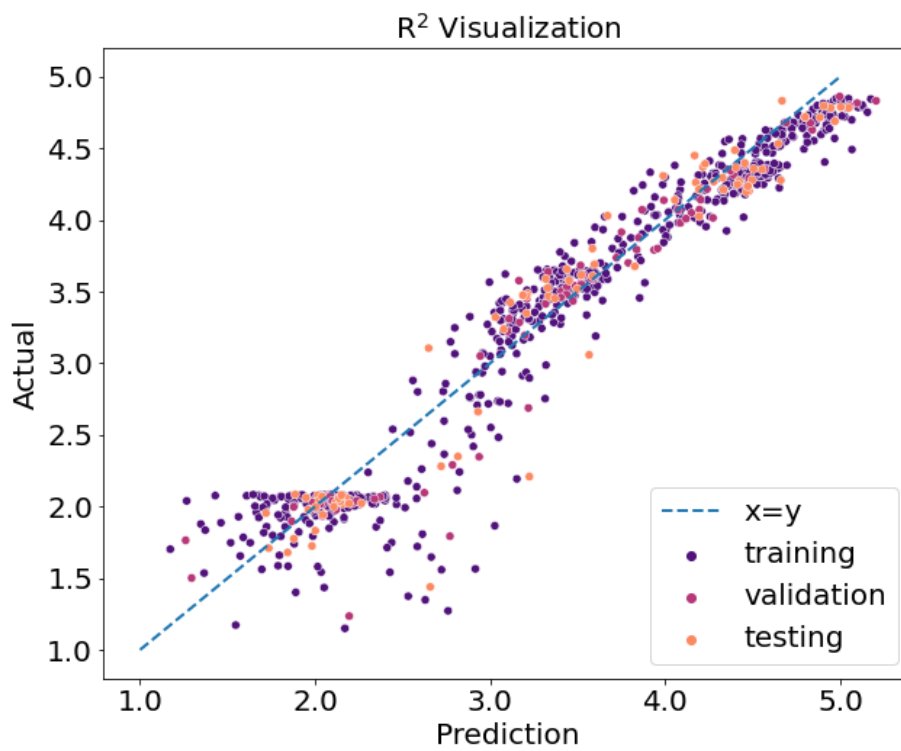


Fig 3.8: R<sup>2</sup> visualization plot of stiffness.

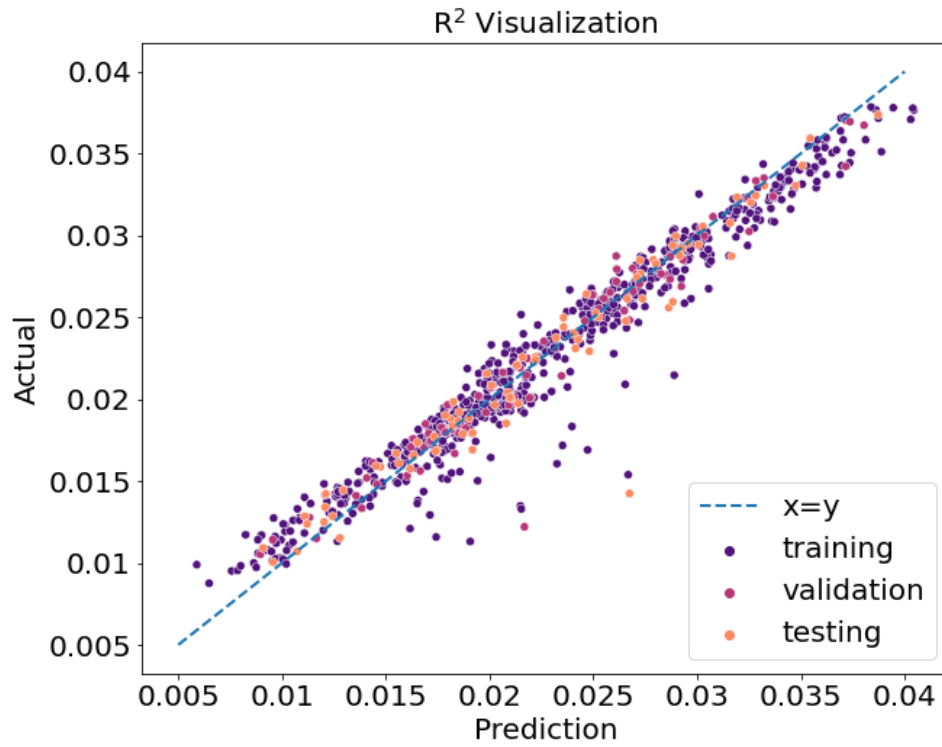


Fig 3.9: R<sup>2</sup> visualization plot of stress when strain = 0.01.

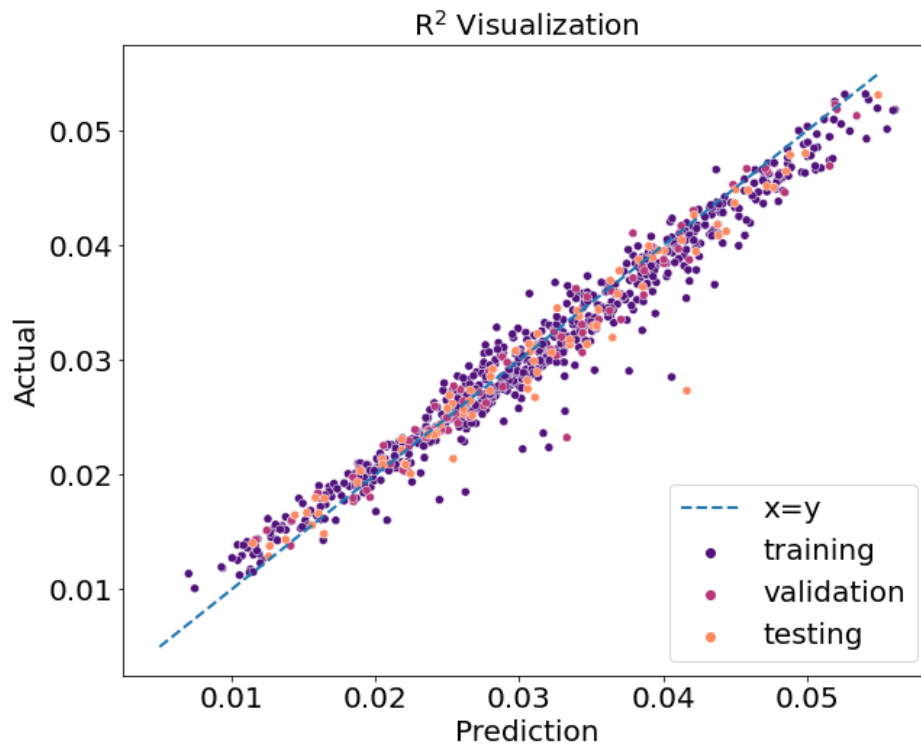


Fig 3.10: R<sup>2</sup> visualization plot of stress when strain = 0.02.

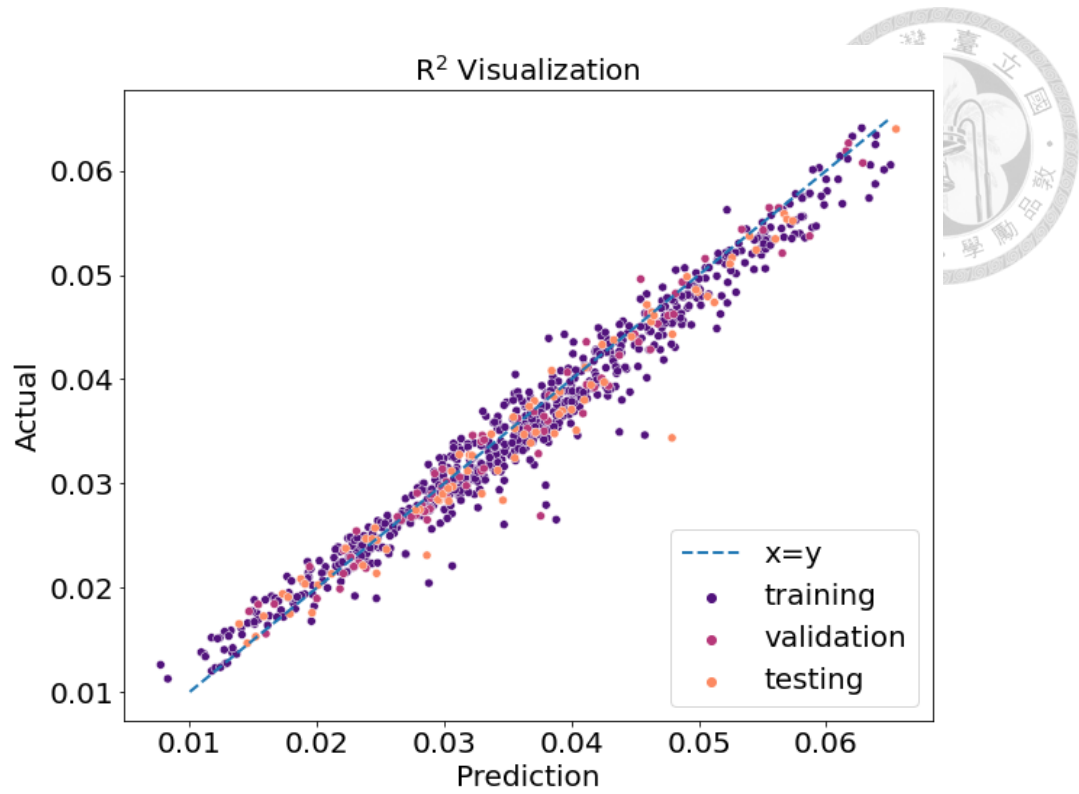


Fig 3.11: R<sup>2</sup> visualization plot of stress when strain = 0.03.

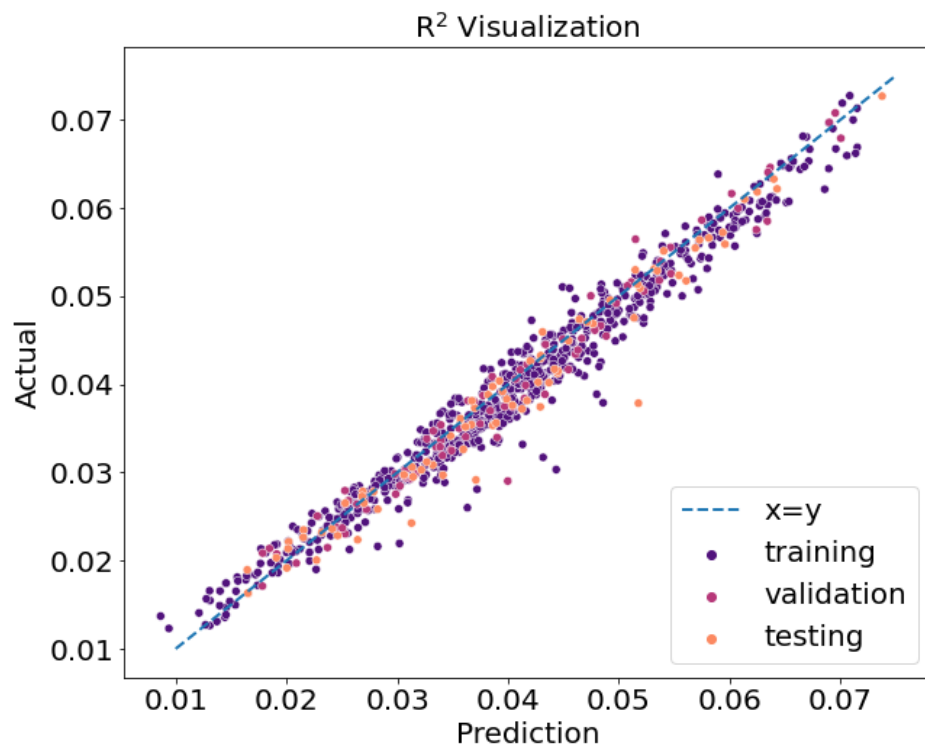


Fig 3.12: R<sup>2</sup> visualization plot of stress when strain = 0.04.

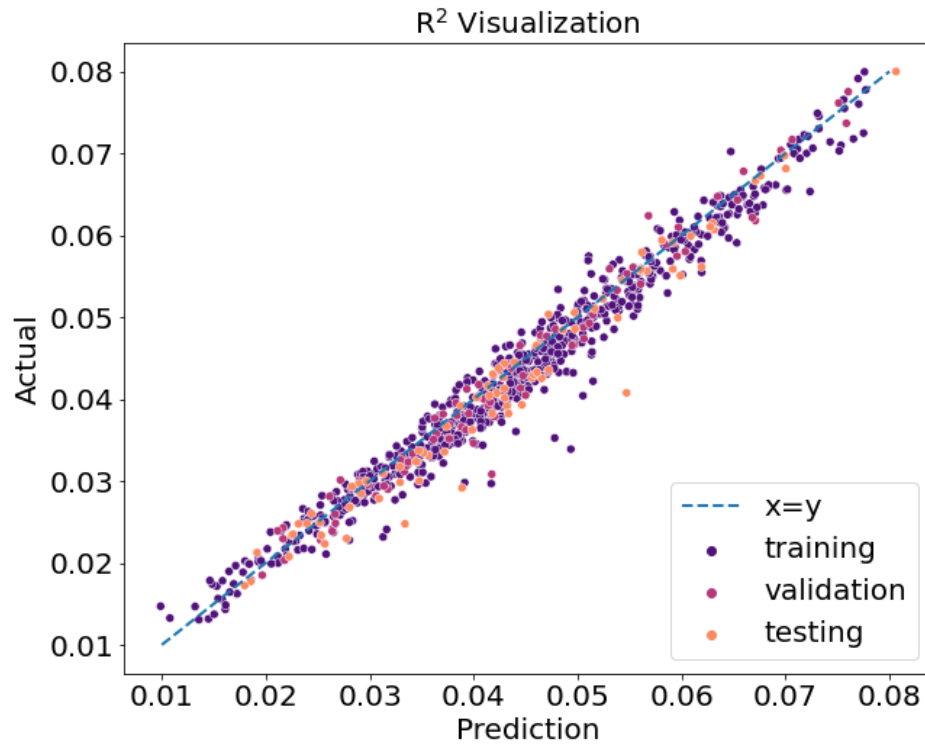


Fig 3.13: R<sup>2</sup> visualization plot of stress when strain = 0.05.

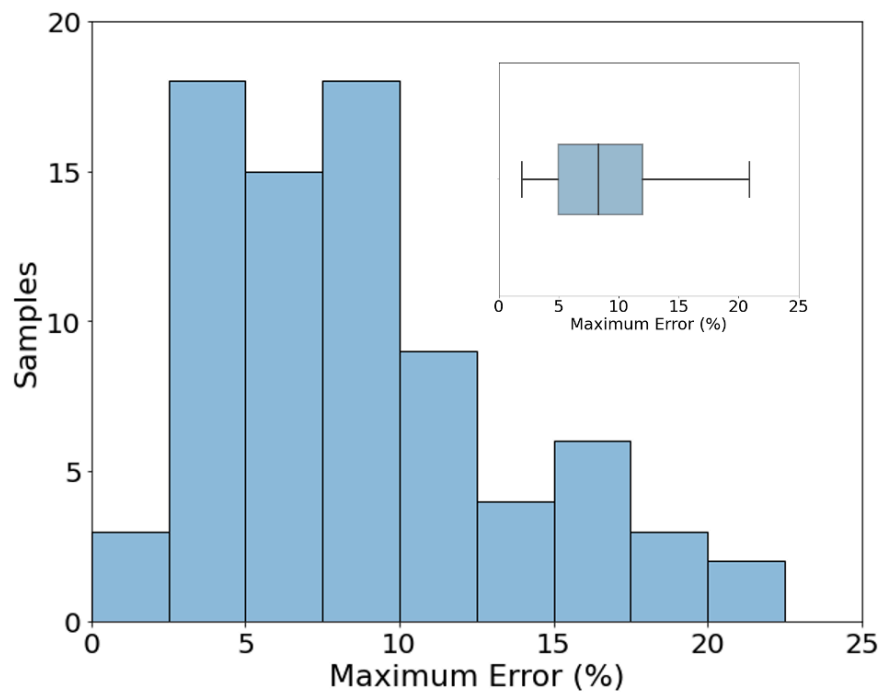


Fig 3.14: Comparison between predictive performances of ML with FEM for SFRCs. 82

testing data were used for comparison.



### 3.4 Summary

In this chapter, a DNN predictive model was trained to predict the stress-strain curves based on the SFRC dataset of 814 samples. Our model performs excellently in predicting stress-strain curves with  $R^2$  scores higher than 0.9 of material properties and maximum relative errors lower than 10% for most testing samples. Compared to the cost of experiments or computational methods, the ML predictive model can be a real-time and efficient tool for obtaining stress-strain curves and material properties. The ML method can be extended to analyses of other composites with nonlinear mechanical behavior. However, we may sometimes want to predict stress-strain curves of SFRCs with unseen aspect ratios. Hence, in the next chapter, TGML and two-phase learning approach will be adopted, and the results of applying them will be compared and discussed.



## Chapter 4 TGML and Two-phase Learning for Enhancing Stress-strain Curve Predictions of SFRCs

As demonstrated in the former chapter, machine learning techniques can help us predict stress-strain curves of SFRCs. However, the previous method may occur to some obstacles when we want to predict stress-strain curves of SFRCs with unseen aspect ratios in the dataset. Hence, in this chapter, we proposed TGML and two-phase learning methods to see if they have better predictive performances when predicting stress-strain curves of SFRCs with unprecedented aspect ratios. Fig 4.1 shows the workflow for using TGML and two-phase learning to predict the stress-strain behavior of the SFRCs. Like Chapter 3, the data preprocessing, training of ML models, and analyses of the results are done by Python codes.

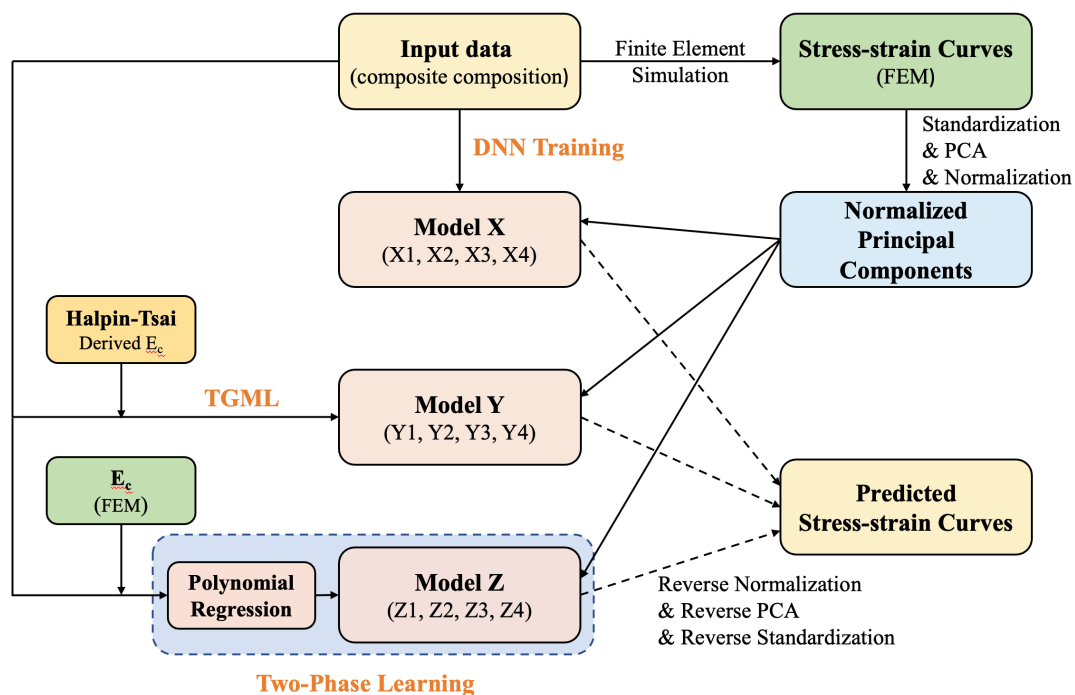
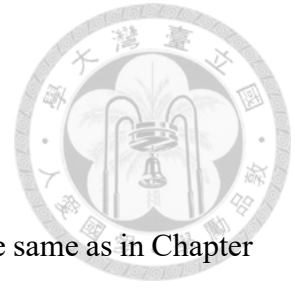


Fig 4.1: The overall workflow for predicting stress-strain curves of SFRCs.

## 4.1 Dataset Preparation

### 4.1.1 Dataset for Each Task

The entire dataset of SFRCs produced by FEM simulations is the same as in Chapter 3. However, each task is trained by a different portion of the dataset. The dataset for each task is depicted in Fig 4.2. For task A, the training data and validation data are the data of SFRCs that the aspect ratio equals 1, and the testing data are the data that the aspect ratio equals 10. As for task B, the training data and validation data are the data that the aspect ratio equals 1 or 4, and the testing data are the data that the aspect ratio equals 10. Moreover, for task C, the training data and validation data are the data that the aspect ratio equals 1, 4, or 7, and the testing data are the data that the aspect ratio equals 10. Lastly, for task D, the training data and validation data are the data that the aspect ratio equals 1, 4, or 7, and half of the data that the aspect ratio equals 10, and the testing data are the other half of the data that the aspect ratio equals 10. In all tasks, samples were split into training data and validation data with the percentage of 80% and 20%, respectively. Both training and validation sets were used in the training stage, while the testing set was not involved in training but only used to evaluate the model performance.



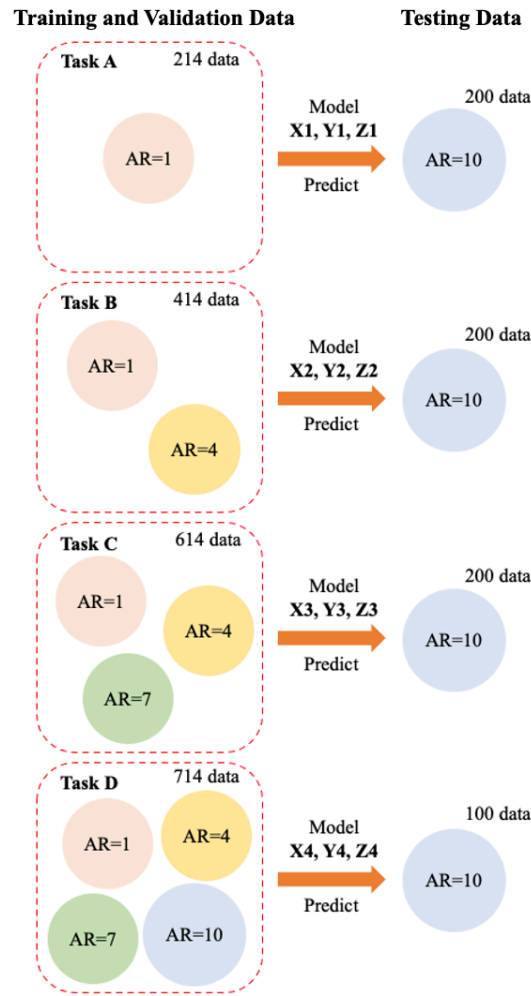


Fig 4.2: Illustration of the dataset of each model.

#### 4.1.2 Data Preparation for Model X

Input parameters of model X are in the range as listed in Table 2.1, and we normalize them to values between 0 and 1 before training. The procedure for preprocessing the output data is the same as in Chapter 3. Firstly, the stress-strain curves are represented as arrays of 101-dimensional stress values. Secondly, the stress vectors are standardized. Thirdly, the dimensionality of the stress vectors is reduced via PCA to 5-dimension vectors composed of the first 5 principal components. The cumulative explained variance of each model is higher than 99.95%. Eventually, we normalize the 5 most important principal components to values between 0 and 1 before training.

### 4.1.3 Data Preparation for Model Y

As mentioned in Chapter 2, TGML relies on data and the fundamental physical laws related to the problem (i.e., domain knowledge or theory). This chapter uses Halpin-Tsai equations to derive physics-based features (i.e., inputs). Halpin-Tsai equations are often used to predict Young's modulus of both unidirectional and randomly distributed fiber reinforcement composites [37], which is denoted as follows:

$$\frac{E_c}{E_0} = \frac{1 + \eta\xi\varphi_f}{1 - \eta\varphi_f} \quad (4-1)$$

$$\eta = \frac{E_1/E_0 - 1}{E_1/E_0 + \xi} \quad (4-2)$$

$$\xi = 2 \times AR \quad (4-3)$$

where  $E_c$  and  $E_0$  are Young's modulus values of the composite and the matrix, respectively. Also,  $\varphi_f$ ,  $E_1$ , and AR are the volume fraction, modulus, and aspect ratio of the fibers, respectively.

In this work, the predicted  $E_c/E_0$  was calculated via Halpin-Tsai equations with AR and  $E_1/E_0$ . The comparison between the predicted  $E_c/E_0$  and actual values from FEM is shown in Fig 4.3. Further, the derived  $E_c/E_0$  was substituted for AR as one of the six input parameters. Finally, before training, we normalized the input parameters to values between 0 and 1. On the other hand, the output data preprocessing procedures are the same as model X.

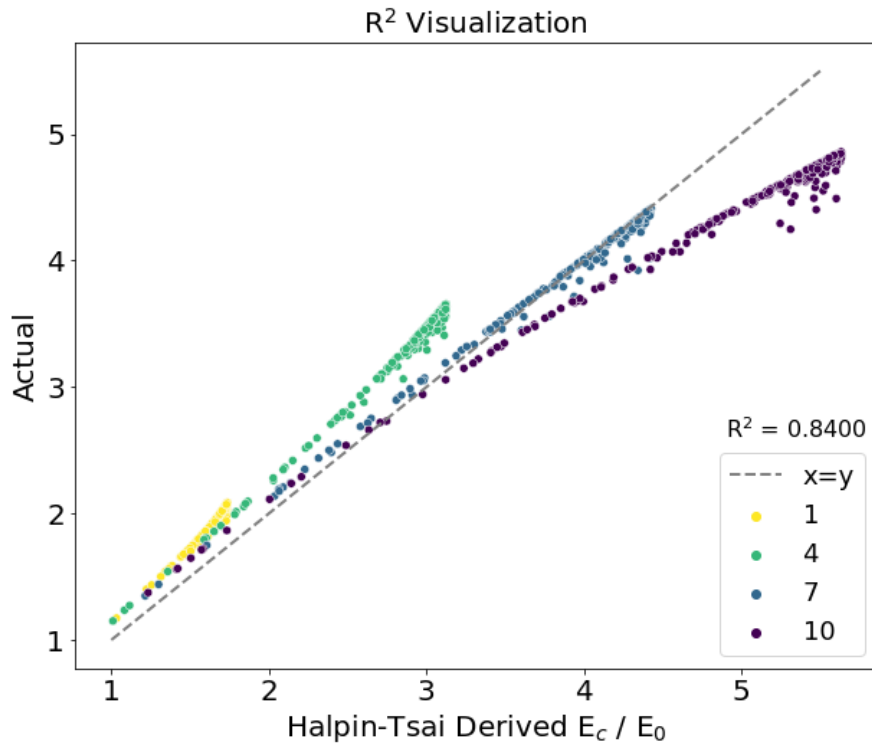


Fig 4.3: Comparison between Halpin-Tsai Derived  $E_c/E_0$  and actual values from FEM.

#### 4.1.4 Data Preparation for Model Z

As depicted in Fig 4.4, the whole model Z training is a two-phase learning process. In the first phase, AR and  $E_1/E_0$  were taken as the inputs, whereas Young's modulus values from FEM were taken as the outputs. First, the inputs were standardized. Subsequently, the 814 samples of the dataset were split as training and testing data in 80% and 20%, respectively. Further, the training set was fitted in a 5<sup>th</sup>-degree polynomial model, and the testing set was used to evaluate the model's predictive performance. As shown in Fig 4.5, the model can provide an excellent fit to the data with  $R^2$  scores of 0.9962 and 0.9969 for the training and testing data, respectively. Therefore, the results showed that we can obtain accurately predicted  $E_c/E_0$  from the polynomial model. In the second phase, AR was replaced with the predicted  $E_c/E_0$  from the first phase as one of the six input parameters. Eventually, we normalized the input parameters to values

between 0 and 1 before training. On the other hand, the output data preprocessing procedures are the same as model X and model Y.

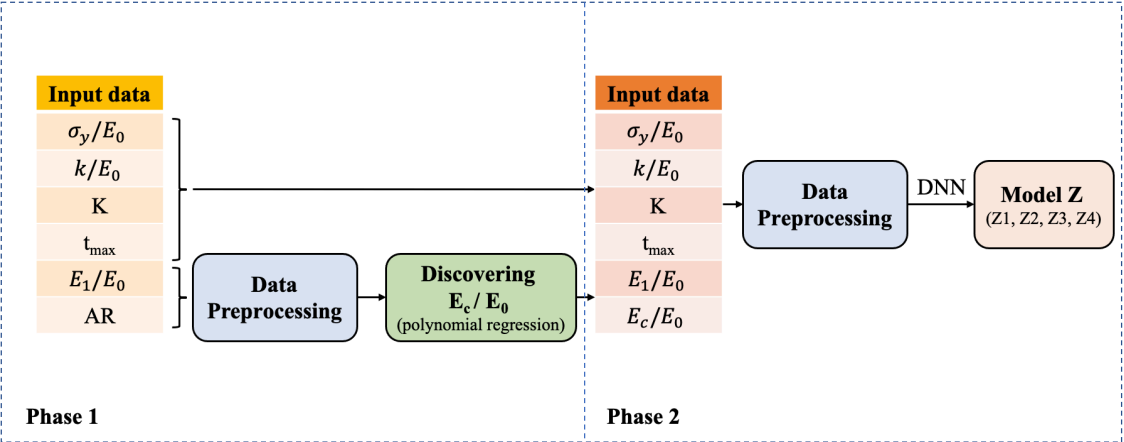


Fig 4.4: Illustration of two-phase learning.

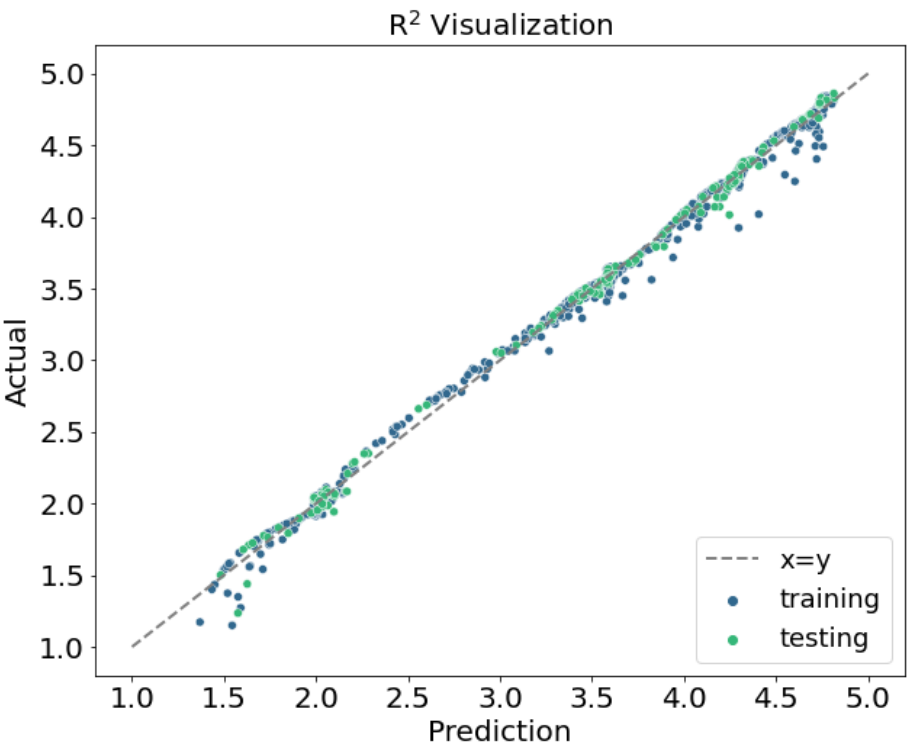


Fig 4.5: R<sup>2</sup> visualization of the 5th-degree polynomial model.

## 4.2 DNN Model Setup

The DNN architecture for each model in this chapter is the same as in Chapter 3. The weighted mean squared error is adopted to show our DNN models that the principal components have different importance. The Adam optimizer was chosen to train the DNN model. Also, we set the batch size to 8 in these models. Moreover, early stopping was adopted once the validation loss did not improve within 20 steps to avoid over-fitting.

After the training, we get the 101-dimensional stress-strain curves from the outputs (i.e., the 5-dimensional normalized principal components) via reverse normalization, reverse PCA, and reverse standardization.

## 4.3 Results and Discussion

For each predictive model, we selected the model that had a minimum loss on validation data as the final predictive model. The evaluation metrics of R2 score, MSE, and MAE corresponding to training, validation, and testing data of each model are demonstrated in Table 4.1 to Table 4.12. Moreover, the loss history during training, examples of predicted stress-strain curves by different models, regression scatter plots, and comparison between performances of the four tasks are plotted in Fig 4.6 to Fig 4.33. Due to the same value of aspect ratio in the training set and significant difference between the aspect ratio of the training set and that of the testing set, model X1 cannot learn good representations of aspect ratio. Therefore, as shown in Fig 4.7, the stress-strain curves of SFRCs predicted via model X1 are far from the actual results from the FEM simulation. However, the results obtained by model Y1 and Z1 have higher accuracy with a relatively low maximum error between prediction and ground truth (FEM) (see Fig 4.11). Furthermore, model Y2 and Z2 showed better predictive performance over model X2 in



task B. As for task C and task D, the variety of aspect ratios of the training set leads to better predictive performances than in previous tasks. In comparison with predictions of model X3, those of model Y3 and Z3 are closer to the actual stress-strain curves. Additionally, as shown in Fig 4.32, the maximum relative errors of model Y4 and Z4 are lower than those of model X4. The results of these four tasks clearly indicate that TGML and two-phase learning methods can have better predictive performances. Moreover, the results also show that predicted Young's modulus might serve as a more appropriate input feature than the aspect ratio, especially in tasks where the aspect ratio of the training set and testing set is in a different range.

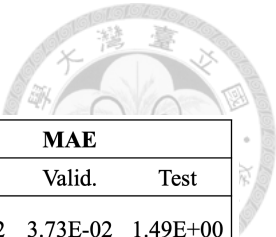
Table 4.1: Evaluation metrics of model X1.

Model X1	R <sup>2</sup> score			MSE			MAE		
	Train	Valid.	Test	Train	Valid.	Test	Train	Valid.	Test
Stiffness	0.5834	0.4261	-1415.061	6.96E-03	7.67E-03	1.29E+01	5.88E-02	6.19E-02	3.50E+00
Stress when strain = 0.01	0.8982	0.8676	-3.3454	1.32E-06	1.47E-06	2.07E-05	8.72E-04	9.61E-04	3.82E-03
Stress when strain = 0.03	0.9566	0.9553	-147.9670	3.15E-06	2.74E-06	1.61E-03	1.40E-03	1.23E-03	3.94E-02
Stress when strain = 0.05	0.9585	0.9552	-181.3772	3.44E-06	3.25E-06	1.58E-03	1.44E-03	1.34E-03	3.84E-02

Table 4.2: Evaluation metrics of model Y1.

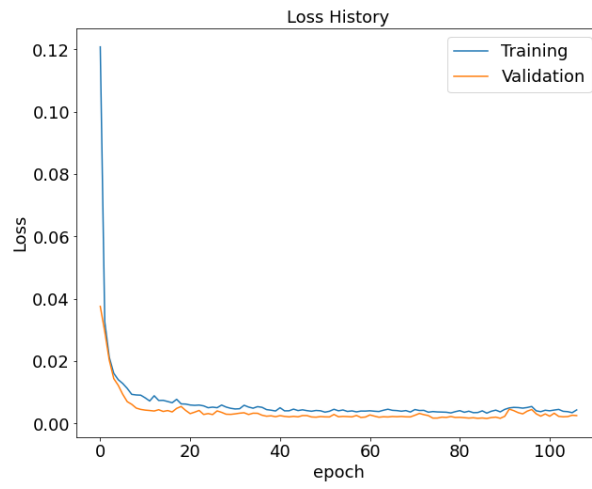
Model Y1	R <sup>2</sup> score			MSE			MAE		
	Train	Valid.	Test	Train	Valid.	Test	Train	Valid.	Test
Stiffness	0.9286	0.9155	-50.4827	1.63E-03	1.70E-03	2.50E+00	3.10E-02	3.39E-02	1.48E+00
Stress when strain = 0.01	0.9231	0.9334	-39.2247	6.59E-07	5.49E-07	1.64E-04	6.36E-04	5.79E-04	1.17E-02
Stress when strain = 0.03	0.9550	0.9584	-25.1368	2.47E-06	2.17E-06	3.84E-04	1.27E-03	1.21E-03	1.78E-02
Stress when strain = 0.05	0.9519	0.9535	-26.7054	3.16E-06	2.99E-06	4.84E-04	1.43E-03	1.35E-03	1.97E-02

Table 4.3: Evaluation metrics of model Z1.



Model Z1 Properties	R <sup>2</sup> score			MSE			MAE		
	Train	Valid.	Test	Train	Valid.	Test	Train	Valid.	Test
Stiffness	0.8817	0.8977	-39.5335	2.22E-03	2.26E-03	2.51E+00	3.36E-02	3.73E-02	1.49E+00
Stress when strain = 0.01	0.8882	0.8868	-7.2672	9.65E-07	9.69E-07	7.74E-05	8.06E-04	7.71E-04	7.28E-03
Stress when strain = 0.03	0.9420	0.9476	-1.3587	2.83E-06	2.59E-06	8.21E-05	1.39E-03	1.36E-03	7.58E-03
Stress when strain = 0.05	0.9574	0.9551	-1.8844	2.59E-06	2.76E-06	1.48E-04	1.32E-03	1.38E-03	1.02E-02

(a)



(b)



(c)

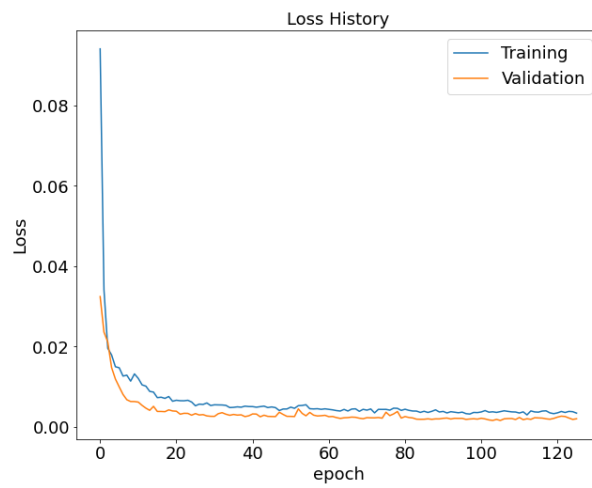


Fig 4.6: Loss history of task A. (a) Model X1. (b) Model Y1. (c) Model Z1.

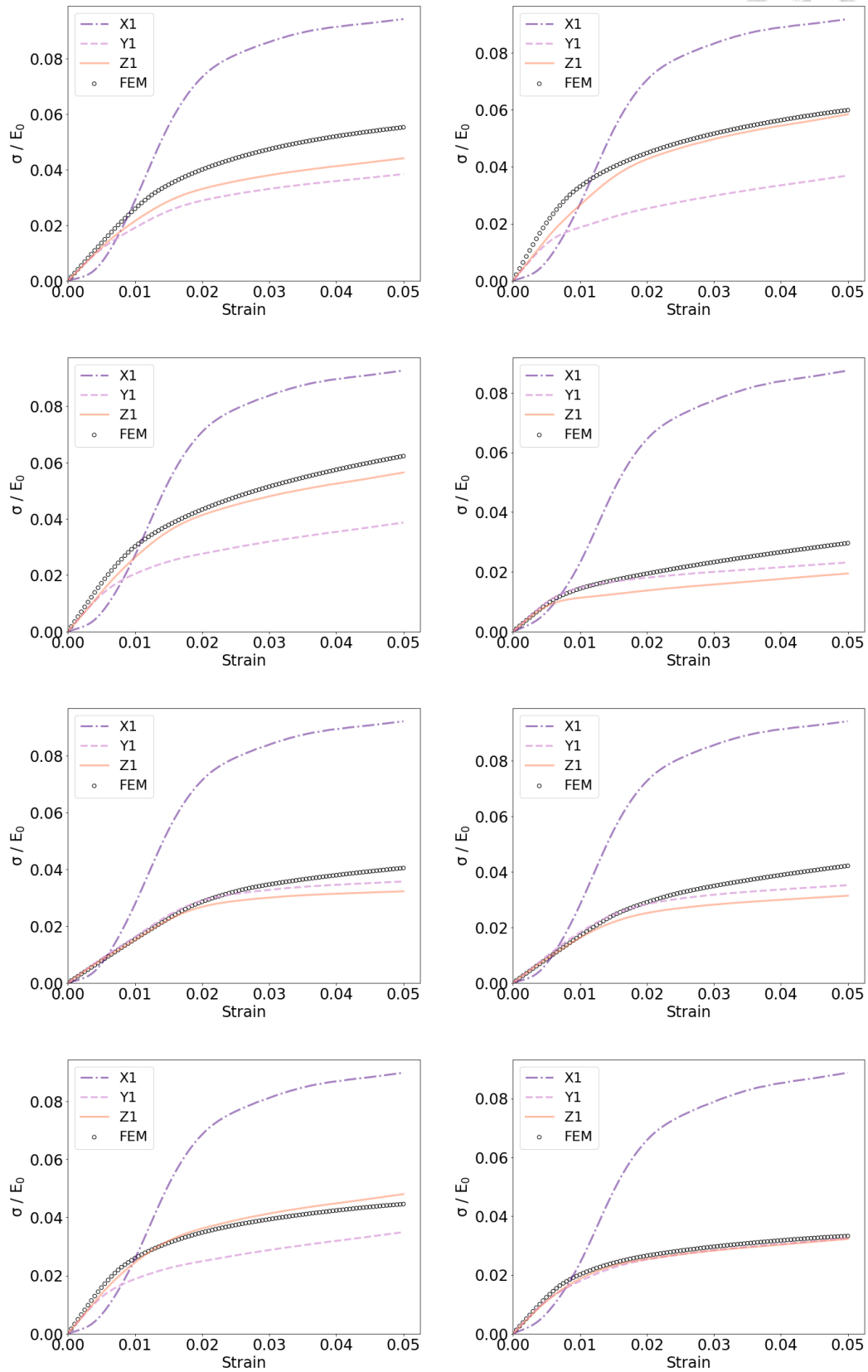


Fig 4.7: 8 comparisons between predicted stress-strain curves by model X1, Y1, and Z1 and the actual stress-strain curve (FEM).

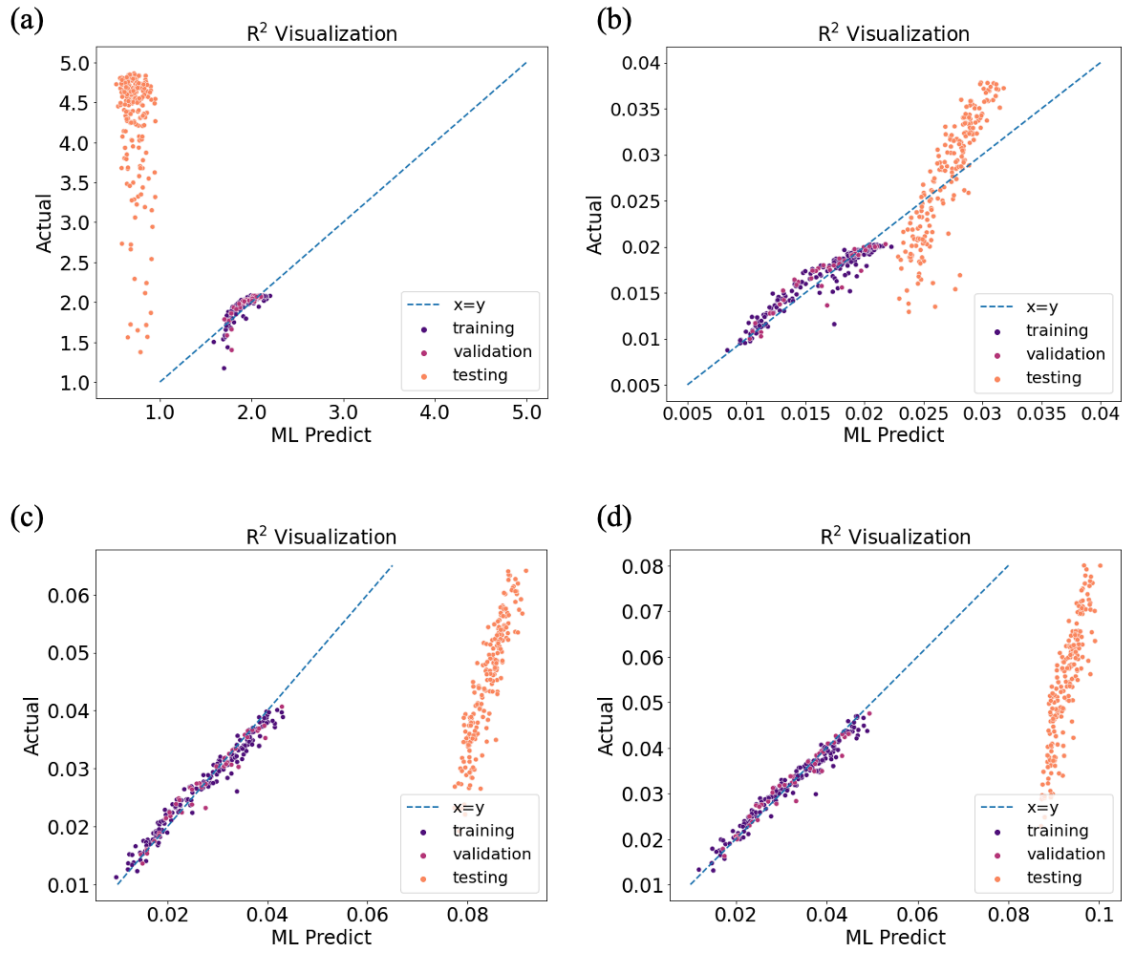


Fig 4.8:  $R^2$  visualization plot of model X1. (a) Stiffness. (b) Stress when strain = 0.01.  
(c) Stress when strain = 0.03. (d) Stress when strain = 0.05.

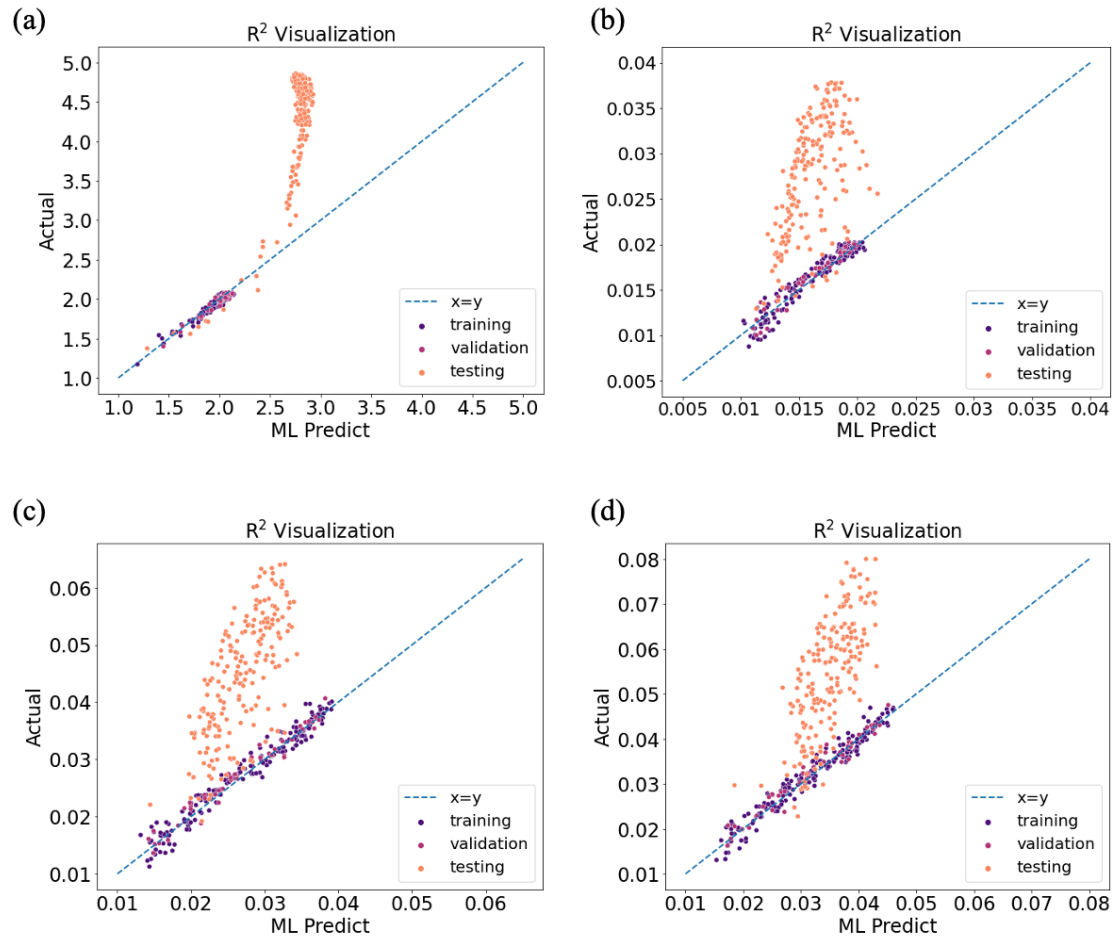


Fig 4.9:  $R^2$  visualization plot of model Y1. (a) Stiffness. (b) Stress when strain = 0.01. (c) Stress when strain = 0.03. (d) Stress when strain = 0.05.

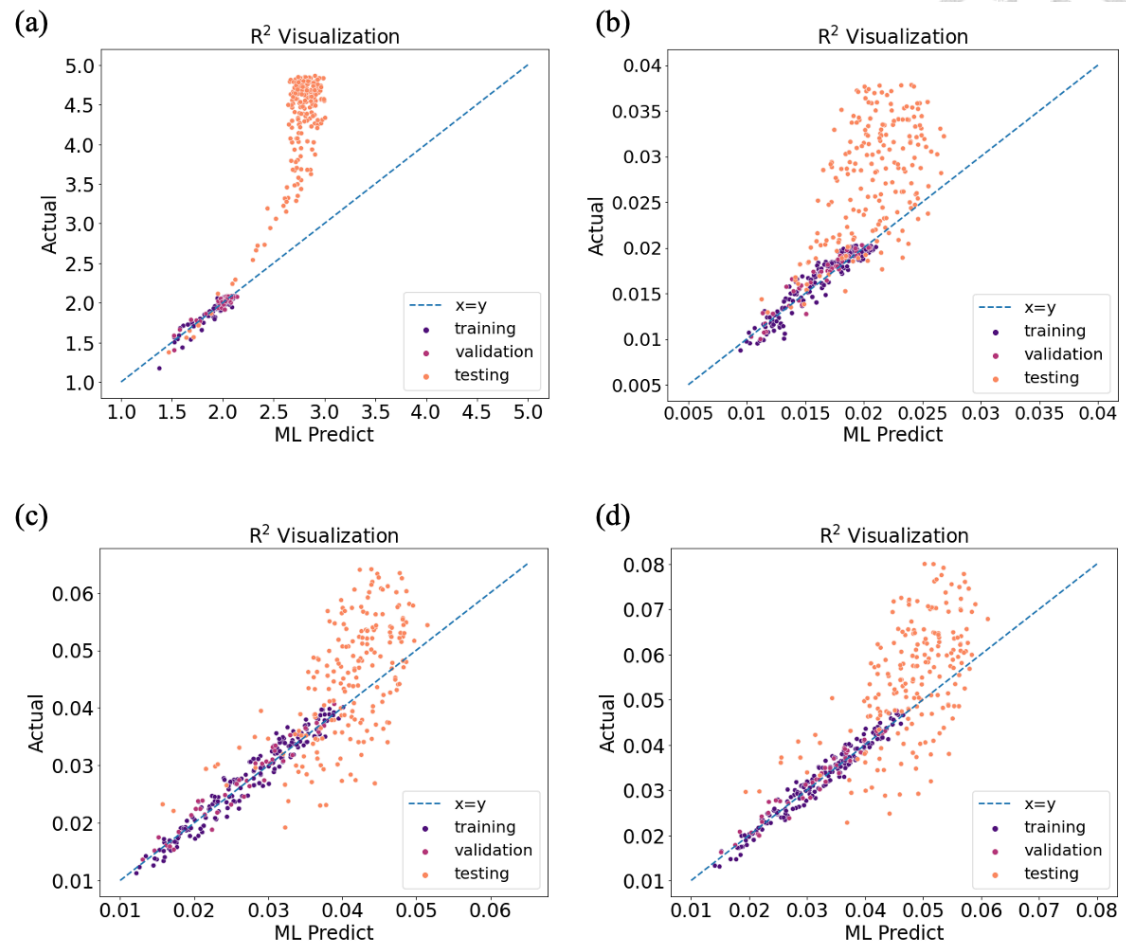


Fig 4.10:  $R^2$  visualization plot of model Z1. (a) Stiffness. (b) Stress when strain = 0.01.  
(c) Stress when strain = 0.03. (d) Stress when strain = 0.05.

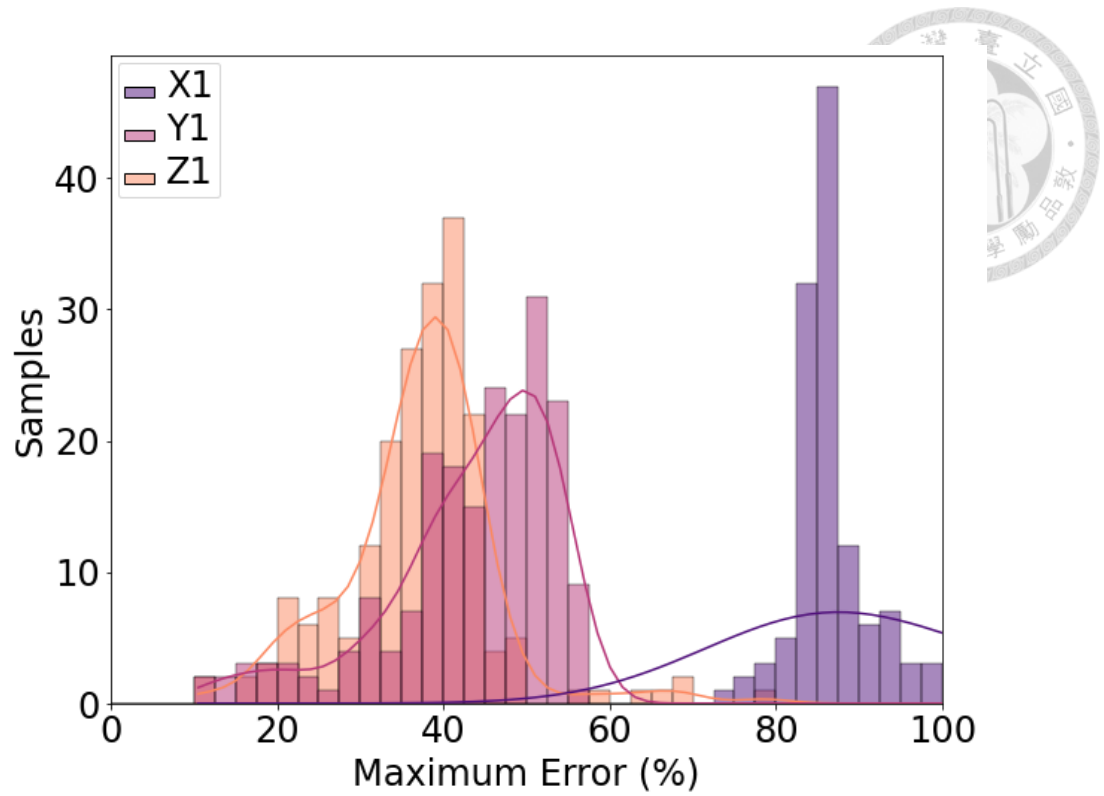


Fig 4.11: Comparison between performances of model X1, Y1, and Z1 in task A.

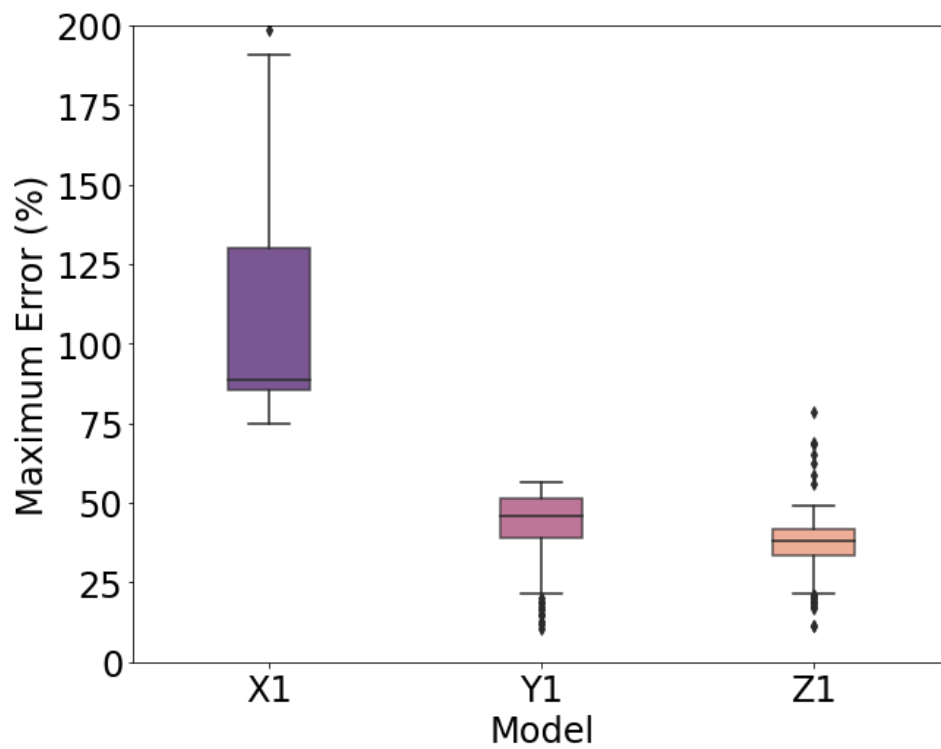
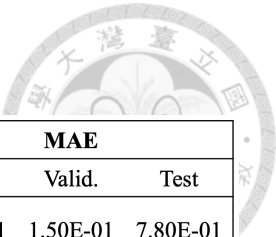


Fig 4.12: Boxplot of maximum error of model X1, Y1, and Z1 in task A.



Table 4.4: Evaluation metrics of model X2.



Model X2	R <sup>2</sup> score			MSE			MAE		
	Train	Valid.	Test	Train	Valid.	Test	Train	Valid.	Test
Stiffness	0.9211	0.8953	-8.2989	4.53E-02	6.18E-02	6.88E-01	1.44E-01	1.50E-01	7.80E-01
Stress when strain = 0.01	0.9126	0.8921	-2.6543	1.99E-06	2.84E-06	5.19E-05	1.06E-03	1.09E-03	6.52E-03
Stress when strain = 0.03	0.9578	0.9492	-4.4297	3.01E-06	3.87E-06	2.09E-04	1.30E-03	1.48E-03	1.35E-02
Stress when strain = 0.05	0.9526	0.9362	-5.5279	4.58E-06	6.20E-06	3.44E-04	1.64E-03	1.93E-03	1.72E-02

Table 4.5: Evaluation metrics of model Y2.

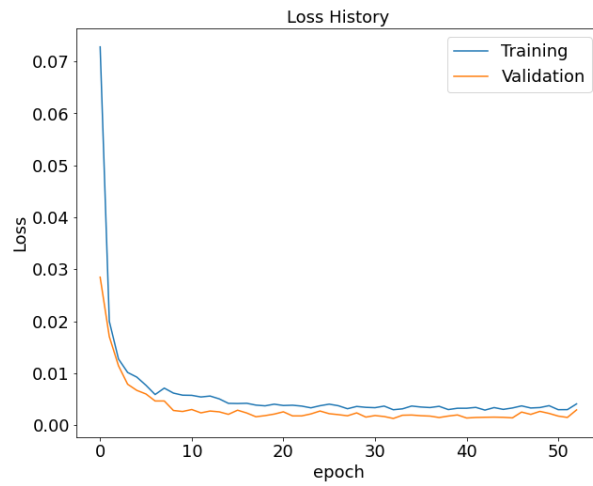
Model Y2	R <sup>2</sup> score			MSE			MAE		
	Train	Valid.	Test	Train	Valid.	Test	Train	Valid.	Test
Stiffness	0.9699	0.9671	0.1338	1.88E-02	1.92E-02	2.58E-01	1.12E-01	1.15E-01	4.53E-01
Stress when strain = 0.01	0.9603	0.9593	-1.4491	9.25E-07	1.01E-06	3.41E-05	7.73E-04	7.46E-04	5.05E-03
Stress when strain = 0.03	0.9739	0.9709	-1.2423	2.06E-06	2.27E-06	1.04E-04	1.13E-03	1.18E-03	9.30E-03
Stress when strain = 0.05	0.9629	0.9597	-1.6519	3.99E-06	4.05E-06	1.76E-04	1.60E-03	1.58E-03	1.22E-02

Table 4.6: Evaluation metrics of model Z2.

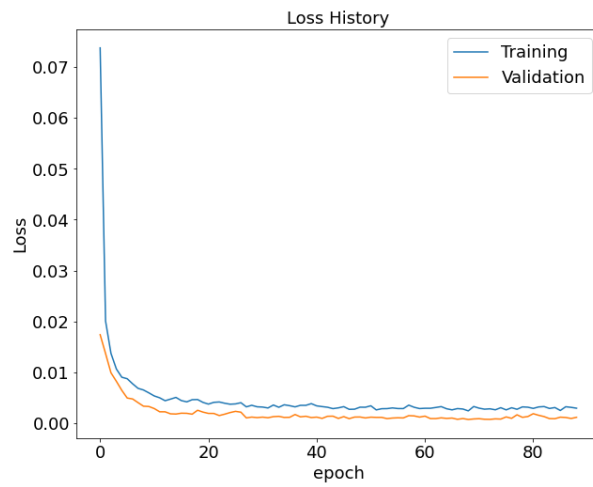
Model Z2	R <sup>2</sup> score			MSE			MAE		
	Train	Valid.	Test	Train	Valid.	Test	Train	Valid.	Test
Stiffness	0.9771	0.9725	0.6747	1.52E-02	1.78E-02	1.27E-01	1.03E-01	1.04E-01	3.27E-01
Stress when strain = 0.01	0.9575	0.9640	0.3204	1.24E-06	1.16E-06	1.87E-05	8.72E-04	8.67E-04	4.08E-03
Stress when strain = 0.03	0.9757	0.9753	-0.3044	2.13E-06	2.23E-06	9.47E-05	1.16E-03	1.22E-03	9.44E-03
Stress when strain = 0.05	0.9784	0.9739	-0.6202	2.46E-06	2.87E-06	1.65E-04	1.25E-03	1.36E-03	1.25E-02



(a)



(b)



(c)

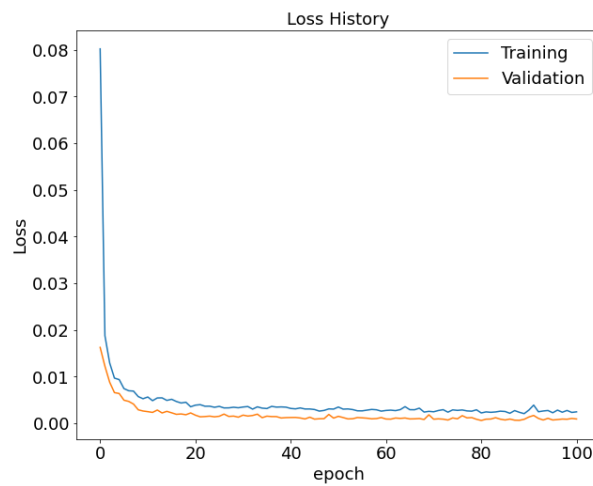


Fig 4.13: Loss history of task B. (a) Model X2. (b) Model Y2. (c) Model Z2.

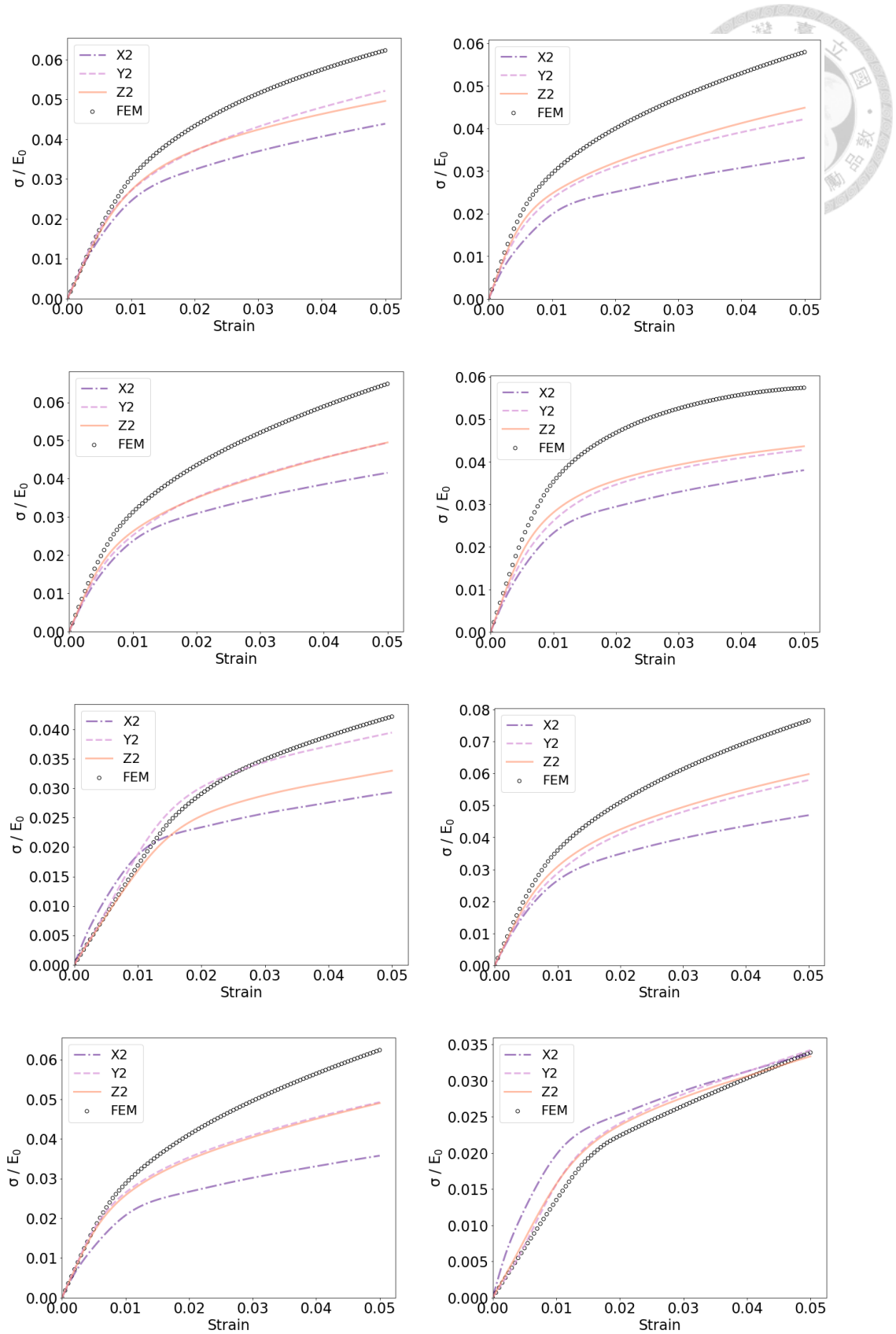


Fig 4.14: 8 comparisons between predicted stress-strain curves by model X2, Y2, and Z2 and the actual stress-strain curve (FEM).

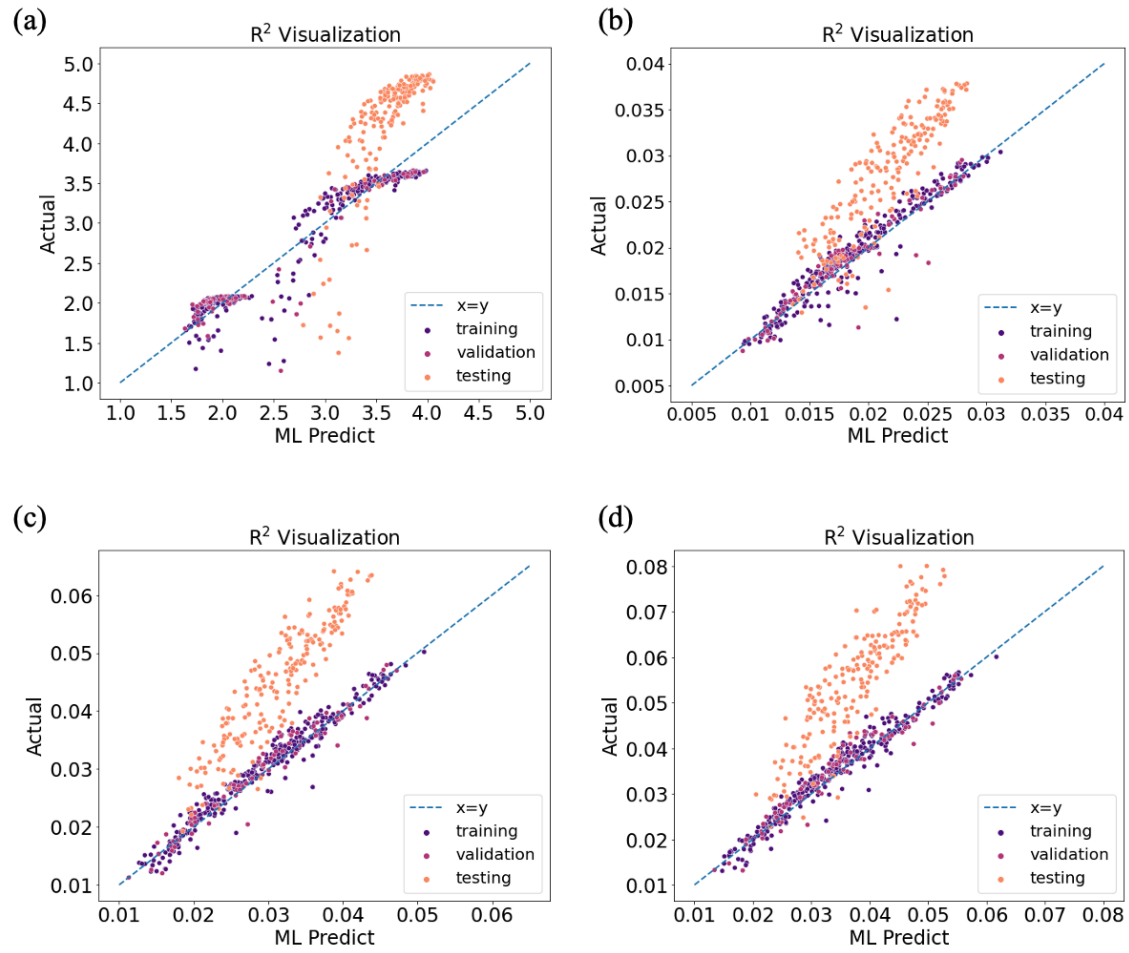


Fig 4.15:  $R^2$  visualization plot of model X2. (a) Stiffness. (b) Stress when strain = 0.01.

(c) Stress when strain = 0.03. (d) Stress when strain = 0.05.

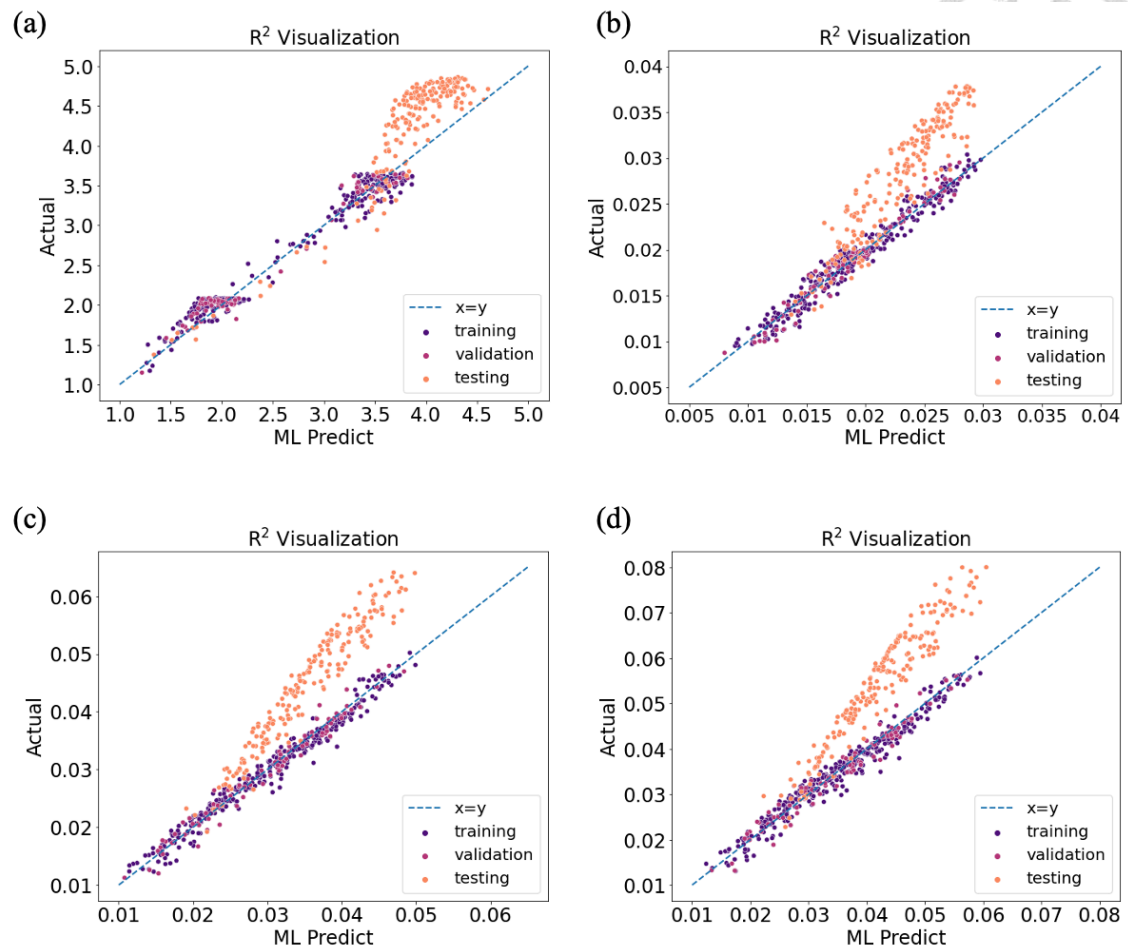


Fig 4.16:  $R^2$  visualization plot of model Y2. (a) Stiffness. (b) Stress when strain = 0.01. (c) Stress when strain = 0.03. (d) Stress when strain = 0.05.

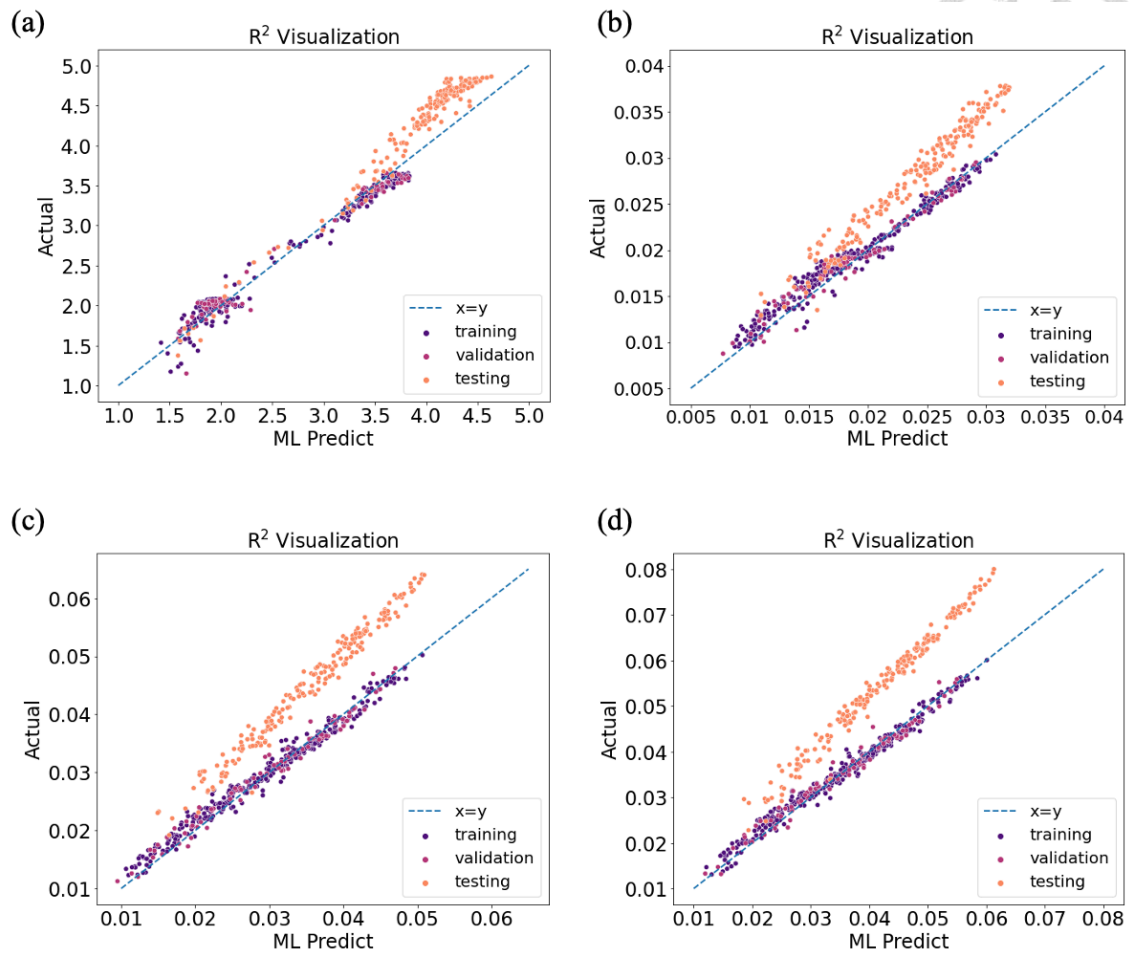


Fig 4.17:  $R^2$  visualization plot of model Z2. (a) Stiffness. (b) Stress when strain = 0.01.

(c) Stress when strain = 0.03. (d) Stress when strain = 0.05.

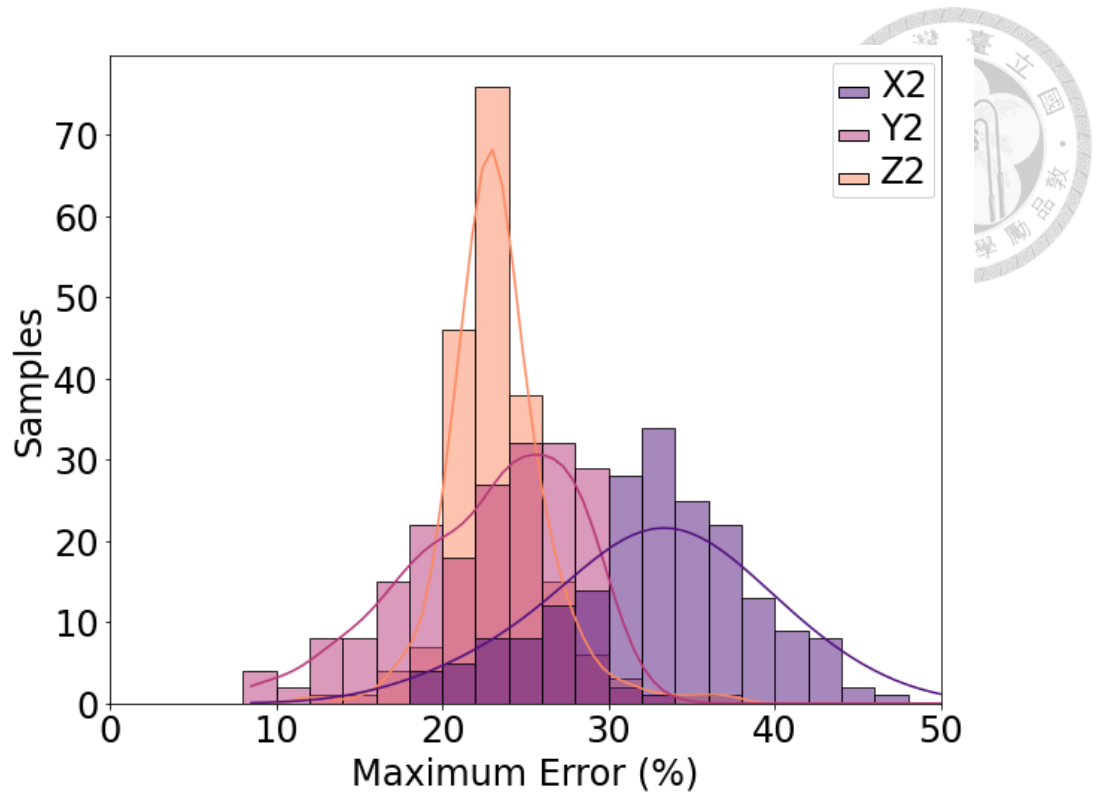


Fig 4.18: Comparison between performances of model X2, Y2, and Z2 in task B.

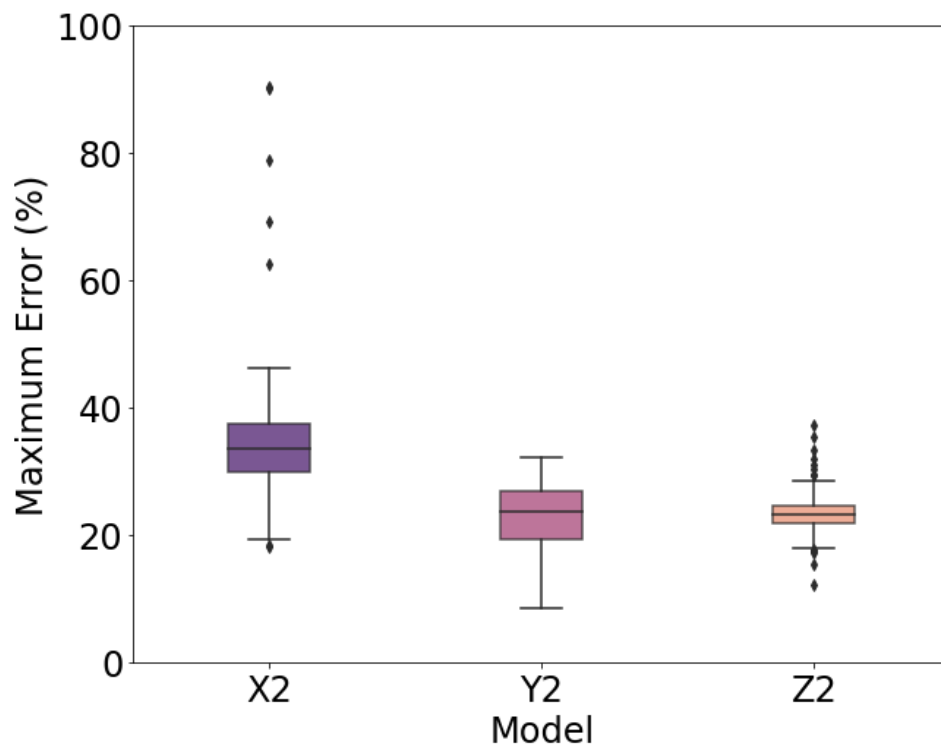
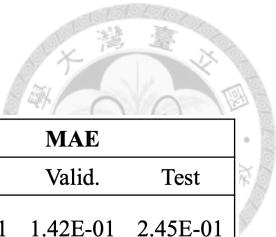


Fig 4.19: Boxplot of maximum error of model X2, Y2, and Z2 in task B.

Table 4.7: Evaluation metrics of model X3.



Model X3	R <sup>2</sup> score			MSE			MAE		
	Train	Valid.	Test	Train	Valid.	Test	Train	Valid.	Test
Stiffness	0.9638	0.9549	0.7751	3.30E-02	4.01E-02	1.14E-01	1.25E-01	1.42E-01	2.45E-01
Stress when strain = 0.01	0.9561	0.9523	0.8634	1.27E-06	1.47E-06	3.99E-06	6.70E-04	7.69E-04	1.41E-03
Stress when strain = 0.03	0.9723	0.9735	0.8888	2.26E-06	2.10E-06	9.36E-06	1.08E-03	1.08E-03	2.53E-03
Stress when strain = 0.05	0.9732	0.9777	0.9212	3.16E-06	2.53E-06	9.94E-06	1.26E-03	1.21E-03	2.31E-03

Table 4.8: Evaluation metrics of model Y3.

Model Y3	R <sup>2</sup> score			MSE			MAE		
	Train	Valid.	Test	Train	Valid.	Test	Train	Valid.	Test
Stiffness	0.9721	0.9725	0.9302	2.09E-02	2.03E-02	2.79E-02	1.14E-01	1.16E-01	1.41E-01
Stress when strain = 0.01	0.9596	0.9611	0.9096	1.20E-06	1.19E-06	2.92E-06	8.28E-04	8.32E-04	1.28E-03
Stress when strain = 0.03	0.9621	0.9650	0.9067	3.40E-06	3.04E-06	9.36E-06	1.49E-03	1.36E-03	2.48E-03
Stress when strain = 0.05	0.9638	0.9623	0.9029	4.86E-06	4.78E-06	1.52E-05	1.80E-03	1.75E-03	3.07E-03

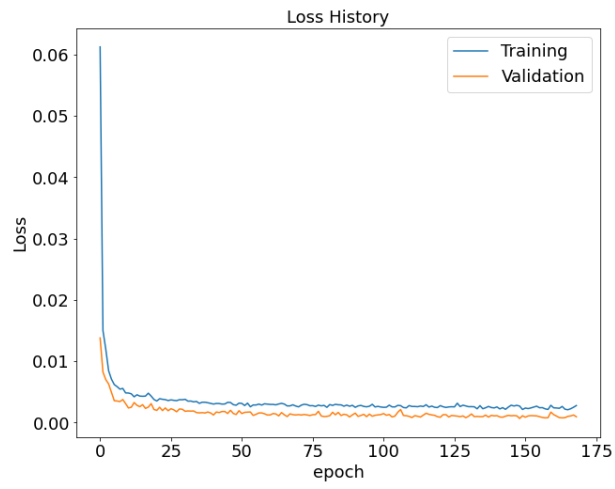
Table 4.9: Evaluation metrics of model Z3.

Model Z3	R <sup>2</sup> score			MSE			MAE		
	Train	Valid.	Test	Train	Valid.	Test	Train	Valid.	Test
Stiffness	0.9696	0.9714	0.8390	2.22E-02	2.08E-02	6.60E-02	1.17E-01	1.12E-01	2.23E-01
Stress when strain = 0.01	0.9584	0.9645	0.9617	1.61E-06	1.34E-06	1.47E-06	1.01E-03	8.63E-04	9.48E-04
Stress when strain = 0.03	0.9526	0.9591	0.9476	5.64E-06	4.56E-06	6.03E-06	1.90E-03	1.69E-03	1.80E-03
Stress when strain = 0.05	0.9473	0.9502	0.9246	9.07E-06	7.93E-06	1.29E-05	2.37E-03	2.25E-03	2.60E-03

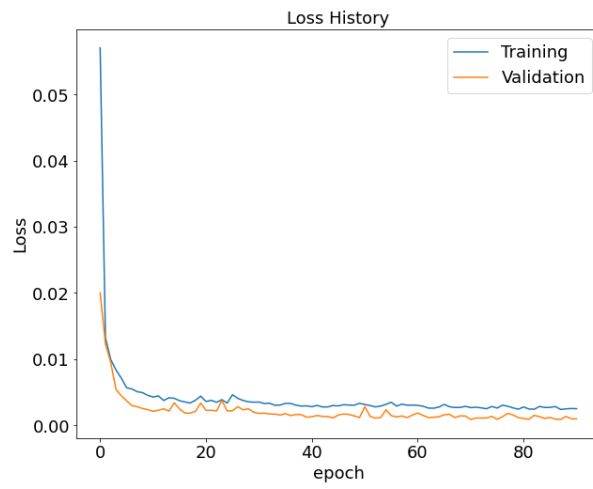




(a)



(b)



(c)

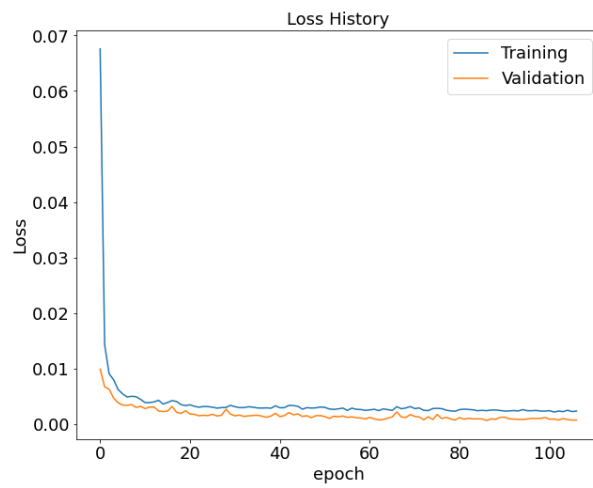


Fig 4.20: Loss history of task C. (a) Model X3. (b) Model Y3. (c) Model Z3.

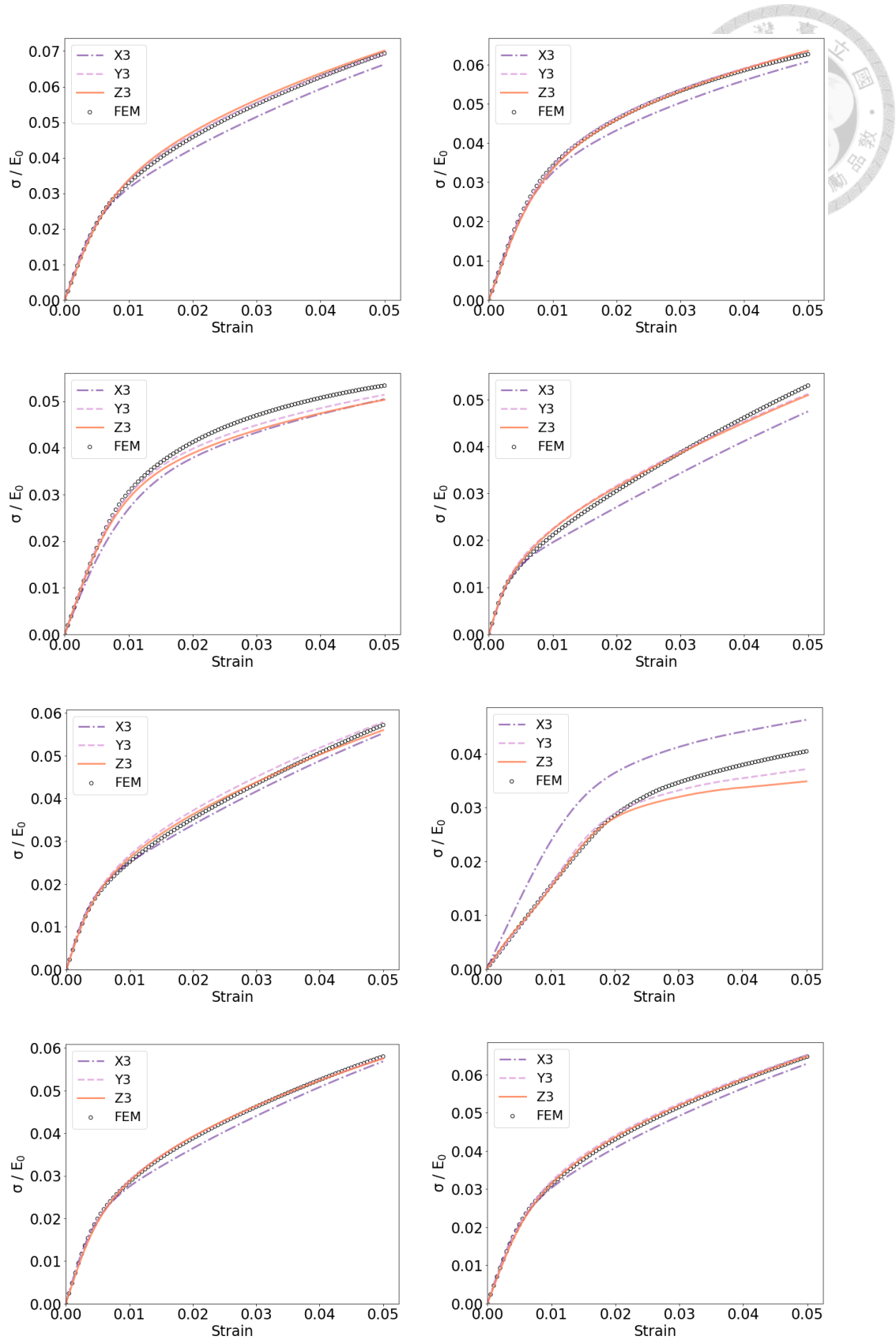


Fig 4.21: 8 comparisons between predicted stress-strain curves by model X3, Y3, and Z3 and the actual stress-strain curve (FEM).

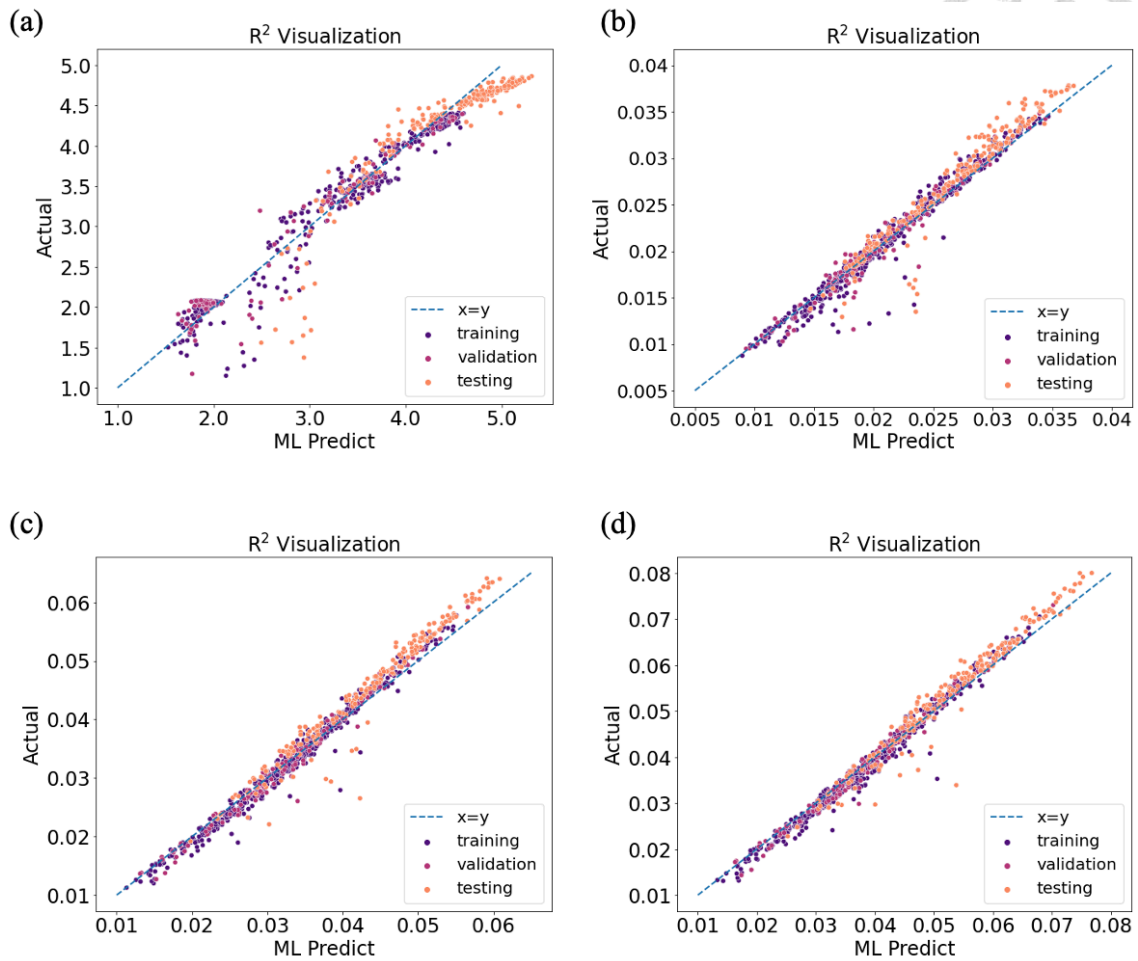


Fig 4.22:  $R^2$  visualization plot of model X3. (a) Stiffness. (b) Stress when strain = 0.01.

(c) Stress when strain = 0.03. (d) Stress when strain = 0.05.

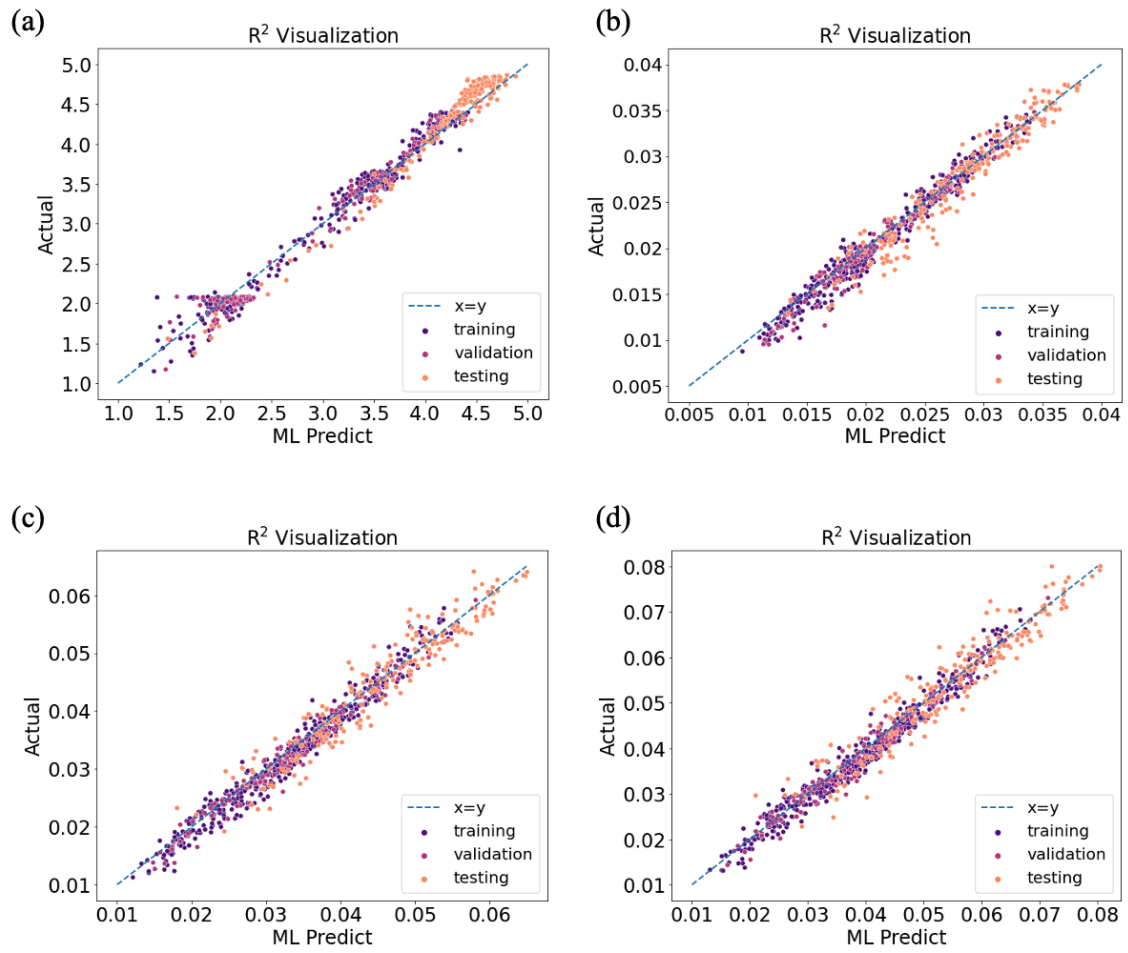


Fig 4.23:  $R^2$  visualization plot of model Y3. (a) Stiffness. (b) Stress when strain = 0.01.

(c) Stress when strain = 0.03. (d) Stress when strain = 0.05.

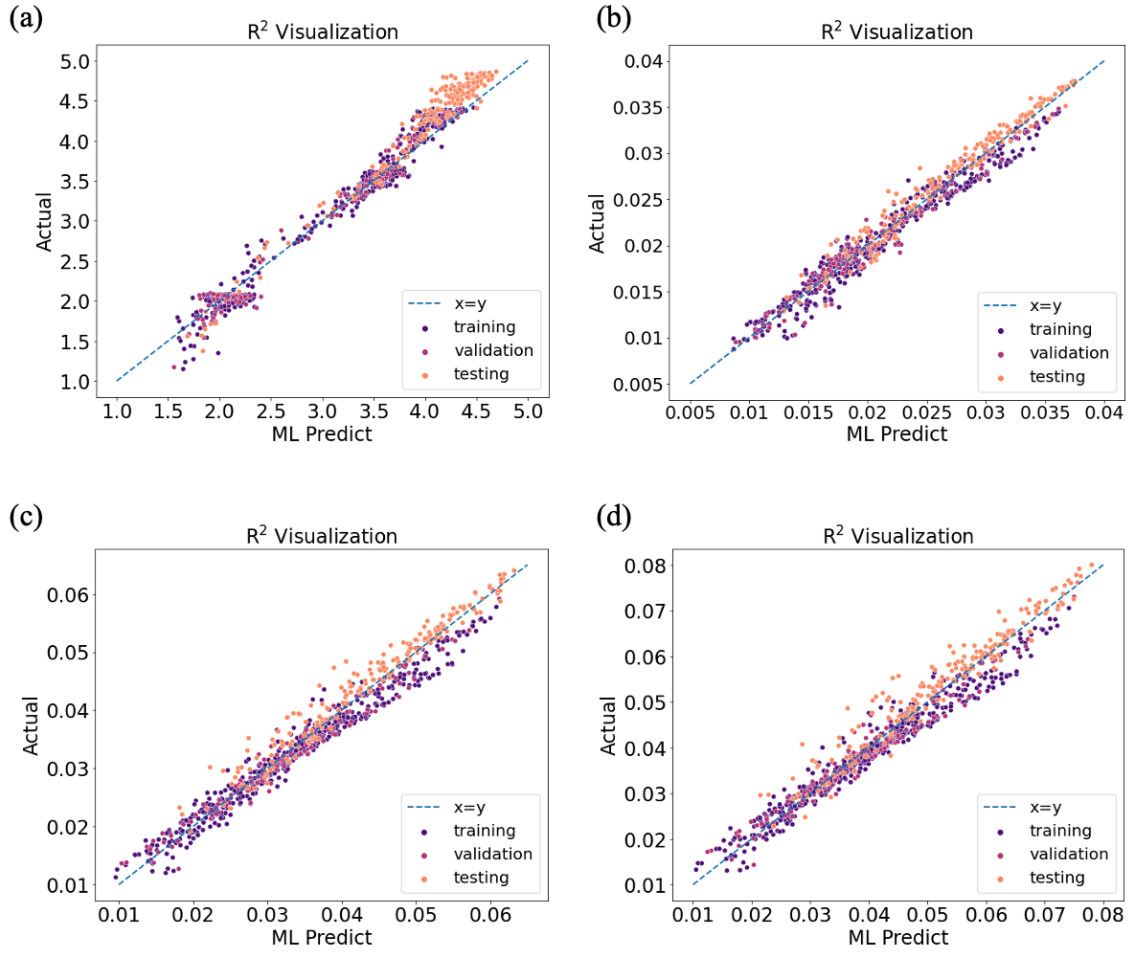


Fig 4.24:  $R^2$  visualization plot of model Z3. (a) Stiffness. (b) Stress when strain = 0.01. (c) Stress when strain = 0.03. (d) Stress when strain = 0.05.

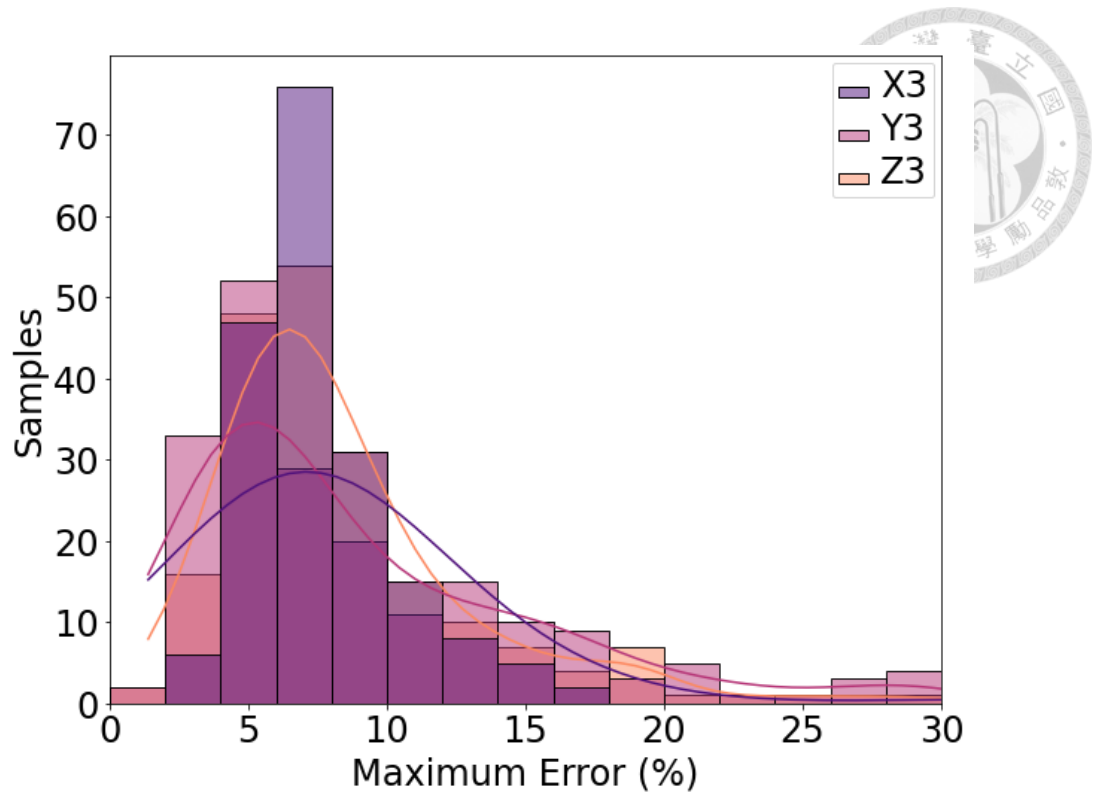


Fig 4.25: Comparison between performances of model X3, Y3, and Z3 in task C.

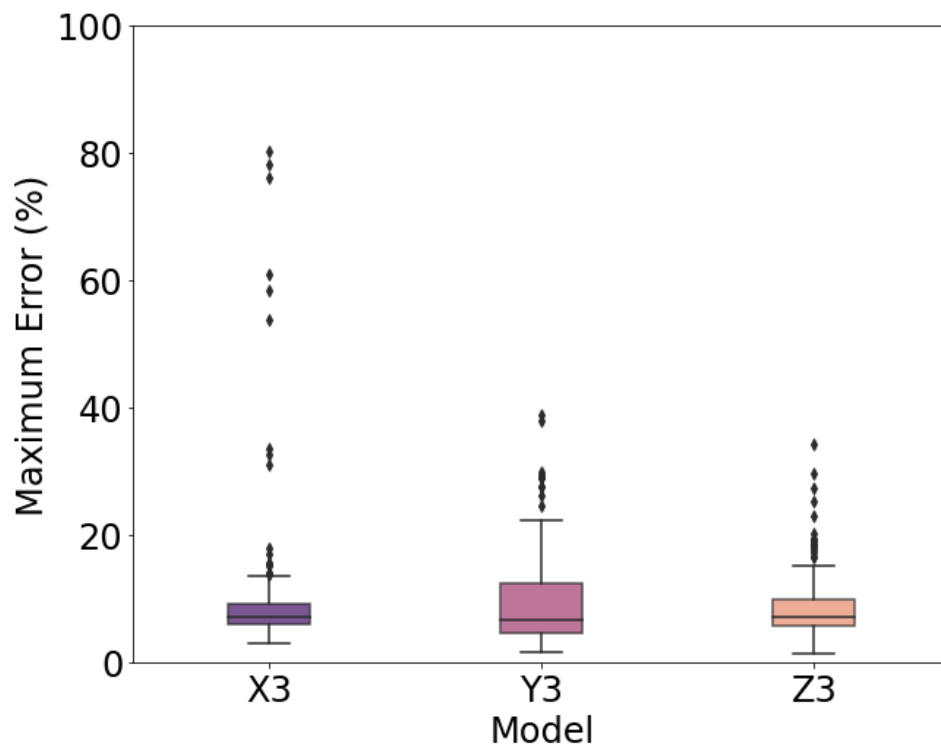
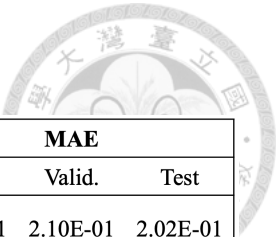


Fig 4.26: Boxplot of maximum error of model X3, Y3, and Z3 in task C.

Table 4.10: Evaluation metrics of model X4.



Model X4	R <sup>2</sup> score			MSE			MAE		
	Train	Valid.	Test	Train	Valid.	Test	Train	Valid.	Test
Stiffness	0.9312	0.9210	0.7170	7.64E-02	8.38E-02	9.41E-02	1.91E-01	2.10E-01	2.02E-01
Stress when strain = 0.01	0.9229	0.9145	0.8754	3.33E-06	3.52E-06	3.71E-06	1.29E-03	1.26E-03	1.38E-03
Stress when strain = 0.03	0.9562	0.9628	0.9114	5.48E-06	4.63E-06	7.72E-06	1.66E-03	1.57E-03	2.01E-03
Stress when strain = 0.05	0.9583	0.9695	0.9182	7.59E-06	5.56E-06	1.06E-05	1.91E-03	1.77E-03	2.35E-03

Table 4.11: Evaluation metrics of model Y4.

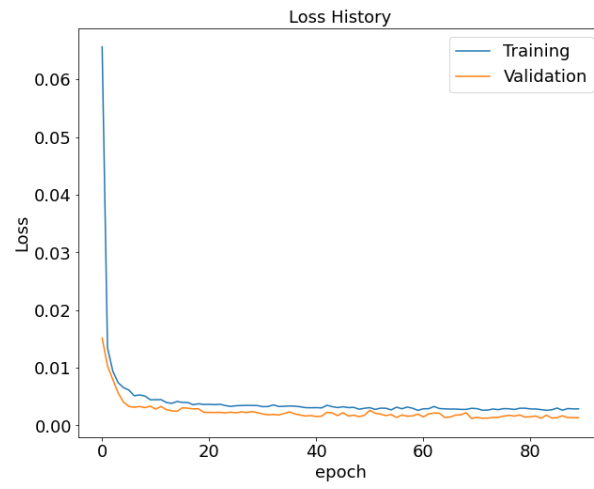
Model Y4	R <sup>2</sup> score			MSE			MAE		
	Train	Valid.	Test	Train	Valid.	Test	Train	Valid.	Test
Stiffness	0.9715	0.9734	0.8366	2.46E-02	2.32E-02	5.98E-02	1.26E-01	1.23E-01	2.05E-01
Stress when strain = 0.01	0.9699	0.9634	0.9567	9.39E-07	1.11E-06	1.43E-06	7.70E-04	8.35E-04	9.92E-04
Stress when strain = 0.03	0.9601	0.9518	0.9615	3.57E-06	4.20E-06	3.80E-06	1.47E-03	1.62E-03	1.56E-03
Stress when strain = 0.05	0.9570	0.9478	0.9544	5.79E-06	7.00E-06	6.91E-06	1.87E-03	2.12E-03	1.93E-03

Table 4.12: Evaluation metrics of model Z4.

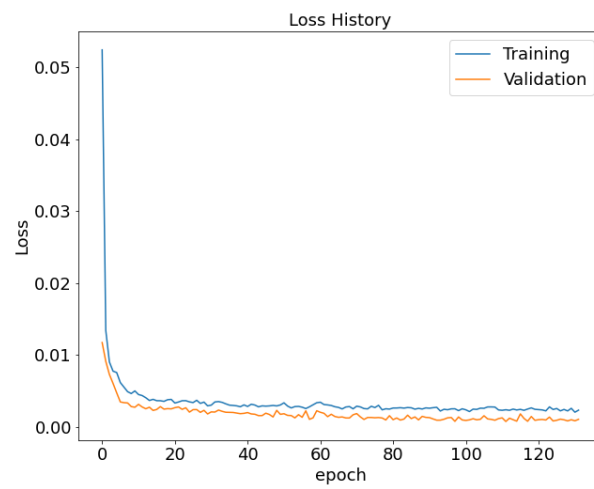
Model Z4	R <sup>2</sup> score			MSE			MAE		
	Train	Valid.	Test	Train	Valid.	Test	Train	Valid.	Test
Stiffness	0.9895	0.9878	0.9730	1.08E-02	1.23E-02	1.25E-02	8.15E-02	9.04E-02	8.38E-02
Stress when strain = 0.01	0.9798	0.9759	0.9765	8.29E-07	9.24E-07	9.47E-07	6.86E-04	7.20E-04	7.39E-04
Stress when strain = 0.03	0.9741	0.9737	0.9492	2.78E-06	2.69E-06	5.49E-06	1.29E-03	1.23E-03	1.63E-03
Stress when strain = 0.05	0.9660	0.9662	0.9224	5.22E-06	5.05E-06	1.20E-05	1.75E-03	1.66E-03	2.27E-03



(a)



(b)



(c)

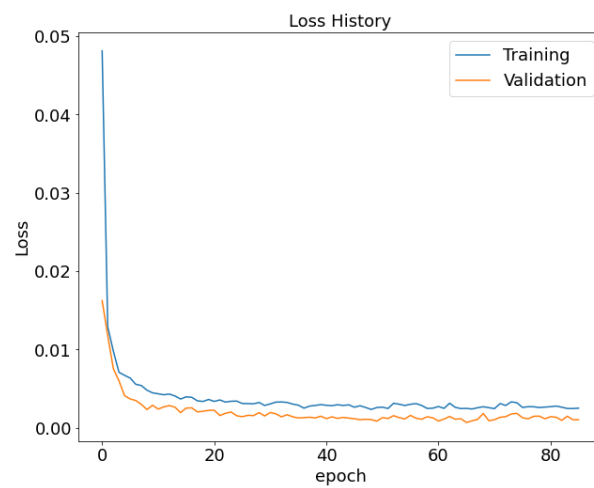


Fig 4.27: Loss history of task D. (a) Model X4. (b) Model Y4. (c) Model Z4.



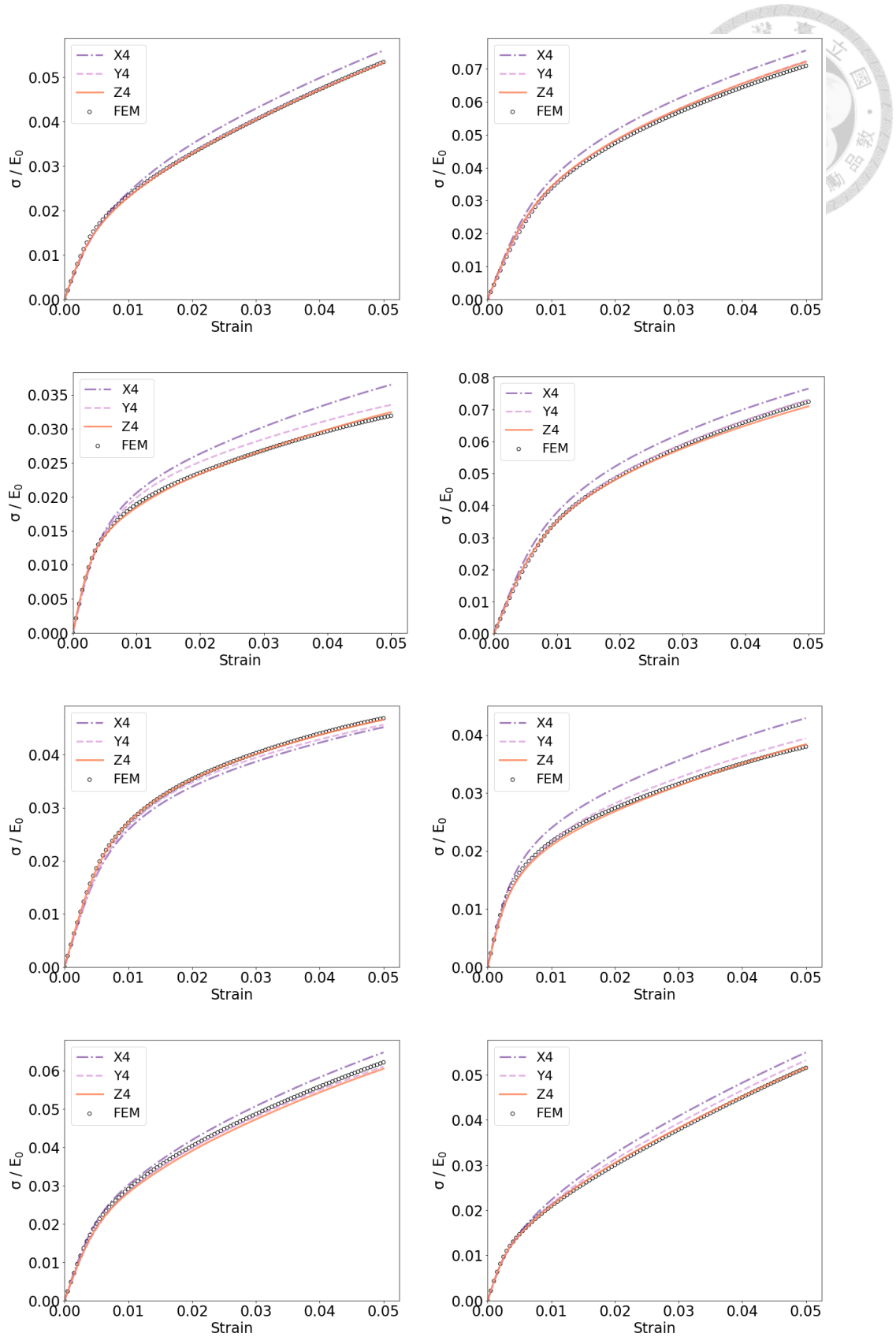


Fig 4.28: 8 comparisons between predicted stress-strain curves by model X4, Y4, and Z4 and the actual stress-strain curve (FEM).

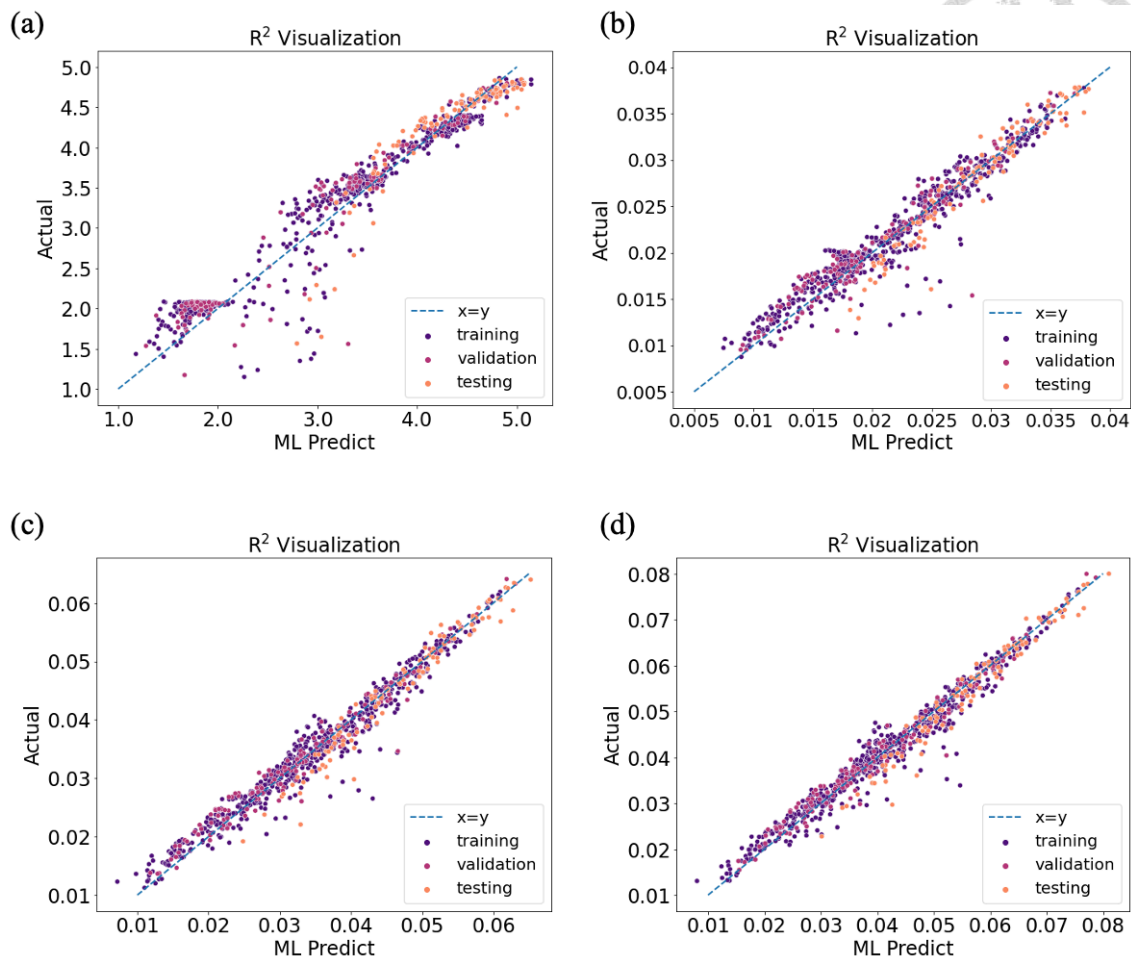


Fig 4.29:  $R^2$  visualization plot of model X4. (a) Stiffness. (b) Stress when strain = 0.01. (c) Stress when strain = 0.03. (d) Stress when strain = 0.05.

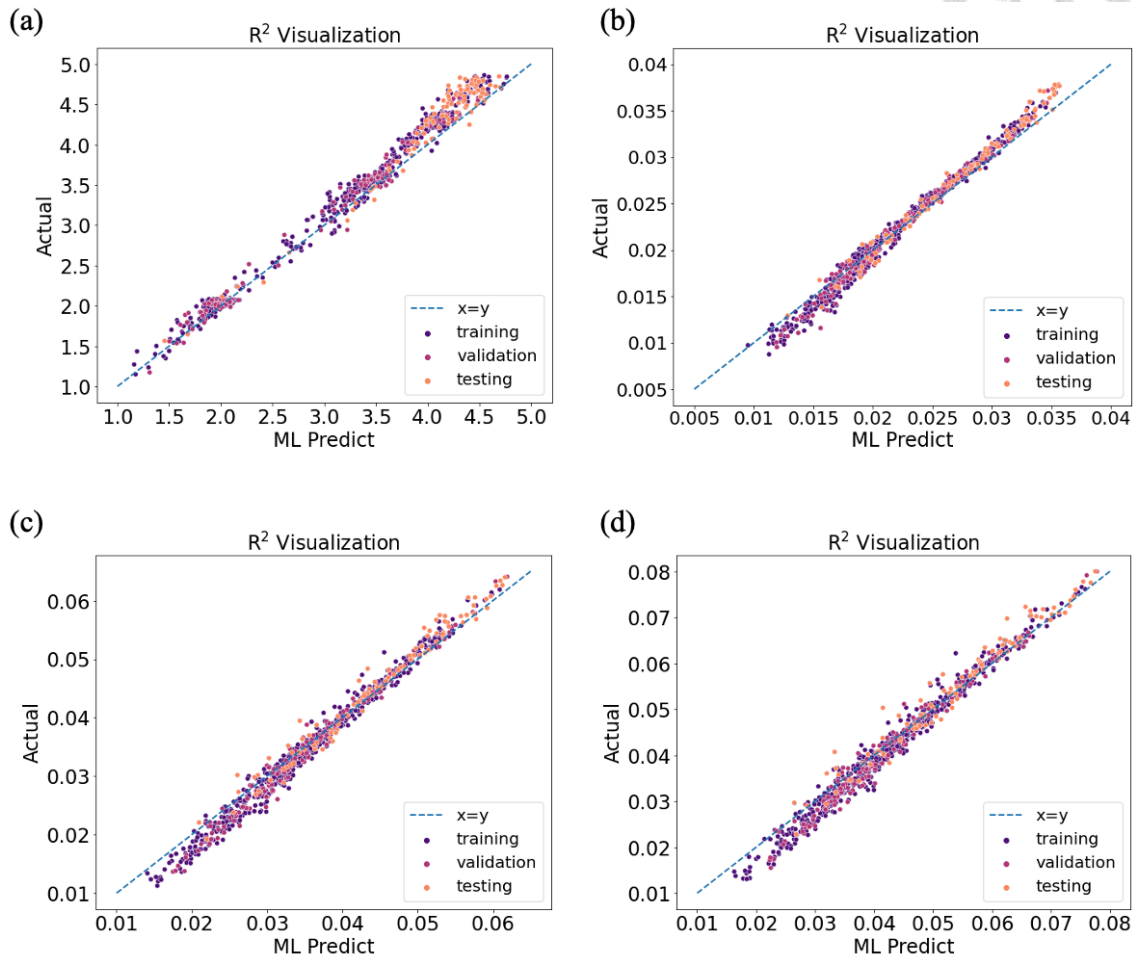


Fig 4.30:  $R^2$  visualization plot of model Y4. (a) Stiffness. (b) Stress when strain = 0.01. (c) Stress when strain = 0.03. (d) Stress when strain = 0.05.

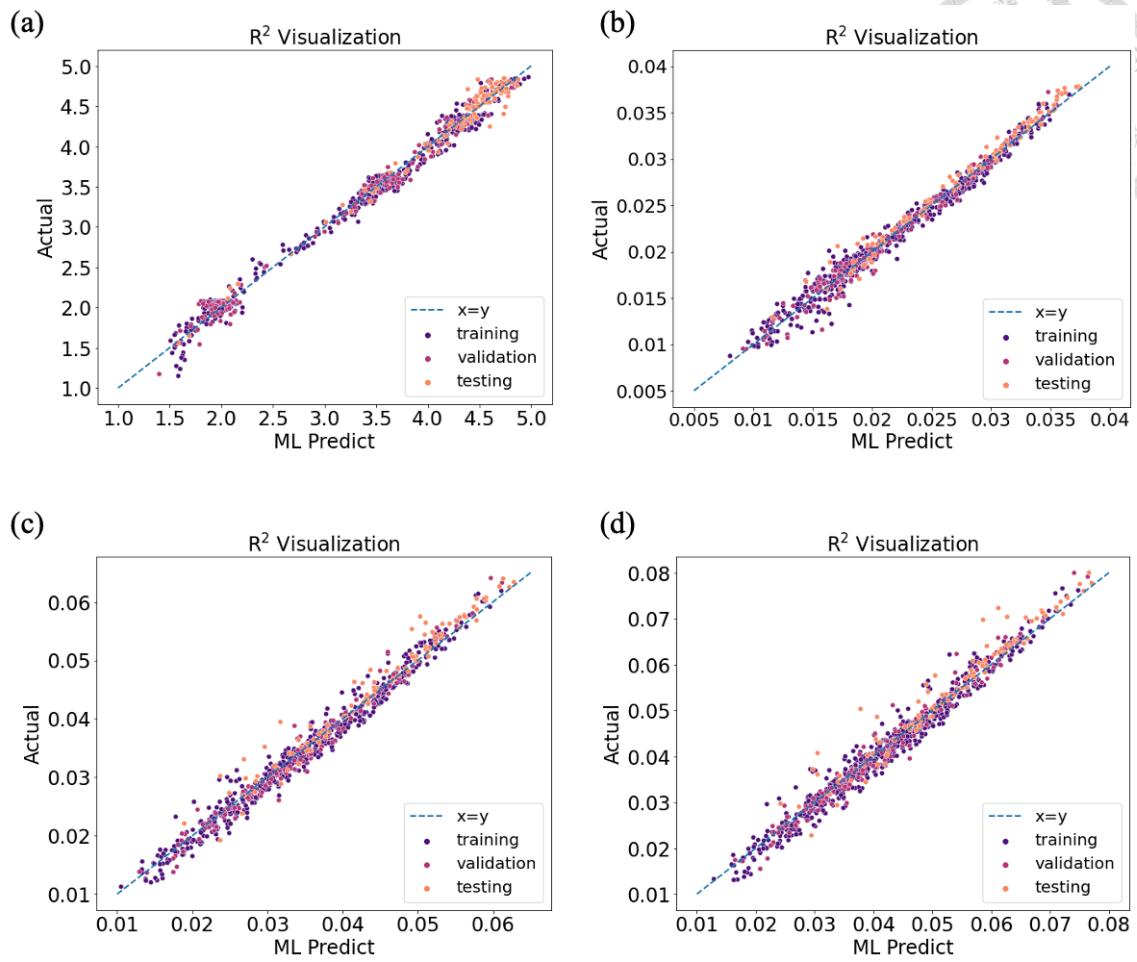


Fig 4.31:  $R^2$  visualization plot of model Z4. (a) Stiffness. (b) Stress when strain = 0.01.

(c) Stress when strain = 0.03. (d) Stress when strain = 0.05.

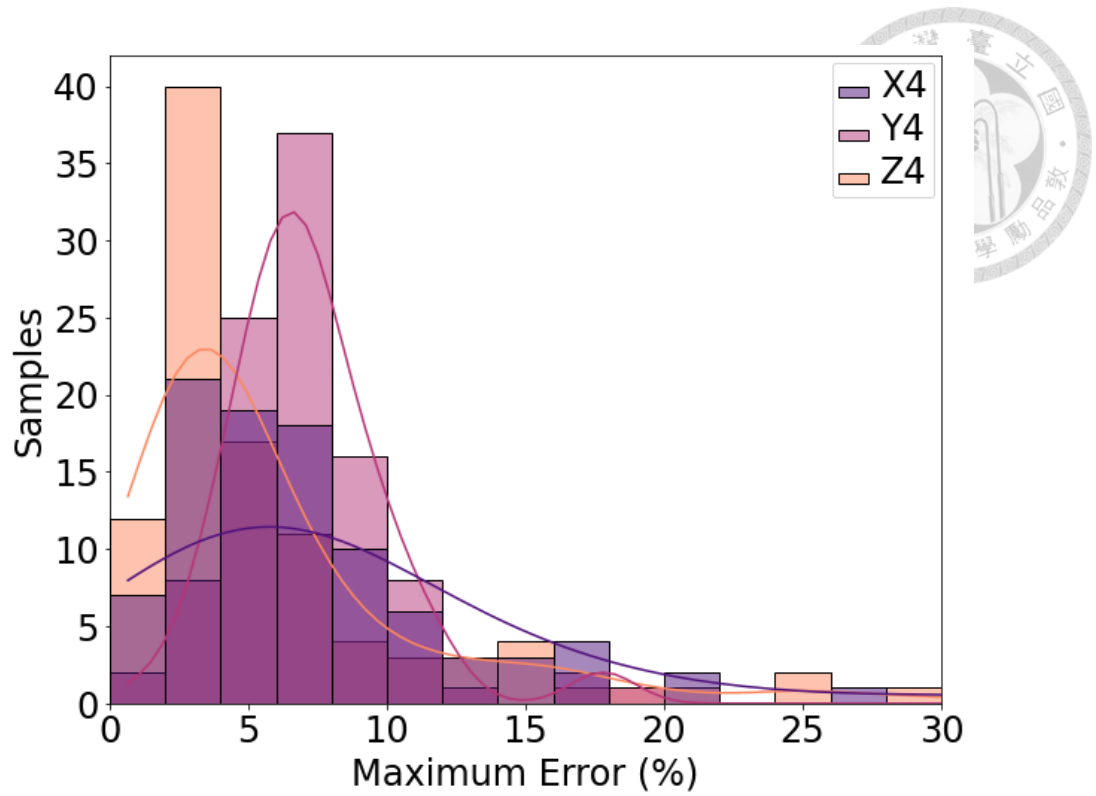


Fig 4.32: Comparison between performances of model X4, Y4, and Z4 in task D.

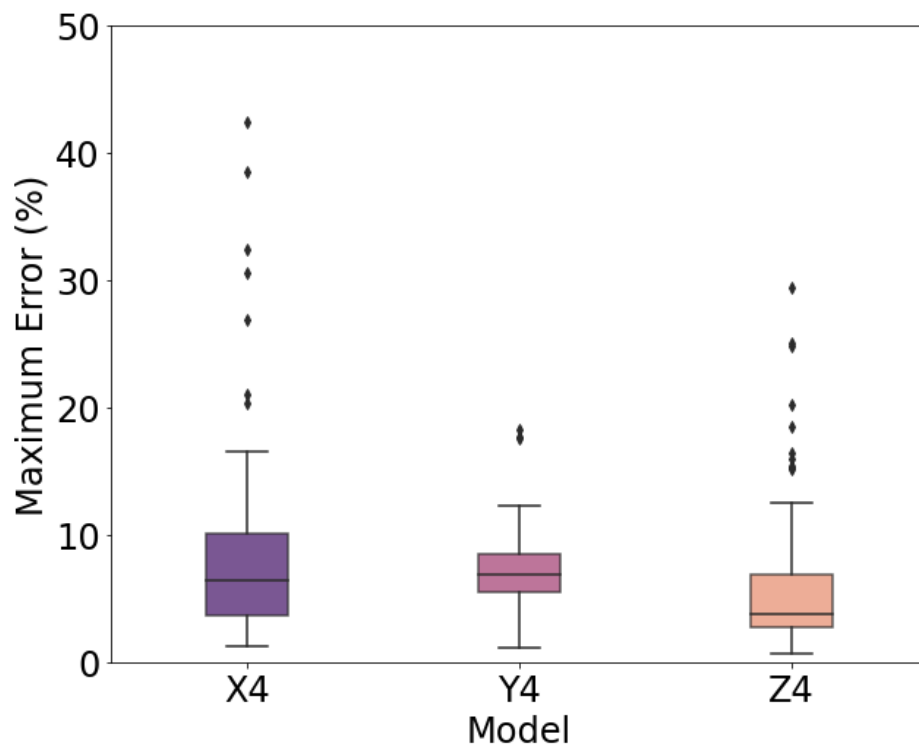
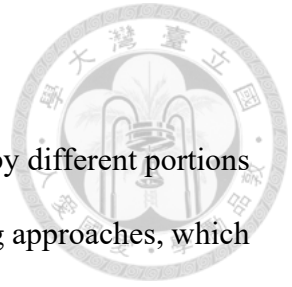


Fig 4.33: Boxplot of maximum error of model X4, Y4, and Z4 in task D.

## 4.4 Summary

This chapter discusses four tasks to predict stress-strain curves by different portions of the SFRC dataset. In each case, three kinds of DNN model training approaches, which are training directly by inputs (model X), TGML (model Y), and two-phase learning (model Z), are adopted and compared. The results show that the predictive performances of model Y and model Z exceed that of model X in all tasks. For model Y and model Z, the  $R^2$  scores of material properties are much higher, and maximum relative errors are lower than that of model X. Additionally, the results also show that by taking predicted Young's modulus instead of aspect ratio as an input feature, the DNN models may capture more data characteristics. Thus, the predictive performance may improve significantly, especially in tasks where the aspect ratios of the training and testing sets are in a different range.





# Chapter 5 Stress-strain Curve Predictions of Bio-inspired Layered Structural Composites

In this chapter, the detailed training setups and the results of the surrogate model are presented. The regression model based on DNN was trained to predict the stress-strain curves. After obtaining the predicted stress-strain curves, we derive the composites' strength and toughness to evaluate the performance of the predictive model. Fig. 5.1 depicts the workflow of the modeling process.

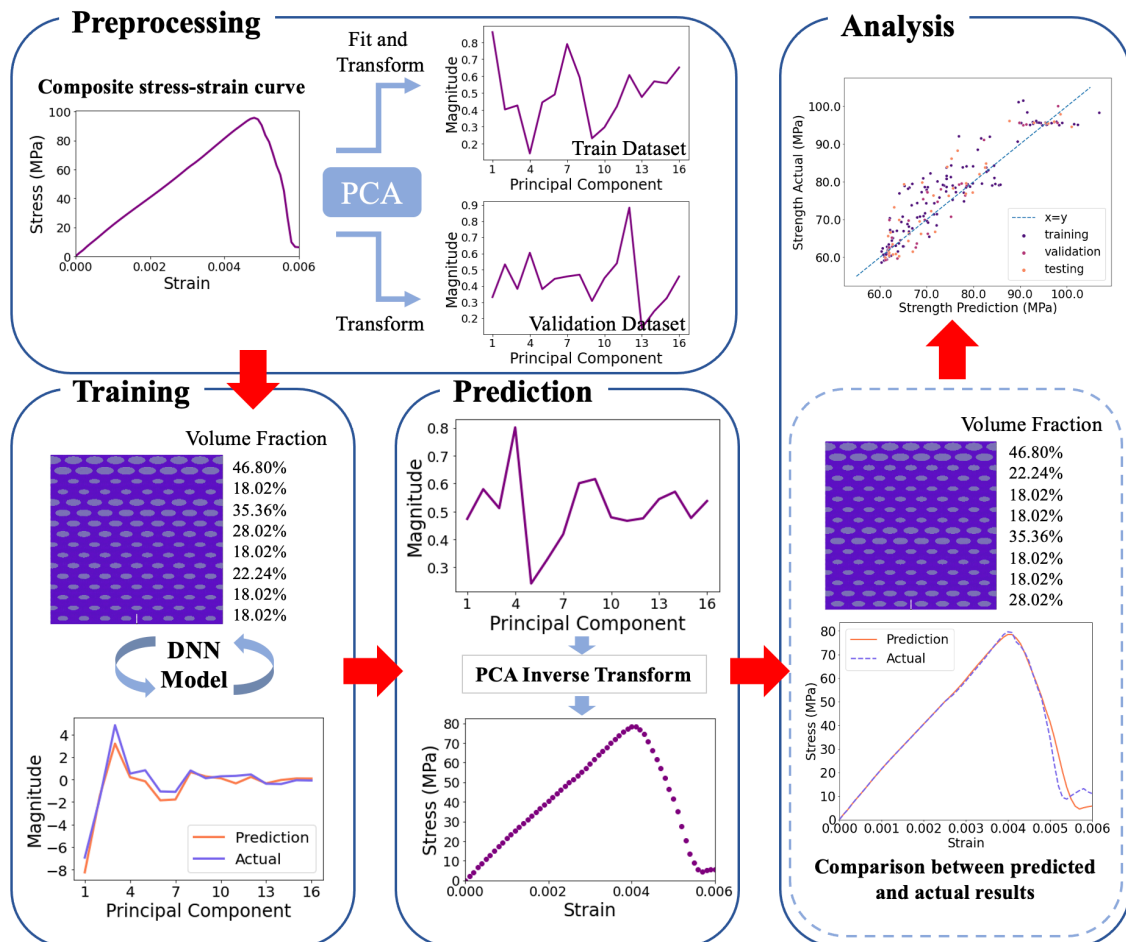


Fig 5.1: Workflow of the modeling process.



## 5.1 Dataset Preparation

We collect our data by LAMMPS simulation as described in section 2.1.2. Because of the computational cost and time limit, 200 samples were generated with volume fractions of inclusion in shuffled order to perform uniaxial tensile simulation. The distribution of strength and toughness of the structures are depicted in Fig 5.2. In this chapter, the simulation results are taken as ground truth. The dataset of 200 samples was divided into training, validation, and testing data in 64%, 16%, and 20%, respectively. Both training and validation sets were used in the training stage, while the testing set was only used to evaluate the final performance of the model. The output data, stress-strain curves obtained from simulations, were preprocessed before training. Firstly, the stress-strain curves are represented as arrays of 61-dimensional stress values. Secondly, the stress vectors are standardized. Since the stress-strain curves contain the fracture behavior, they are more complicated than those of SFRCs mentioned previously. Thus, we need more principal components to recover most of the essential characteristics of the data in this case. The dimensionality of the stress vectors is reduced via PCA to 16-dimension vectors composed of the first 16 principal components. The cumulative explained variance ( $\sum_{i=1}^{16} \lambda_{jj} / \sum_{i=1}^{61} \lambda_{jj}$ ) is higher than 99.5%. The cumulative explained variance ratio with respect to the number of dimensions is depicted in Fig 5.3. Finally, we normalize the 16 most important principal components to values between 0 and 1.

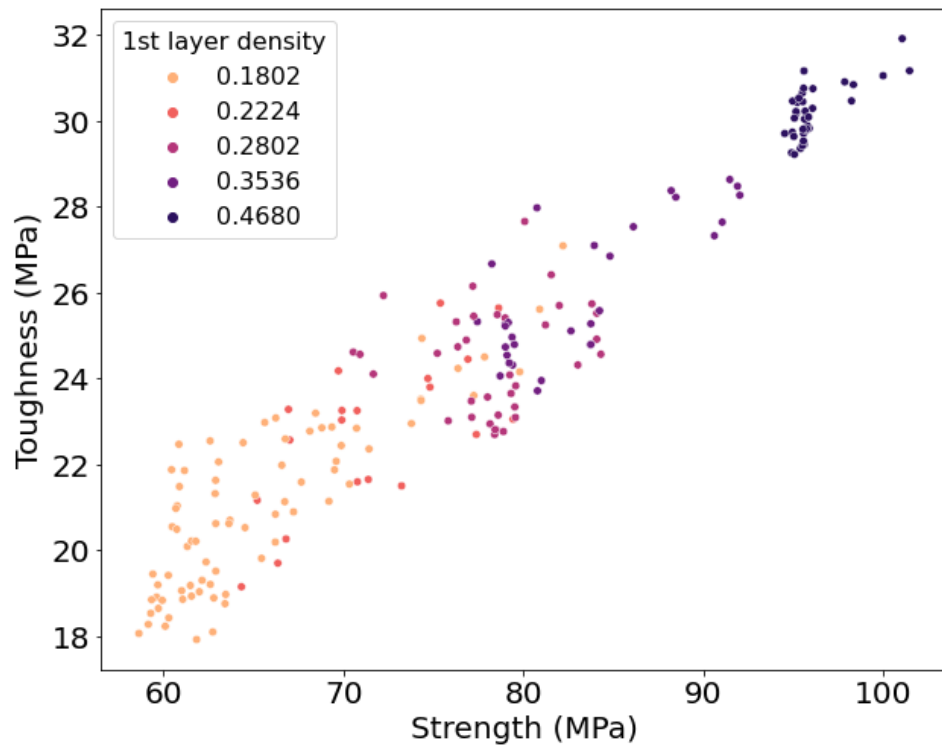


Fig 5.2: Distribution of strength and toughness of the bio-inspired structures dataset.

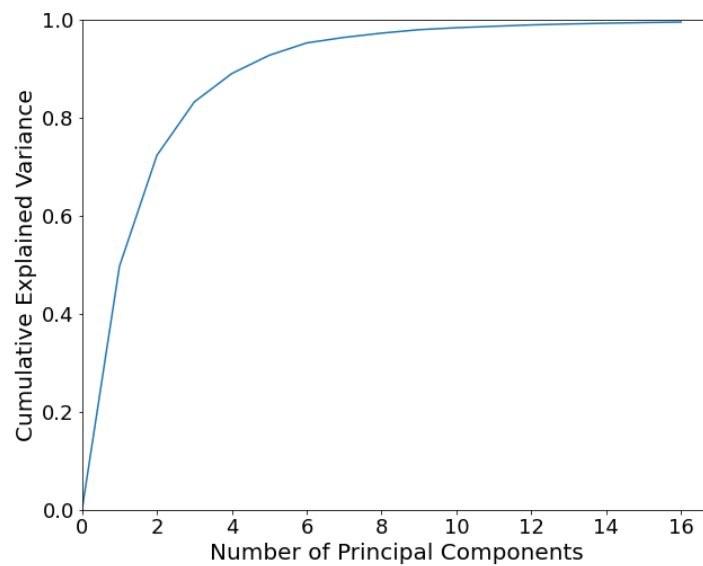


Fig 5.3: Cumulative explained variance ratio with respect to the number of dimensions.



## 5.2 DNN Model Setup

The WMSE is defined for DNN model training as follows:

$$WMSE = \frac{1}{n} \sum_{i=1}^n \sum_{j=1}^{16} \lambda_{jj} (Y_{j,i}^{true} - Y_{j,i}^{pred})^2 \quad (5-1)$$

To search for optimal DNN architecture for this case, we implement the same technique as Chapter 3 to find the best combination of the hyper-parameters. The architecture with the lowest average WMSE after five epochs was chosen in the following search space:

- Number of neurons in each layer = [40, 50, 60, 70, 80, 90, 100]
- Number of hidden unit layers = [3, 4, 5, 6]
- Activation function = [ReLU, LeakyReLU, GeLU, ELU]

The results of the grid-search after five epochs were obtained over 10-fold cross-validation, as demonstrated in Table 5.1 to Table 5.4.

Table 5.1: Average WMSE results with ReLU activation function. The minimum value is highlighted in red.

ReLU Activation Function		Number of hidden unit layers			
		3	4	5	6
Number of neurons	40	0.009584	0.008327	0.009530	0.008395
	50	0.009454	0.008087	0.009254	0.007718
	60	0.008541	0.008644	0.008980	0.008726
	70	0.009299	0.008449	0.008905	0.007817
	80	0.009346	0.008524	0.008267	0.007780
	90	0.008200	0.008559	0.007542	0.008233
	100	0.008490	0.008426	0.008386	0.008721

Table 5.2: Average WMSE results with LeakyReLU activation function. The minimum value is highlighted in red.

LeakyReLU Activation Function		Number of hidden unit layers			
		3	4	5	6
Number of neurons	40	0.009202	0.008821	0.008509	0.008473
	50	0.008186	0.008930	0.007613	0.008418
	60	0.008791	0.008402	0.008623	0.008623
	70	0.008357	0.008513	0.007927	0.007656
	80	0.007812	0.008455	0.008233	0.007830
	90	0.008889	0.008218	0.007644	0.007705
	100	0.009529	0.008512	0.008007	0.007574

Table 5.3: Average WMSE results with GeLU activation function. The minimum value is highlighted in red.

GeLU Activation Function		Number of hidden unit layers			
		3	4	5	6
Number of neurons	40	0.010042	0.010022	0.009481	0.008369
	50	0.009455	0.009262	0.008679	0.008492
	60	0.009259	0.009000	0.009099	0.008459
	70	0.010366	0.009255	0.008243	0.008881
	80	0.010081	0.008503	0.008539	0.009053
	90	0.009563	0.008531	0.008197	0.008514
	100	0.008786	0.008241	0.008608	0.008075

Table 5.4: Average WMSE results with ELU activation function. The minimum value is highlighted in red.

ELU Activation Function		Number of hidden unit layers			
		3	4	5	6
Number of neurons	40	0.008103	0.007626	0.007975	0.008203
	50	0.008341	0.007528	0.008114	0.007158
	60	0.007646	0.007180	0.008017	0.007397
	70	0.007983	0.007717	0.007201	0.007052
	80	0.007608	0.006787	0.007161	0.005953
	90	0.007358	0.007370	0.006703	0.006511
	100	0.006677	0.007026	0.005963	0.006240

The chosen DNN architecture in this chapter has 80 neurons in each dense layer, six hidden unit layers, and ELU as an activation function. This DNN model has 35,376 trainable parameters. The WMSE is adopted to show the DNN model that each principal component has particular importance. The Adam optimizer was applied to train the DNN model. Also, we set the batch size to 8 in these models. Furthermore, early stopping was adopted once the validation loss did not improve within 20 steps to avoid over-fitting.

After the training, we transform the outputs, i.e., the 16-dimensional normalized principal components, into the 61-dimensional stress-strain curves via reverse normalization, reverse PCA, and reverse standardization.

### 5.3 Results and Discussion

Table 5.5: Evaluation metrics of the predictive model.

Properties	R <sup>2</sup> score			MSE			MAE		
	Train	Valid.	Test	Train	Valid.	Test	Train	Valid.	Test
Strength	0.8030	0.8733	0.8027	28.0780	16.4618	27.4922	3.8987	3.2920	3.7484
Toughness	0.8657	0.8883	0.8533	1.5882	1.2258	1.7533	1.0051	0.9091	1.0524

The model with the minimum loss on validation data was selected as our final predictive model. Table 5.5 lists the evaluation metrics of R<sup>2</sup> scores, MSE, and MAE corresponding to training, validation, and testing data. Additionally, the loss history during training, comparison examples between predicted and actual stress-strain curves (from simulation), and regression scatter plots are plotted in Fig 5.4 to Fig 5.7. From the results, we can see great performances of R<sup>2</sup> score of toughness higher than 0.85 and R<sup>2</sup> score of strength higher than 0.8 when compared to ground truth (LAMMPS simulation). These results show that DNN models have great potential to be used as surrogate models to efficiently and accurately predict stress-strain curves by simple descriptions of the structures.

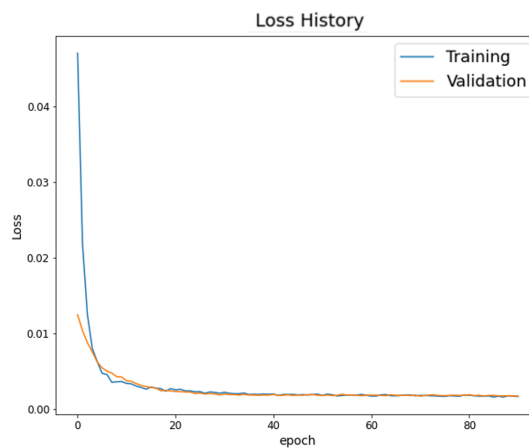


Fig 5.4: Loss history of the predictive model.

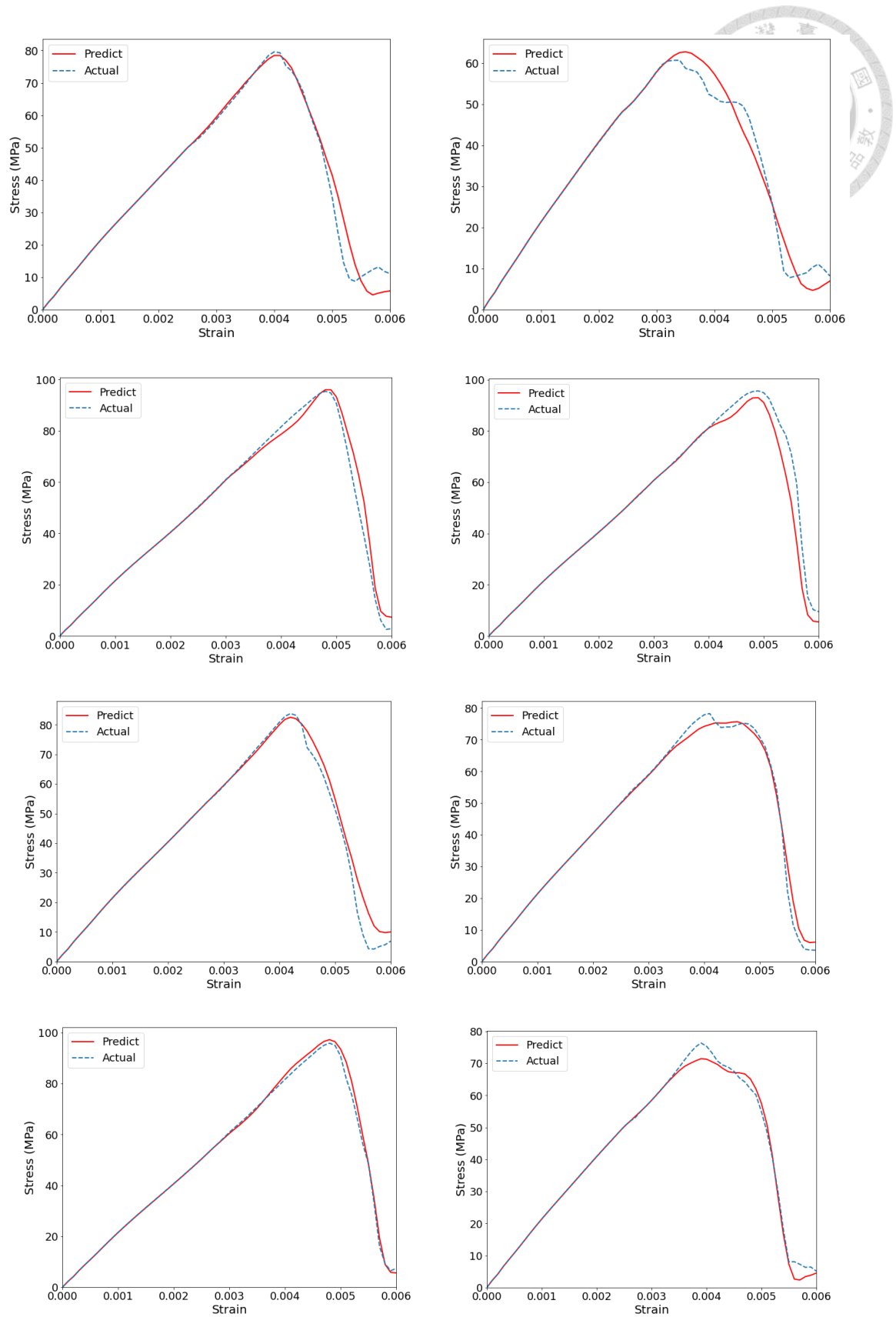


Fig 5.5: 8 comparisons between the predicted stress-strain curve and the actual stress-strain curve (LAMMPS simulation).

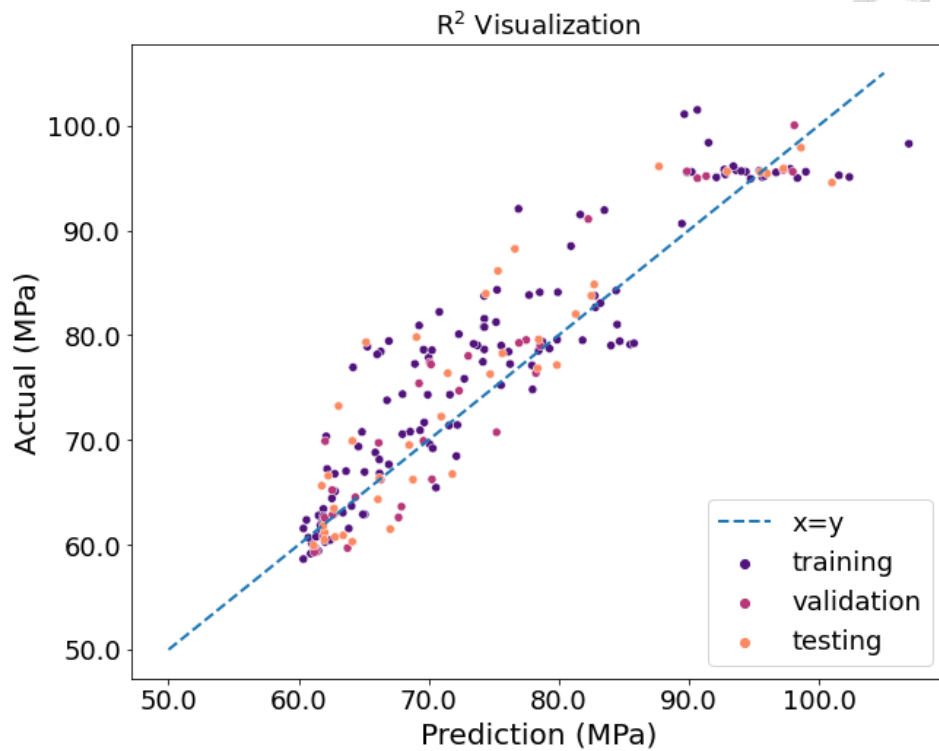


Fig 5.6: R<sup>2</sup> visualization plot of strength.

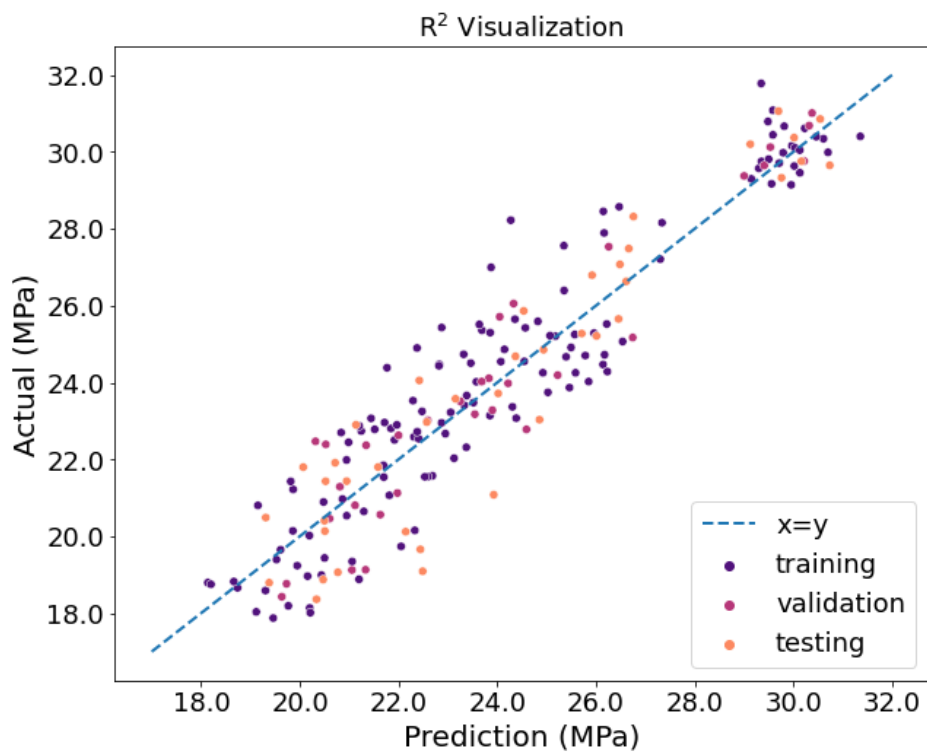


Fig 5.7: R<sup>2</sup> visualization plot of toughness.



## 5.4 Properties Prediction of Whole Design Space

In this work, the volume fraction of each layer is 18.02%, 22.24%, 28.02%, 35.36%, and 46.80%. As described in section 2.1.2, in our design space, the volume fraction of each layer is in shuffled order, which leads to the result of 1620 structures. As shown in Fig 5.8, the properties of all structures in the design space are predicted by our DNN model. We can find out that the results in Fig 5.8 demonstrate a trend that a higher volume fraction of the first layer leads to higher strength and toughness of the composite structures, which is the same trend as our dataset (see Fig 5.2). This result shows that the DNN model can learn the characteristics of the composite structure data.

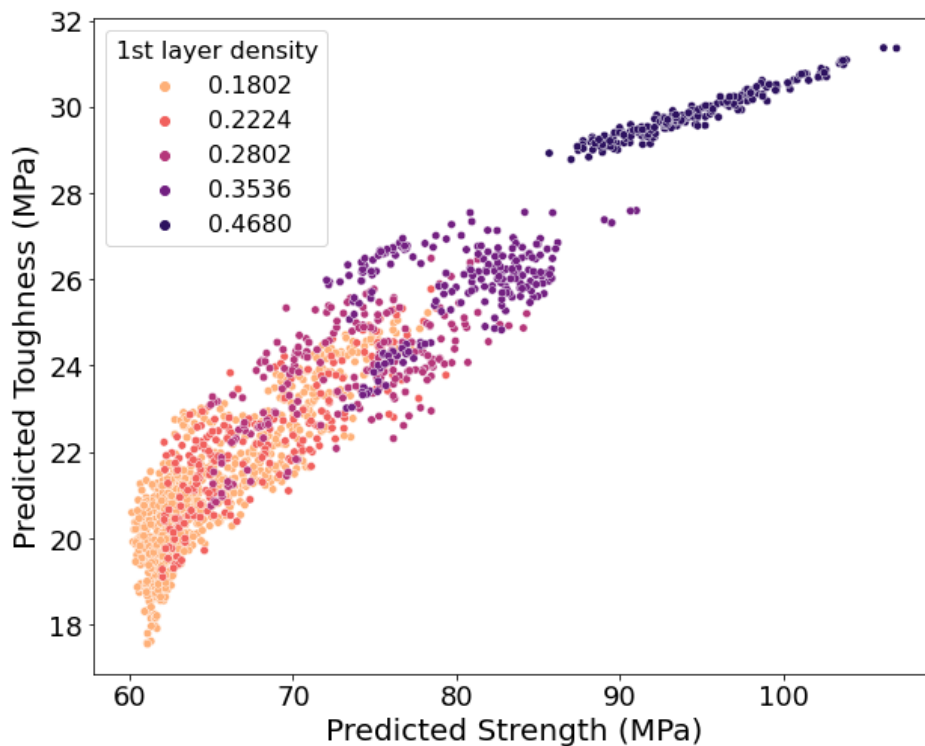


Fig 5.8: Predicted material properties distribution of the whole design space.

## 5.5 Summary

In this chapter, a DNN predictive model was trained to predict the stress-strain curves based on the bio-inspired layered structural composite dataset of 200 samples. Our model performs well in predicting stress-strain curves with  $R^2$  scores of 0.85 in toughness and 0.8 in strength. The results show great potential to design composites with mechanical behavior beyond the elastic zone and can be expanded easily to other design spaces.



## Chapter 6 Conclusions and Future Work

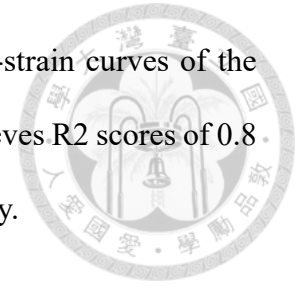


### 6.1 Conclusions

In attribute to machine learning, novel and advanced techniques are applied to various research fields, and material design is no exception. By adopting the combination of additive manufacturing or computational methods and ML techniques, we can explore the material design space more easily and efficiently. This study provides a machine learning approach to predict stress-strain curves of SFRCs that considers the effect of interphase via training a deep learning network with the FEA dataset. Moreover, the effects of adopting TGML and two-phase learning methods are discussed. In addition, we provide another DNN model to predict stress-strain curves of bio-inspired layered structural composites. Based on the work presented in this thesis, conclusions can be drawn as follows:

1. A design space for SFRC materials is investigated. The SFRC dataset is created from FEM simulation results.
2. A machine learning approach is provided to predict stress-strain curves of the SFRCs. The predictive model results in R2 scores higher than 0.9 for stress in different strains and stiffness, along with the maximum relative error lower than 10% for most of the predicted stress-strain curves compared to ground truth (FEM).
3. The TGML and two-phase learning frameworks are proposed. The predictive models show better performances on R2 score or maximum error when predicting stress-strain curves of SFRCs.
4. A design space for bio-inspired layered structural composites is investigated. The bio-inspired composite dataset is created from LAMMPS simulation results.

5. A machine learning approach is provided to predict stress-strain curves of the bio-inspired layered composites. The predictive model achieves R2 scores of 0.8 and 0.85 with respect to strength and toughness, respectively.



## 6.2 Future Work

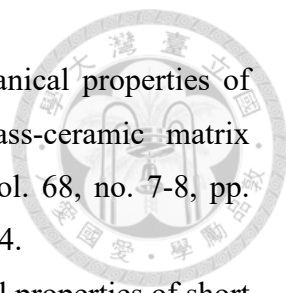
In this thesis, we focus on the DNN predictive models for SFRCs and bio-inspired layered structural composites. Possible directions to extend current work are suggested below:

1. *Inverse material design.* In this work, we see material properties as inputs and the stress-strain curves as answers to the ML models. However, in practical applications, we know our requirements for the material, but it is hard for us to figure out what the composition of that composite can be. Hence, inverse material design can be done by the same dataset but using the stress-strain curves as inputs and material properties as answers to the ML model.
2. *Exploration in other design spaces.* The ML framework mentioned in this thesis is suitable for many material design spaces. As long as the structures' material composition or geometry can be described or quantified, this ML approach can be applied when data is sufficient. It is expected that only a small effort is required to adopt this framework in other design spaces.

## References



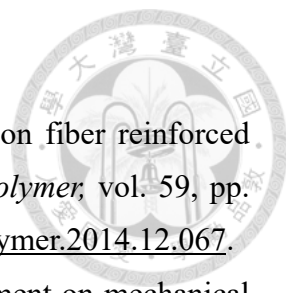
- [1] W. Song *et al.*, "Cross-Scale Biological Models of Species for Future Biomimetic Composite Design: A Review," *Coatings*, vol. 11, no. 11, 2021, doi: 10.3390/coatings11111297.
- [2] U. G. Wegst, H. Bai, E. Saiz, A. P. Tomsia, and R. O. Ritchie, "Bioinspired structural materials," *Nat Mater*, vol. 14, no. 1, pp. 23-36, Jan 2015, doi: 10.1038/nmat4089.
- [3] S. David Muzel, E. P. Bonhin, N. M. Guimaraes, and E. S. Guidi, "Application of the Finite Element Method in the Analysis of Composite Materials: A Review," *Polymers (Basel)*, vol. 12, no. 4, Apr 4 2020, doi: 10.3390/polym12040818.
- [4] J. P. Firmo, M. G. Roquette, J. R. Correia, and A. S. Azevedo, "Influence of elevated temperatures on epoxy adhesive used in CFRP strengthening systems for civil engineering applications," *Int. J. Adhes. Adhes.*, vol. 93, 2019, doi: 10.1016/j.ijadhadh.2019.01.027.
- [5] D. K. Koli, G. Agnihotri, and R. Purohit, "Advanced Aluminium Matrix Composites: The Critical Need of Automotive and Aerospace Engineering Fields," *Materials Today: Proceedings*, vol. 2, no. 4-5, pp. 3032-3041, 2015, doi: 10.1016/j.matpr.2015.07.290.
- [6] M. Arif, M. Asif, and I. Ahmed, "Advanced composite material for aerospace application—A review," *Int. J. Eng. Manuf. Sci*, vol. 7, no. 2, pp. 393-409, 2017.
- [7] D. Mathijssen, "DARPA: inventing the future of military technology," *Reinforced Plastics*, vol. 59, no. 5, pp. 233-237, 2015, doi: 10.1016/j.repl.2015.08.048.
- [8] G.-Z. Kang, C. Yang, and J.-x. Zhang, "Tensile properties of randomly oriented short  $\delta$ -Al<sub>2</sub>O<sub>3</sub> fiber reinforced aluminum alloy composites. I. Microstructure characteristics, fracture mechanisms and strength prediction," *Composites Part A: Applied Science and Manufacturing*, vol. 33, no. 5, pp. 647-656, 2002/05/01/ 2002, doi: [https://doi.org/10.1016/S1359-835X\(02\)00005-2](https://doi.org/10.1016/S1359-835X(02)00005-2).
- [9] L. G. Hou *et al.*, "Microstructure, mechanical properties and thermal conductivity of the short carbon fiber reinforced magnesium matrix composites," (in English), *J. Alloy. Compd.*, Article vol. 695, pp. 2820-2826, Feb 2017, doi: 10.1016/j.jallcom.2016.11.422.

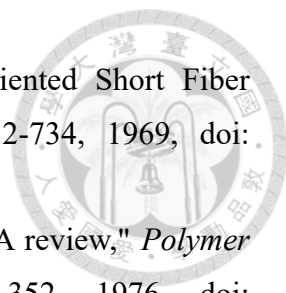
- 
- [10] F. Ye, L. M. Liu, and L. J. Huang, "Fabrication and mechanical properties of carbon short fiber reinforced barium aluminosilicate glass-ceramic matrix composites," (in English), *Compos. Sci. Technol.*, Article vol. 68, no. 7-8, pp. 1710-1717, Jun 2008, doi: 10.1016/j.compscitech.2008.02.004.
- [11] F. Y. Yang, X. H. Zhang, J. C. Han, and S. Y. Du, "Mechanical properties of short carbon fiber reinforced ZrB<sub>2</sub>-SiC ceramic matrix composites," (in English), *Mater. Lett.*, Article vol. 62, no. 17-18, pp. 2925-2927, Jun 2008, doi: 10.1016/j.matlet.2008.01.076.
- [12] Z. S. Hua, G. C. Yao, J. F. Ma, and M. L. Zhang, "Fabrication and mechanical properties of short ZrO<sub>2</sub> fiber reinforced NiFe<sub>2</sub>O<sub>4</sub> matrix composites," (in English), *Ceram. Int.*, Article vol. 39, no. 4, pp. 3699-3708, May 2013, doi: 10.1016/j.ceramint.2012.10.203.
- [13] S. Mortazavian and A. Fatemi, "Tensile behavior and modeling of short fiber-reinforced polymer composites including temperature and strain rate effects," *J. Thermoplast. Compos. Mater.*, vol. 30, no. 10, pp. 1414-1437, 2016, doi: 10.1177/0892705716632863.
- [14] J. Cui, S. Wang, S. Wang, G. Li, P. Wang, and C. Liang, "The Effects of Strain Rates on Mechanical Properties and Failure Behavior of Long Glass Fiber Reinforced Thermoplastic Composites," *Polymers (Basel)*, vol. 11, no. 12, Dec 5 2019, doi: 10.3390/polym11122019.
- [15] Z. K. Zhao *et al.*, "Mechanical and tribological properties of short glass fiber and short carbon fiber reinforced polyethersulfone composites: A comparative study," (in English), *Compos. Commun.*, Article vol. 8, pp. 1-6, Jun 2018, doi: 10.1016/j.coco.2018.02.001.
- [16] L. Mohammed, M. N. M. Ansari, G. Pua, M. Jawaid, and M. S. Islam, "A Review on Natural Fiber Reinforced Polymer Composite and Its Applications," *International Journal of Polymer Science*, vol. 2015, pp. 1-15, 2015, doi: 10.1155/2015/243947.
- [17] Jagadish, M. Rajakumaran, and A. Ray, "Investigation on mechanical properties of pineapple leaf-based short fiber-reinforced polymer composite from selected Indian (northeastern part) cultivars," (in English), *J. Thermoplast. Compos. Mater.*, Article vol. 33, no. 3, pp. 324-342, Mar 2020, doi: 10.1177/0892705718805535.
- [18] M. Szpieg, M. Wysocki, and L. E. Asp, "Mechanical performance and modelling of a fully recycled modified CF/PP composite," *J. Compos Mater.*, vol. 46, no. 12,

- pp. 1503-1517, 2011, doi: 10.1177/0021998311423860.
- [19] H. Meftah, S. Tamboura, J. Fitoussi, H. BenDaly, and A. Tcharkhtchi, "Characterization of a New Fully Recycled Carbon Fiber Reinforced Composite Subjected to High Strain Rate Tension," (in English), *Appl. Compos. Mater.*, Article vol. 25, no. 3, pp. 507-526, Jun 2018, doi: 10.1007/s10443-017-9632-6.
- [20] M. S. Rouhi, M. Juntikka, J. Landberg, and M. Wysocki, "Assessing models for the prediction of mechanical properties for the recycled short fibre composites," (in English), *J. Reinf. Plast. Compos.*, Article vol. 38, no. 10, pp. 454-466, May 2019, doi: 10.1177/0731684418824404.
- [21] T. Lin, D. Jia, P. He, M. Wang, and D. Liang, "Effects of fiber length on mechanical properties and fracture behavior of short carbon fiber reinforced geopolymer matrix composites," (in English), *Mater. Sci. Eng. A-Struct. Mater. Prop. Microstruct. Process.*, Article vol. 497, no. 1-2, pp. 181-185, Dec 2008, doi: 10.1016/j.msea.2008.06.040.
- [22] N. Ferreira, C. Capela, J. M. Ferreira, and J. M. Costa, "Effect of Water and Fiber Length on the Mechanical Properties of Polypropylene Matrix Composites," (in English), *Fiber. Polym.*, Article vol. 15, no. 5, pp. 1017-1022, May 2014, doi: 10.1007/s12221-014-1017-y.
- [23] C. Jayaseelan, P. Padmanabhan, A. Athijayamani, and K. Ramanathan, "Comparative Investigation of Mechanical Properties of Epoxy Composites Reinforced with Short Fibers, Macro Particles, and Micro Particles," (in English), *BioResources*, Article vol. 12, no. 2, pp. 2864-2871, 2017, doi: 10.15376/biores.12.2.2864-2871.
- [24] X. Y. Wang, F. Luo, X. M. Yu, D. M. Zhu, and W. C. Zhou, "Influence of short carbon fiber content on mechanical and dielectric properties of C-fiber/Si<sub>3</sub>N<sub>4</sub> composites," (in English), *Scr. Mater.*, Article vol. 57, no. 4, pp. 309-312, Aug 2007, doi: 10.1016/j.scriptamat.2007.04.030.
- [25] C. Capela, S. E. Oliveira, and J. A. M. Ferreira, "Mechanical behavior of high dosage short carbon fiber reinforced epoxy composites," (in English), *Fiber. Polym.*, Article vol. 18, no. 6, pp. 1200-1207, Jun 2017, doi: 10.1007/s12221-017-7246-0.
- [26] W. W. Li, L. Liu, and B. Shen, "Effect of Ni-coated short carbon fibers on the mechanical and electrical properties of epoxy composites," (in English), *Fiber. Polym.*, Article vol. 14, no. 9, pp. 1515-1520, Sep 2013, doi: 10.1007/s12221-

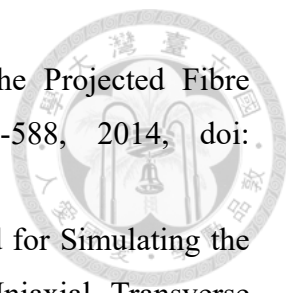


013-1515-3.

- 
- [27] F. Li *et al.*, "Enhanced mechanical properties of short carbon fiber reinforced polyethersulfone composites by graphene oxide coating," *Polymer*, vol. 59, pp. 155-165, 2015/02/24/ 2015, doi: <https://doi.org/10.1016/j.polymer.2014.12.067>.
- [28] H. F. Lei, Z. Q. Zhang, and B. Liu, "Effect of fiber arrangement on mechanical properties of short fiber reinforced composites," (in English), *Compos. Sci. Technol.*, Article vol. 72, no. 4, pp. 506-514, Feb 2012, doi: 10.1016/j.compscitech.2011.12.011.
- [29] W. Tian, L. Qi, C. Su, J. Zhou, and Z. Jing, "Numerical simulation on elastic properties of short-fiber-reinforced metal matrix composites: Effect of fiber orientation," *Composite Structures*, vol. 152, pp. 408-417, 2016, doi: 10.1016/j.compstruct.2016.05.046.
- [30] L. P. Canal, C. González, J. Segurado, and J. Llorca, "Intraply fracture of fiber-reinforced composites: Microscopic mechanisms and modeling," *Compos. Sci. Technol.*, vol. 72, no. 11, pp. 1223-1232, 2012, doi: 10.1016/j.compscitech.2012.04.008.
- [31] L. Riaño, L. Belec, J.-F. Chailan, and Y. Joliff, "Effect of interphase region on the elastic behavior of unidirectional glass-fiber/epoxy composites," *Composite Structures*, vol. 198, pp. 109-116, 2018.
- [32] J. Ge, L. Qi, X. Chao, Y. Xue, X. Hou, and H. Li, "The effects of interphase parameters on transverse elastic properties of Carbon–Carbon composites based on FE model," *Composite Structures*, vol. 268, 2021, doi: 10.1016/j.compstruct.2021.113961.
- [33] L. Wang, G. Nygren, R. L. Karkkainen, and Q. Yang, "A multiscale approach for virtual testing of highly aligned short carbon fiber composites," *Composite Structures*, vol. 230, 2019, doi: 10.1016/j.compstruct.2019.111462.
- [34] M. Takayanagi, S. Uemura, and S. Minami, "Application of equivalent model method to dynamic rheo-optical properties of crystalline polymer," *Journal of Polymer Science Part C: Polymer Symposia*, vol. 5, no. 1, pp. 113-122, 1964, doi: <https://doi.org/10.1002/polc.5070050111>.
- [35] Y. Zare and K. Y. Rhee, "Expansion of Takayanagi model by interphase characteristics and filler size to approximate the tensile modulus of halloysite-nanotube-filled system," *Journal of Materials Research and Technology*, vol. 16, pp. 1628-1636, 2022, doi: 10.1016/j.jmrt.2021.12.082.

- 
- [36] J. C. Halpin, "Stiffness and Expansion Estimates for Oriented Short Fiber Composites," *J. Compos Mater.*, vol. 3, no. 4, pp. 732-734, 1969, doi: 10.1177/002199836900300419.
- [37] J. C. Halpin and J. L. Kardos, "The Halpin-Tsai equations: A review," *Polymer Engineering & Science*, vol. 16, no. 5, pp. 344-352, 1976, doi: <https://doi.org/10.1002/pen.760160512>.
- [38] Z. Luo, X. Li, J. Shang, H. Zhu, and D. Fang, "Modified rule of mixtures and Halpin–Tsai model for prediction of tensile strength of micron-sized reinforced composites and Young’s modulus of multiscale reinforced composites for direct extrusion fabrication," *Advances in Mechanical Engineering*, vol. 10, no. 7, 2018, doi: 10.1177/1687814018785286.
- [39] R. M. Christensen, "Asymptotic modulus results for composites containing randomly oriented fibers," *International Journal of Solids and Structures*, vol. 12, no. 7, pp. 537-544, 1976, doi: 10.1016/0020-7683(76)90036-6.
- [40] J. Epaarachchi, H. Ku, and K. Gohel, "A Simplified Empirical Model for Prediction of Mechanical Properties of Random Short Fiber/Vinylester Composites," (in English), *J. Compos Mater.*, Article vol. 44, no. 6, pp. 779-788, Mar 2010, doi: 10.1177/0021998309346383.
- [41] I. Doghri, L. Brassart, L. Adam, and J. S. Gérard, "A second-moment incremental formulation for the mean-field homogenization of elasto-plastic composites," *International Journal of Plasticity*, vol. 27, no. 3, pp. 352-371, 2011, doi: 10.1016/j.ijplas.2010.06.004.
- [42] V. Müller, B. Brylka, F. Dillenberger, R. Glöckner, S. Kolling, and T. Böhlke, "Homogenization of elastic properties of short-fiber reinforced composites based on measured microstructure data," *J. Compos Mater.*, vol. 50, no. 3, pp. 297-312, 2015, doi: 10.1177/0021998315574314.
- [43] P. A. Hessman, F. Welschinger, K. Hornberger, and T. Böhlke, "On mean field homogenization schemes for short fiber reinforced composites: Unified formulation, application and benchmark," *International Journal of Solids and Structures*, vol. 230-231, 2021, doi: 10.1016/j.ijsolstr.2021.111141.
- [44] A. Gupta, S. Hasanov, I. Fidan, and Z. Zhang, "Homogenized modeling approach for effective property prediction of 3D-printed short fibers reinforced polymer matrix composite material," *The International Journal of Advanced Manufacturing Technology*, vol. 118, no. 11-12, pp. 4161-4178, 2021, doi:

- 10.1007/s00170-021-08230-9.
- [45] O. Pierard, C. Friebel, and I. Doghri, "Mean-field homogenization of multi-phase thermo-elastic composites: a general framework and its validation," *Compos. Sci. Technol.*, vol. 64, no. 10-11, pp. 1587-1603, 2004, doi: 10.1016/j.compscitech.2003.11.009.
- [46] J. Jung, S. Lee, B. Ryu, and S. Ryu, "Investigation of effective thermoelectric properties of composite with interfacial resistance using micromechanics-based homogenisation," *International Journal of Heat and Mass Transfer*, vol. 144, 2019, doi: 10.1016/j.ijheatmasstransfer.2019.118620.
- [47] S. Ryu, S. Lee, J. Jung, J. Lee, and Y. Kim, "Micromechanics-Based Homogenization of the Effective Physical Properties of Composites With an Anisotropic Matrix and Interfacial Imperfections," *Frontiers in Materials*, vol. 6, 2019, doi: 10.3389/fmats.2019.00021.
- [48] V. Müller, M. Kabel, H. Andrä, and T. Böhlke, "Homogenization of linear elastic properties of short-fiber reinforced composites – A comparison of mean field and voxel-based methods," *International Journal of Solids and Structures*, vol. 67-68, pp. 56-70, 2015, doi: 10.1016/j.ijsolstr.2015.02.030.
- [49] S. Y. Fu, B. Lauke, E. Mäder, C. Y. Yue, and X. Hu, "Tensile properties of short-glass-fiber- and short-carbon-fiber-reinforced polypropylene composites," *Composites Part A: Applied Science and Manufacturing*, vol. 31, no. 10, pp. 1117-1125, 2000/10/01/ 2000, doi: [https://doi.org/10.1016/S1359-835X\(00\)00068-3](https://doi.org/10.1016/S1359-835X(00)00068-3).
- [50] H. L. Tang, X. R. Zeng, X. B. Xiong, L. Li, and J. Z. Zou, "Mechanical and tribological properties of short-fiber-reinforced SiC composites," (in English), *Tribol. Int.*, Article vol. 42, no. 6, pp. 823-827, Jun 2009, doi: 10.1016/j.triboint.2008.10.017.
- [51] A. P. Sharma, S. H. Khan, and V. Parameswaran, "Experimental and numerical investigation on the uni-axial tensile response and failure of fiber metal laminates," *Composites Part B: Engineering*, vol. 125, pp. 259-274, 2017, doi: 10.1016/j.compositesb.2017.05.072.
- [52] Z. X. Lu, Z. S. Yuan, and Q. Liu, "3D numerical simulation for the elastic properties of random fiber composites with a wide range of fiber aspect ratios," (in English), *Comput. Mater. Sci.*, Article vol. 90, pp. 123-129, Jul 2014, doi: 10.1016/j.commatsci.2014.04.007.
- [53] H. Kebir and R. Ayad, "A specific finite element procedure for the analysis of

- 
- elastic behaviour of short fibre reinforced composites. The Projected Fibre approach," *Composite Structures*, vol. 118, pp. 580-588, 2014, doi: 10.1016/j.compstruct.2014.07.046.
- [54] J. Zhi, L. Zhao, J. Zhang, and Z. Liu, "A Numerical Method for Simulating the Microscopic Damage Evolution in Composites Under Uniaxial Transverse Tension," *Appl. Compos. Mater.*, vol. 23, no. 3, pp. 255-269, 2015, doi: 10.1007/s10443-015-9459-y.
- [55] S. Daggumati, A. Sharma, and Y. S. Pydi, "Micromechanical FE Analysis of SiCf/SiC Composite with BN Interface," *Silicon*, vol. 12, no. 2, pp. 245-261, 2019, doi: 10.1007/s12633-019-00119-3.
- [56] S. M. Mirkhalaf, E. H. Eggels, T. J. H. van Beurden, F. Larsson, and M. Fagerström, "A finite element based orientation averaging method for predicting elastic properties of short fiber reinforced composites," *Composites Part B: Engineering*, vol. 202, 2020, doi: 10.1016/j.compositesb.2020.108388.
- [57] S. E. Naleway, M. M. Porter, J. McKittrick, and M. A. Meyers, "Structural Design Elements in Biological Materials: Application to Bioinspiration," *Adv Mater*, vol. 27, no. 37, pp. 5455-76, Oct 7 2015, doi: 10.1002/adma.201502403.
- [58] B. Zhang, Q. Han, J. Zhang, Z. Han, S. Niu, and L. Ren, "Advanced bio-inspired structural materials: Local properties determine overall performance," *Materials Today*, vol. 41, pp. 177-199, 2020, doi: 10.1016/j.mattod.2020.04.009.
- [59] A. Ghimire, Y.-Y. Tsai, P.-Y. Chen, and S.-W. Chang, "Tunable interface hardening: Designing tough bio-inspired composites through 3D printing, testing, and computational validation," *Composites Part B: Engineering*, vol. 215, p. 108754, 2021/06/15/ 2021, doi: <https://doi.org/10.1016/j.compositesb.2021.108754>.
- [60] Y. Chiang, C.-C. Tung, X.-D. Lin, P.-Y. Chen, C.-S. Chen, and S.-W. Chang, "Geometrically toughening mechanism of cellular composites inspired by Fibonacci lattice in Liquidambar formosana," *Composite Structures*, vol. 262, 2021, doi: 10.1016/j.compstruct.2020.113349.
- [61] Y. Y. Tsai, Y. Chiang, J. L. Buford, M. L. Tsai, H. C. Chen, and S. W. Chang, "Mechanical and Crack Propagating Behavior of Sierpinski Carpet Composites," *ACS Biomater Sci Eng*, Apr 11 2021, doi: 10.1021/acsbiomaterials.0c01595.
- [62] F. Libonati, G. X. Gu, Z. Qin, L. Vergani, and M. J. Buehler, "Bone-Inspired Materials by Design: Toughness Amplification Observed Using 3D Printing and Testing " *Advanced Engineering Materials*, vol. 18, no. 8, pp. 1354-1363, 2016,

- doi: 10.1002/adem.201600143.
- [63] F. Libonati, V. Cipriano, L. Vergani, and M. J. Buehler, "Computational Framework to Predict Failure and Performance of Bone-Inspired Materials," *ACS Biomater Sci Eng*, vol. 3, no. 12, pp. 3236-3243, Dec 11 2017, doi: 10.1021/acsbiomaterials.7b00606.
- [64] L. Long, Z. Wang, and K. Chen, "Analysis of the hollow structure with functionally gradient materials of moso bamboo," *Journal of Wood Science*, vol. 61, no. 6, pp. 569-577, 2015, doi: 10.1007/s10086-015-1504-9.
- [65] G. X. Gu, C.-T. Chen, D. J. Richmond, and M. J. Buehler, "Bioinspired hierarchical composite design using machine learning: simulation, additive manufacturing, and experiment," *Materials Horizons*, vol. 5, no. 5, pp. 939-945, 2018, doi: 10.1039/c8mh00653a.
- [66] G. X. Gu, C.-T. Chen, and M. J. Buehler, "De novo composite design based on machine learning algorithm," *Extreme Mechanics Letters*, vol. 18, pp. 19-28, 2018/01/01/ 2018, doi: <https://doi.org/10.1016/j.eml.2017.10.001>.
- [67] C. Yang, Y. Kim, S. Ryu, and G. X. Gu, "Prediction of composite microstructure stress-strain curves using convolutional neural networks," *Materials & Design*, vol. 189, 2020, doi: 10.1016/j.matdes.2020.108509.
- [68] K. Weiss, T. M. Khoshgoftaar, and D. Wang, "A survey of transfer learning," *Journal of Big Data*, vol. 3, no. 1, 2016, doi: 10.1186/s40537-016-0043-6.
- [69] Z. Q. Fuzhen Zhuang, Keyu Duan, Dongbo Xi, Yongchun Zhu, Hengshu Zhu, Senior Member, IEEE, and F. Hui Xiong, IEEE, and Qing He, "A Comprehensive Survey on Transfer Learning," 2020.
- [70] E. D. Cubuk, A. D. Sendek, and E. J. Reed, "Screening billions of candidates for solid lithium-ion conductors: A transfer learning approach for small data," *J Chem Phys*, vol. 150, no. 21, p. 214701, Jun 7 2019, doi: 10.1063/1.5093220.
- [71] J. Y. Jung, Y. Kim, J. Park, and S. Ryu, "Transfer learning for enhancing the homogenization-theory-based prediction of elasto-plastic response of particle/short fiber-reinforced composites," (in English), *Composite Structures*, Article vol. 285, p. 11, Apr 2022, doi: 10.1016/j.compstruct.2022.115210.
- [72] O. Iatrellis, I. K. Savvas, P. Fitsilis, and V. C. Gerogiannis, "A two-phase machine learning approach for predicting student outcomes," *Education and Information Technologies*, vol. 26, no. 1, pp. 69-88, 2020, doi: 10.1007/s10639-020-10260-x.
- [73] N. Zobeiry, J. Reiner, and R. Vaziri, "Theory-guided machine learning for damage

- characterization of composites," *Composite Structures*, vol. 246, 2020, doi: 10.1016/j.compstruct.2020.112407.
- [74] "ABAQUS Documentation," 2020. [Online]. Available: [https://help.3ds.com/2020/English/DSSIMULIA\\_Established/SIMULIA\\_Established\\_FrontmatterMap/HelpViewerDS.aspx?version=2020&prod=DSSIMULIA\\_Established&lang=English&path=SIMULIA\\_Established\\_FrontmatterMap%2f](https://help.3ds.com/2020/English/DSSIMULIA_Established/SIMULIA_Established_FrontmatterMap/HelpViewerDS.aspx?version=2020&prod=DSSIMULIA_Established&lang=English&path=SIMULIA_Established_FrontmatterMap%2fsim-r-DSDocAbaqus.htm&ContextScope=all)  
[sim-r-DSDocAbaqus.htm&ContextScope=all](https://help.3ds.com/2020/English/DSSIMULIA_Established/SIMULIA_Established_FrontmatterMap/HelpViewerDS.aspx?version=2020&prod=DSSIMULIA_Established&lang=English&path=SIMULIA_Established_FrontmatterMap%2fsim-r-DSDocAbaqus.htm&ContextScope=all).
- [75] L. Bouaoune, Y. Brunet, A. El Moumen, T. Kanit, and H. Mazouz, "Random versus periodic microstructures for elasticity of fibers reinforced composites," *Composites Part B: Engineering*, vol. 103, pp. 68-73, 2016, doi: 10.1016/j.compositesb.2016.08.026.
- [76] W. Tian, L. Qi, X. Chao, J. Liang, and M. Fu, "Periodic boundary condition and its numerical implementation algorithm for the evaluation of effective mechanical properties of the composites with complicated micro-structures," *Composites Part B: Engineering*, vol. 162, pp. 1-10, 2019, doi: 10.1016/j.compositesb.2018.10.053.
- [77] S. Plimpton, P. Crozier, and A. Thompson, "LAMMPS-large-scale atomic/molecular massively parallel simulator," *Sandia National Laboratories*, vol. 18, p. 43, 2007.
- [78] I. T. Jolliffe and J. Cadima, "Principal component analysis: a review and recent developments," *Philos Trans A Math Phys Eng Sci*, vol. 374, no. 2065, p. 20150202, Apr 13 2016, doi: 10.1098/rsta.2015.0202.
- [79] P. Domingos, "A few useful things to know about machine learning," *Communications of the ACM*, vol. 55, no. 10, pp. 78-87, 2012, doi: 10.1145/2347736.2347755.
- [80] F. CHOLLET, "Deep Learning with Python," 2018.
- [81] S. C. Douglas and J. Yu, "Why RELU Units Sometimes Die: Analysis of Single-Unit Error Backpropagation in Neural Networks," in *2018 52nd Asilomar Conference on Signals, Systems, and Computers*, 28-31 Oct. 2018 2018, pp. 864-868, doi: 10.1109/ACSSC.2018.8645556. [Online]. Available: <https://ieeexplore.ieee.org/document/8645556/>
- [82] D.-A. Clevert, T. Unterthiner, and S. Hochreiter, "Fast and accurate deep network learning by exponential linear units (elus)," *arXiv preprint arXiv:1511.07289*, 2015.
- [83] D. Hendrycks and K. Gimpel, "Gaussian error linear units (gelus)," *arXiv preprint*

*arXiv:1606.08415*, 2016.

- [84] S. Ioffe and C. Szegedy, "Batch normalization: Accelerating deep network training by reducing internal covariate shift," in *International conference on machine learning*, 2015: PMLR, pp. 448-456.
- [85] D. P. Kingma and J. Ba, "Adam: A method for stochastic optimization," *arXiv preprint arXiv:1412.6980*, 2014.

